2016

Development of a multi-detector quality assurance instrument for intensity modulated radiotherapy

Claudiu Sebastian Porumb
University of Wollongong

DEVELOPMENT OF A MULTI-DETECTOR QUALITY ASSURANCE INSTRUMENT FOR INTENSITY MODULATED RADIOTHERAPY

A Thesis Submitted in Fulfilment of the

Requirements for the Award of the Degree of

Doctor of Philosophy

from

UNIVERSITY OF WOLLONGONG

by

Claudiu Sebastian Porumb

BMed.Rad.Phys.Adv.

Centre for Medical Radiation Physics

Faculty of Engineering & Information Sciences

2016

Abstract

The advancement of delivery techniques in external beam radiotherapy and ever-increasing complexity of delivery modalities requires that quality assurance systems keep pace with smaller radiation fields, larger dose gradients and dynamic dose profiles. This work describes the development of a novel pre-treatment and *in-vivo* quality assurance devices for use in external beam radiotherapy, including small-beam stereotactic radiotherapy.

The first part of this work aims to describe the architecture of the instrument, the readout electronics, the development of the data acquisition software, and the application of the system as a dual-verification device for intensity modulated radiotherapy using the silicon epitaxial diode array MagicPlate-121. To eliminate the angular dependence of the detector due to the planar structure of the pixels, a cylindrical phantom accepts the insertion of the detector and tracks the motion of the linear accelerator in order to maintain the plane of the detector orthogonal to the incident radiation beam, providing the dose mapping continuously for each gantry angle. The system demonstrated accurate tracking of the linac gantry within ±1.5°. The performance of the device was verified against the expected dose prescribed by the treatment planning software, and it demonstrated an agree-

ment of better than 2% for field size of 5 $\times$ 5 cm^2.

The second part of the study focuses on the characterisation of three monolithic silicon detector arrays developed by the Centre for Medical Radiation Physics. The detectors, named MagicPlate-512 (MP512), DUO and OCTA, are pixellated silicon detectors with 512 pixels fabricated on a *p-type* substrate, arranged in different configurations, and total detector areas ranging from 40.2 $\times$ 40.2 mm^2 to 52 $\times$ 52 mm^2. The MagicPlate-512 detector pixels are 0.5 $\times$ 0.5 mm^2 squares arranged in a square array with an inter-pixel separation (pitch) of 2 mm, while DUO and OCTA are strip detectors with pixel areas of 20 $\times$ 800 µm^2 and 40 $\times$ 800 µm^2, respectively, pitch of 200 µm and 300 µm, respectively, arranged in orthogonal linear arrays, with a special square central pixel arrangement dedicated to accurate determination of output factors for small beamlets. For a low p-stop concentration sample, the MP512 detector demonstrated an unusual uniformity in the form of a circular artifact of around 17 mm radius around the center of the array due to thermal donor impurities present in the substrate. This was mitigated by using a higher concentration of p-stop implantation. The DUO and OCTA low resistivity silicon detectors operating in passive mode demonstrated high charge collection efficiencies of 66% and 73% respectively when irradiated by alpha particles with energy 5.5 MeV and compared to a fully depleted Hamamatsu PIN diode. Despite the small pitch, the DUO and OCTA detectors showed negligible inter-pixel crosstalk.

The third part of this work focuses on the application of the MP512-based quality assurance instrument to characterise a cobalt-60 low dose rate irradiator, for three beam sizes of diameters 20 mm or less. The high spatial resolution of the instru-

ment resulted in beam profile agreement with radiochromic film within $<$1 mm. The speed of the irradiator shutter was determined to be 20 cm/s and 26 cm/s for exposing and concealing the beam, respectively.

The fourth part of the study, the MP512 quality assurance device was used in stereotactic motion adaptive radiotherapy to investigate the impact of motion correction for a simulated lung treatment. The MP512 agreed with radiocromic film within 4% and less than 0.5 mm for profile full-width at half-maximum and penumbra measurements.

Acknowledgements

I would like to sincerely thank my supervisors Dr. Marco Petasecca and Dist. Prof. Anatoly Rozenfeld for their guidance, patience and support throughout my PhD journey, and my whole university journey. Their knowledge and invested time have helped shape my scientific aptitudes, my team skills and networking capabilities. The opportunities to travel and attend international conferences with the Centre for Medical Radiation Physics have been an absolute privilege, and have provided me with an invaluable opportunity to meet other researchers from around the world.

I would like to acknowledge Dr. Martin Carolan for his many evenings spent with us at Illawarra Cancer Care Centre, so that we may perform our measurements on the linacs and achieve the goals of our experiments.

Many thanks also to Prof. Peter Metcalfe for the coffees and multitude of trips to Liverpool hospital during weekends. And the occasional chat outside his office. It is always a pleasure to discuss any topic, ranging from physics to surfing.

Thank you to Assoc. Prof. Michael Lerch for always being helpful and positive regarding everything. His leadership and positive attitude especially in the physics

labs is inspiring.

Thank you to Dr. Justin Davies for his support during the irradiation by Co-60 at the GATRI facility, and to Dr. Dale Prokopovich for the assistance during the measurements at the IBICC facility, both at ANSTO.

Thank you to Dr. Dean Cutajar for his help and guidance with IBICC and the charge collection efficiency studies. Thank you also for providing access to the CMRP cluster.

Thank you to Julian Steele for providing me with the optical bench equipment from his department so that I may perform the mapping of our detectors.

I'd also like to acknowledge Amy Walker and Elise Pogson for their help with the Pinnacle treatment plans. With their help I was able to generate the phantom dose maps required for my project.

Thank you to Dr. Susanna Guatelli and Dr. Iwan Cornelius for their help with Geant4 programming. While my project did not get to include such a section, their effort is nonetheless appreciated.

Many thanks to Dr. Linh Tran and Lachlan Chartier for their help and explanations regarding IBICC. Their MATLAB code has helped me generate the charge collection efficiency and charge sharing graphs in this thesis.

Thanks also to all my family and friends for their encouragement while undertaking this project. Thanks Chris Cassell for being a great friend and for our project-related chats in amongst all the coffee.

Many thanks to my girlfriend Lauren for the love and support throughout this

project. Our scientific conversations and sharing of ideas has often returned fruitful results.

A big thank you to both my parents Ioan and Teodora for supporting me and encouraging me throughout the whole PhD and my university studies. Their patience, wisdom, love, support, ideas and words of encouragement are priceless. Thank you for everything.

Contents

List of Figures

List of Tables

List of Abbreviations

ACQ	Acquisition class
ANSTO	Australian Nuclear Science and Technology Organisation
ADC	Analog to digital converter
AFE	Analog front-end
API	Application programming interface
ASIC	Application-specific integrated circuit
CCD	Charge-coupled device
CCE	Charge collection efficiency
CMRP	Centre for Medical Radiation Physics
CPE	Charged particle equilibrium
CRT	Conformal radiotherapy
CT	Computed tomography
DAC	Digital to analog converter
DAQ	Data acquisition
DLL	Dynamic link library
DMG	Dose Magnifying Glass (detector)
DMM	Digital multi-meter

DMLC	Dynamic multi-leaf collimator
DVH	Dose volume histogram
EBRT	External beam radiotherapy
EMR	Electromagnetic radiation
EPID	Electronic portable imaging device
FFF	Flattening filter free
FIFO	First-in first-out
FPGA	Field-programmable gate array
GB	Gigabyte
GRC	Generation and recombination centers
GUI	Graphical user interface
IBICC	Ion beam induced charge collection
IC	Ionisation chamber / integrated circuit
I/O	Input-output
IDE	Integrated development environment
IEL	Ionising energy loss
IMAT	Intensity modulated arc therapy
IMRT	Intensity modulated radiotherapy
IR	Infra-red
kB	Kilobyte
LINAC	Linear accelerator
MB	Megabyte
MRI	Magnetic resonance imaging
MLC	Multi-leaf collimator

MP121	MagicPlate-121 (detector)
MP512	MagicPlate-512 (detector)
MPDS	MagicPlate Dosimetry System
MRT	Microbeam radiation therapy
NIEL	Non-ionising energy loss
NMR	Nuclear magnetic resonance
OF	Output factor
OSL	Optically stimulated luminescence
OS	Operating system
PC	Personal computer
PCB	Printed circuit board
PDD	Percentage depth dose
PMMA	Polymethylmethacrylate
PMT	Photomultiplier tube
POI	Point of interest
QA	Quality assurance
RAM	Random access memory
RF	Radio-frequency
RL	Radio-luminescence
ROI	Region of interest
RT	Radiotherapy
SAD	Source to axis distance
SBRT	Stereotactic body radiotherapy
SD	Standard deviation

SiPM	Silicon photomultipliers
SMU	Semiconductor measurement unit
SNR	Signal-to-noise ratio
SRS	Stereotactic radiosurgery
SRT	Stereotactic radiotherapy
SSD	Source to surface distance
TFT	Thin film transistor
UOW	University of Wollongong
VMAT	Volumetric modulated arc therapy

Statement of Originality

This is to certify that the work described in this thesis is entirely my own, except where due reference is made in the text.

No work in this thesis has been submitted for a degree to any other university or institution.

Signed

Claudiu Sebastian Porumb

17 August 2016

Publications

1. C. S. Porumb, A.H. Aldosari, I. Fuduli, D. Cutajar, M. Newall, P. Metcalfe, M. Carolan, M.L.F. Lerch, V.L. Perevertaylo, A.B. Rosenfeld, M. Petasecca, "Characterisation of silicon diode arrays for dosimetry in external beam radiation therapy", *IEEE TNS*, 2016
   doi:10.1109/TNS.2016.2567446

2. C. S. Porumb, J. B. Davies, V. Perevertaylo, A. B. Rosenfeld, M. Petasecca, "Characterisation of a cobalt-60 small-beam animal irradiator using a real-time silicon pixelated detector", *JINST*, 2016
   doi:10.1088/1748-0221/11/04/P04014

3. Z.A. Alrowaili, M.L.F Lerch, M. Carolan, I. Fuduli, C. Porumb, M. Petasecca, P. Metcalfe, A.B. Rosenfeld, "2D mapping of the MV photon fluence and 3D dose reconstruction in real time for quality assurance during radiotherapy treatment", *JINST*, 2015
   doi:10.1088/1748-0221/10/09/P09019

4. M. Petasecca, S. Alhujaili, A.H. Aldosari, I. Fuduli, M. Newall, C.S. Porumb, M. Carolan, K. Nitschke, M.L.F. Lerch, J. Kalliopuska, V. Perevertaylo,

A.B. Rosenfeld, ”Angular independent silicon detector for dosimetry in external beam radiotherapy”, *Med. Phys.*, 2015
doi:10.1118/1.4926778

5. M. Petasecca, M.K. Newall, J.T. Booth, M. Duncan, A.H. Aldosari, I. Fuduli, A.A. Espinoza, C.S. Porumb, S. Guatelli, P. Metcalfe, E. Colvill, D. Cammarano, M. Carolan, B. Oborn, M.L.F. Lerch, V. Perevertaylo, P.J. Keall, A.B. Rosenfeld, ”MagicPlate-512: a 2D silicon detector array for quality assurance of stereotactic motion adaptive radiotherapy”, *Med. Phys.*, 2015
doi:10.1118/1.4921126

6. I. Fuduli, M.K. Newall, A.A. Espinoza, C.S. Porumb, M. Carolan, M.L.F. Lerch, P. Metcalfe, A.B. Rosenfeld, M. Petasecca, ”Multichannel data acquisition system comparison for quality assurance in external beam radiation therapy”, *Rad. Meas.*, 2014
doi:10.1016/j.radmeas.2014.05.016

7. I. Fuduli, C. Porumb, A.A. Espinoza, A.H. Aldosari, M Carolan, M.L.F Lerch, P. Metcalfe, A.B. Rosenfeld, M Petasecca, ”A comparative analysis of multichannel data acquisition systems for quality assurance in external beam radiation therapy”, *JINST*, 2014
doi:10.1088/1748-0221/9/06/T06003

8. A.H. Aldosari, M. Petasecca, A. Espinoza, M. Newall, I. Fuduli, C. Porumb, S. Alshaikh, Z.A. Alrowaili, M. Weaver, P. Metcalfe, M. Carolan, M.L.F. Lerch, V. Perevertaylo, A.B. Rosenfeld, ”A two dimensional silicon detectors array for quality assurance in stereotactic radiotherapy: MagicPlate-

512", *Med. Phys.*, 2014
doi:10.1118/1.4892384

9. A.H. Aldosari, A. Espinoza, D. Robinson, I. Fuduli, C. Porumb, S. Alshaikh, M. Carolan, M.L.F. Lerch, V. Perevertaylo, A.B. Rosenfeld, M. Petasecca, "Characterization of an innovative p-type epitaxial diode for dosimetry in modern external beam radiotherapy", *IEEE TNS*, 2013
doi:10.1109/TNS.2013.2289909

10. A. Espinoza, B. Beeksma, M. Petasecca, I. Fuduli, C. Porumb, D. Cutajar, S. Corde, M. Jackson, M.L.F. Lerch, A.B. Rosenfeld, "The feasibility study and characterization of a two-dimensional diode array in 'magic phantom' for high dose rate brachytherapy quality assurance", *Med. Phys.*, 2013
doi:10.1118/1.4822736

11. P. Metcalfe, A. Quinn, K. Loo, M. Lerch, M. Petasecca, J. Wong, N. Hardcastle, M. Carolan, J. McNamara, D. Cutajar, I. Fuduli, A. Espinoza, C. Porumb, A. Rosenfeld, "Review of four novel dosimeters developed for use in radiotherapy", *Journal of Physics: Conference Series*, 2013
doi:10.1088/1742-6596/444/1/012008

12. M. Petasecca, A. Cullen, I. Fuduli, A. Espinoza, C. Porumb, C. Stanton, A.H. Aldosari, E. Bräuer-Krisch, H. Requardt, A. Bravin, V. Perevertaylo, A.B. Rosenfeld, M.L.F Lerch, "X-tream: a novel dosimetry system for synchrotron microbeam radiation therapy", *JINST*, 2012
doi:10.1088/1748-0221/7/07/P07022

Conferences

1. C.S. Porumb, I. Fuduli, M. Petasecca, Z.A. Alrowaili, A. Espinoza, A.H. Aldosari, A. Cullen, V. Perevertaylo, M. Carolan, M.L.F. Lerch, A.B. Rosenfeld, *A Novel Dual-Verification Quality Assurance System for External Beam Radiotherapy*, 2013 IEEE Nuclear Science Symposium & Medical Imaging Conference, Seoul, South Korea, 27 October – 2 November 2013

2. C.S. Porumb, I. Fuduli, M. Petasecca, Z.A. Alrowaili, A. Espinoza, A.H. Aldosari, A. Cullen, V. Perevertaylo, M. Carolan, M.L.F. Lerch, A.B. Rosenfeld, *A Novel Dual-Verification Quality Assurance System for External Beam Radiotherapy*, 2014 Micro-Mini & Nano-Dosimetry and Prostate Cancer Treatment Conference Workshop, Port Douglas, Australia, 20-25 October 2014

Chapter 1

Introduction

The World Health Organisation predicts that the number of cases of cancer will increase by 70% in the next two decades, and cancer will be the cause of about 14 million deaths per year in 2030. Over 100 types of cancer have been discovered, affecting any part of the body (WHO, 2016). If diagnosed early, some cancers can be either completely cured or the quality of the patients life and chance of survival can be significantly increased. The most common cancer treatments include chemotherapy, surgery and external beam radiotherapy (EBRT). More than half of all cancer patients are prescribed radiotherapy as a form of treatment (WHO, 2016; Maj et al., 2012).

Radiotherapy treatment modalities are advancing in complexity and in ability to spare healthy tissue around the tumor. Volumetric modulated arc therapy (VMAT) minimises the total duration of treatment compared to step-and-shoot modalities by maintaining beam-on during gantry rotation around the patient. Stereotactic radiotherapy (SRT) utilises small beams and high doses to achieve a high confor-

mation to the tumor volume but requires sub-millimeter accuracy to avoid critical organs. The nature of SRT beamlets leads to a loss of lateral electronic equilibrium, which prevents the use of standard dosimetric methods to assess the quality of treatment delivery, otherwise known as quality assurance.

Quality assurance (QA) is defined in ISO 9000:1994 as ”all those planned and systematic actions necessary to provide adequate confidence that a product or service will satisfy the given requirements for quality” (Podgorsak, 2005). In radiotherapy, QA is achieved using point dosimeters such as ionisation chambers, as well as two-dimensional (2D) and three-dimensional (3D) dosimeters, such as radiochromic film, detector arrays and radiosensitive gels. The purpose of QA is to ensure that the dose delivered by the ionising radiation source, usually a clinical linear accelerator, corresponds within the smallest error margins to the specific patient generated treatment plan. As treatment modalities advance, QA for smaller, moving fields must be achieved with accurate instrumentation capable of fast and reliable measurements. This thesis focuses on the development of a quality assurance device with high spatial resolution and high temporal resolution for use in intensity modulated radiotherapy (IMRT), VMAT and SRT.

1.1 Project Aim

This thesis describes the design and implementation of a novel dual-detector quality assurance platform for intensity modulated radiotherapy and volumetric modulated arc therapy. The software development of a multi-threaded data acquisition & control user interface is presented in Chapter 3. Three silicon array detectors

named MagicPlate-512, DUO and OCTA are characterised in Chapter 4 by means of clinical linear accelerator and He^{2+} heavy ion microprobe. Chapter 5 explores the application of the dual-verification instrument, referred to as the MagicPlate Dosimetry System, in a clinical quality assurance study, utilising the cylindrical phantom and the pixellated epitaxial detector array MagicPlate-121, and explores the application of the device for pre-treatment QA as well as real-time *in-vivo* verification.

In Chapter 6, the high temporal resolution data acquisition system connected to the MagicPlate-512 detector is utilised for the characterisation of a low dose rate cobalt-60 irradiator equipped with three small field collimators. The study aims to expand on the results obtained in a previous study and attempts to address the limitations encountered in terms of volume averaging effects due to a comparatively large volume point detector (ionisation chamber).

Chapter 7 explores the use of the MagicPlate-512 system to evaluate the performance of real-time motion adaptive radiotherapy algorithms for multi-leaf collimator tracking based on the Calypso tracking system. Finally, Chapter 8 outlines the main findings of this thesis and explores the advantages, limitations and future developments of the quality assurance device.

Chapter 2

Literature Review

2.1 Introduction

X-ray radiation was discovered in 1895 by Wilhelm Röntgen, who noted its imaging and tissue penetration capabilities. About 1-2 months later, Leopold Freund and Eduard Schiff proposed the use of x-rays for medical treatment of diseases. Their experiments quickly prompted physicians around the world to commence using x-rays patient treatment and publish their findings. While it was still unknown how x-rays worked, they were being used to successfully treat superficial diseases such as lupus, ulcers and epithelioma.

Today, clinicians use x-rays to treat a variety of diseases, both superficial and deep in the body, using advanced delivery techniques that will be described in this chapter. X-rays are defined as energetic electromagnetic radiation (photons) originating from electron de-excitations in atoms or from bremsstrahlung (decelerating

or braking radiation) caused by high-speed electron deceleration when incident on high density material.

Radiotherapy (RT) is used in about 60% of cancer treatment cases (TROG, 2013), alongside non-radiation treatments such as surgical interventions and chemotherapy. Radiotherapy is of three kinds: systemic, which involves ingestion or injection of unsealed sources into the body, internal, known as brachytherapy, and external, generally known as teletherapy or external beam radiotherapy (EBRT).

EBRT is the non-invasive form of available radiotherapy. It has evolved from basic open or square field RT (early 1900s) to using collimators to obtain irregular fields in the attempt to maximise dose conformation to the tumour volume. In 1965, a collimator comprised of metal leaves parallel to the beam which could move individually, was invented by S. Takahashi: the multi-leaf collimator (MLC). In 1971, Sir Godfrey Hounsfield invented computed tomography (CT) which, together with the MLC, revolutionised radiotherapy in terms of imaging of the tumour, treatment planning and dose conformation and thus, modern conformal radiotherapy (CRT) was born. About a decade later, Brahme *et al.* (1982) published a paper which laid the foundation to the delivery technique now known as intensity modulated radiotherapy (IMRT). The technique relies on modulating the radiation beam shape and intensity at a number of angles around the target to conform the dose to the tumor, all the while minimising dose to healty tissue and potential organs at risk in the vicinity. Beam modulation was initially achieved by inserting filters in front of the beam; it was later superceded by dynamic MLCs (Bortfeld, 2006). This chapter will outline briefly the various types of modern EBRT including small-field stereotactic radiotherapy, and will describe commercially available

dosimeters used for quality assurance (QA).

2.2 IMRT/VMAT

Intensity modulated radiotherapy is a delivery technique that makes use of a volumetric image of the patient, MLC, and linac pulsed delivery to conform high doses of radiation to the tumour volume, while maximising sparing of healthy tissue. Typical IMRT plans deliver 70-80 Gy of dose in 15-30 fractions and are comprised of segments of different intensities and MLC shapes, yielding irregular field shapes at different linac gantry angles. The typical area of the fields used ranges from 4×4 cm^2 to 40×40 cm^2. There are two types of IMRT: step-and-shoot, where the MLC shape is kept constant throughout beam-on, and dynamic sliding window, where the beam is kept on while collimator leaves move into the required position. The latter can be affected by mechanical drag of the leaves, in which case the beam has to be stopped until the MLC reaches the required position (Wong, 2011).

Volumetric modulated arc therapy originates from a paper by Yu (1995) that suggested a new technique named intensity modulated arc therapy (IMAT), in which the beam is modulated by the MLC as the linac gantry rotates in an arc around the patient. IMAT was further improved by varying the dose rate and gantry rotation velocity during beam-on phase (Otto, 2008), thus minimizing treatment delivery time and maximizing patient throughput (Matuszak et al., 2010). This is now known as VMAT, Volumetric intensity Modulated Arc radiation Therapy.

2.3 Introduction of Stereotactic Radiotherapy

2.3.1 Stereotactic Radiosurgery

Stereotactic radiosurgery (SRS) is a radiotherapy technique that involves the delivery of high dose of radiation in one single fraction, mostly to brain lesions, head and neck or back spine. It is characterised by large dose drop-off gradients to minimize dose to proximal organs at risk, high geometric accuracy of treatment using three-dimensional coordinate system, and fields that are smaller than those used in 'traditional' treatments fields ranging between 0.3 and 4 cm in diameter (Das et al., 2008). Dose delivered by SRS varies from 8 – 24 Gy (Yamada et al., 2008) in a single fraction. Typical size of tumors treated by SRS is no larger than 4 to 5 cm.

2.3.2 Stereotactic Body Radiotherapy (SBRT)

As with stereotactic radiosurgery, SBRT is a highly conformal RT technique utilising fields smaller than 4×4 cm^2 to treat small tumors in lung, prostate, liver, pancreas or spine. SBRT is used to spare organs-at-risk proximal to the lesions, using large doses typically 10 – 35 Gy (Balagamwala et al., 2012). SBRT is a hypo-fractionated modality, dividing the delivered dose in 2 – 5 fractions. High spatial resolution detectors in the order of 2 mm or less (Aldosari et al., 2014) are required to perform dose verification and quality assurance for SRS and SBRT.

2.4 Small-field Dosimetry Quality Assurance

Small field dosimetry applies to radiation beams whose field size is "smaller than the lateral range of the charged particles that contribute to the dose deposited at a point along the central axis" (Charles et al., 2014). Generally for 6 MV beam, this refers to fields smaller than 3×3 cm^2, however a more conservative field size of 4×4 cm^2 is suggested in the Institute of Physics and Engineers in Medicine (IPEM) Report No. 103 to account for "confidence in measuring data" at field sizes smaller than 4 cm at various clinics (Charles et al., 2014). The dosimetry of such small fields becomes problematic due to the lateral electronic disequilibrium (Das et al., 2008) and high doses of radiation delivered in hypo-fractionated plans. The potential consequences when delivering such high doses with an error in the position or the dosage can be damage to healthy tissue surrounding the tumour, and underdosage of target volume, which can reduce tumor control. When using detector arrays to perform QA, small field dosimetry necessitates detectors with spatial resolution of 2 mm or less (Aldosari et al., 2014) to assess the dose drop-off in the penumbra region with confidence. QA is generally performed using film, although this method is time consuming and results are delayed due to development time of the film, and if an ionisation chamber array detector is available as a realtime detector, the spatial resolution of modern commercially available devices is way too low for an accurate reconstruction of small field mapping.

2.5 Radiation Detectors for Radiotherapy and Small-field Dosimetry

In this section, a brief description of detectors which can be used in EBRT are described and their advantages and limitations outlined.

2.5.1 Ionisation Chambers

The ionisation chamber (IC) is the gold-standard detector in radiation therapy, due to the fact that it yields highly reproducible, reliable response. The principle of operation of the IC is the collection of charge from a gas-filled cavity, usually air, under an electric potential of 100 to 500 V. Incident radiation ionises the gas in the chamber and the ions generated – which are proportional to the energy absorbed by the gas – are collected at the anode. Ionisation chambers are usually thimble-type or cylindrical in shape, with the collecting electrode (anode) in the center and the outer wall being the second conductive electrode, however parallel-plate ionisation chambers are also used, mostly for surface dose measurements (Cross, 1992) or as liquid-filled ionisation chambers (Poppe et al., 2013; González-Castaño et al., 2011). Open-air ionisation chambers require further temperature and pressure correction compared to the sealed chambers, to account for changes in the mass of the air present in the chamber (Podgorsak, 2005).

The main limitation of ion chambers is their relatively large volume (up to 1 cm^3) which is subject to volume averaging effects in high dose gradient scenarios. While ionisation chambers with volumes as low as 0.003 cm^3 are commercially

available, the decreasing volume of an ionisation chamber leads to very small and unreliable measured signal. Thus, the necessity for higher detector volumes can result in over-estimation of penumbra, and limitations in small fields where lateral electronic equilibrium is not achieved (Bucciolini et al., 2003; Das et al., 2008). This becomes a problem in small-field radiotherapy, such as SRS and SBRT as the uncertainty in measurements increases with increasing dose gradients and with decreasing field size. Liquid-filled ionisation chambers try to address this issue by replacing the gas in the chamber with tetramethylsilane, cyclohexane or isooctane (González-Castaño et al., 2011), thus maximising the number of radiation-generated ionisations by a factor of up to a few hundred, which allows for a smaller sensitive volume, usually a few cubic mm (Wickman, 1974). Liquid-filled ICs have long-term stability issues and in some circumstances, require a higher applied voltage up to 1000 V (Poppe et al., 2013; Wickman, 1974).

2.5.2 Silicon Diode

The silicon diode is a radiation detector, capable of high signal-to-noise ratio (SNR) and a very small sensitive volume. Silicon based detectors are more sensitive than an ionisation chamber of the same volume (Rikner and Grusell, 1987) due to the higher atomic number (Z) of silicon, which leads to approximately 18000 times more sensitivity per unit volume when compared to air. Silicon diodes can be arranged into arrays to cover larger areas and to be able to sample most or all of the area of a radiation field. Due to the versatility and robustness of silicon, the detector arrays can be arranged in many configurations, leading to the capability of assessing large dose gradient regions with submillimeter accuracy.

The principle of operation of the silicon diode is a *p*-*n* junction. Radiation detection is achieved by generation of electron-hole pairs due to ionising radiation, in the sensitive volume of the detector, which is collected as a current at the electrodes. Silicon, which is a group IV element, is a poor conductor when it is a pure (intrinsic) crystal, because there are no free charge carriers within the silicon lattice for electricity to flow. The conductivity can be modified by implanting group III or group V impurities such as boron and phosphorus, respectively, within the silicon, at a concentration of one impurity atom per 10^{11}-10^{14} silicon atoms, for high to low resistivity substrates, respectively. This process is known as silicon doping. Lightly doped silicon is known as an extrinsic semiconductor, while heavily doped silicon whose conductivity is similar to that of metal is referred to as a degenerate semiconductor; this can be shown by referring to the semiconductor as *p*+ or *n*+. Doping with boron produces *p*-type silicon (acceptor) whereby the boron atom has three valence electrons which form covalent bonds with the silicon atoms in its vicinity. This leaves one hole which is free to move within the lattice; this hole can be referred to as a positive charge relative to its surroundings. Alternatively, doping with phosphorus produces *n*-type silicon (donor) where four valence electrons form covalent bonds while the fifth excess electron is free to move within the crystal lattice. A junction is created when a bulk of a certain type is implanted on the surface with high concentration of the opposite dopant. The 'type' of the junction is defined by the type of the bulk material.

At the region of the junction, the majority carriers (i.e. electrons and holes) diffuse into the opposite type, creating an intrinsic area where there are no free charge carriers (Fig. 2.1). The distribution of positive and negative charges at the opposite

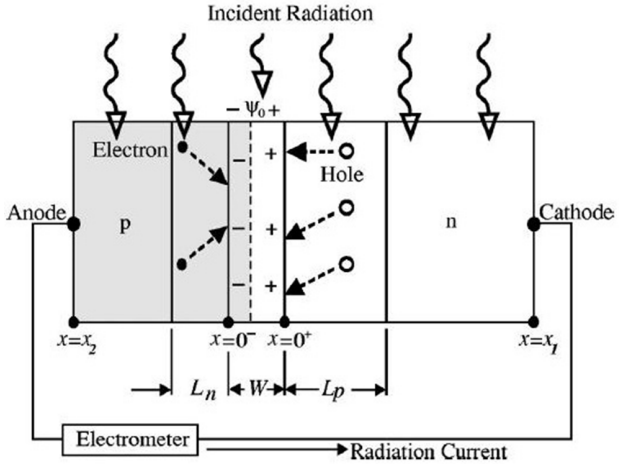

Figure 2.1: Schematic diagram of a *p*-*n* junction used as a detector, and subjected to incident radiation (Shi et al., 2003)

sides of the depleted region results in an electric field due to the immobile impurity atoms, which determines a differential of potential known as the built-in potential, Ψ_0. Equilibrium is reached whereby no more diffusion occurs due to the built-in potential and is proportional to the difference of doping concentration between *n*+ and *p*+ regions. The length of this section, W, is known as the depletion region; its length is also dependent on the impurity concentration. The sensitive volume (or active volume) of the detector is defined as the product of the area of the junction and the minority carrier diffusion length (L_n for electrons and L_p for holes, Fig. 2.1). The minority carrier diffusion length L is defined as:

$$L_p = \sqrt{D_p \tau}; L_n = \sqrt{D_n \tau}, \tag{2.1}$$

where D_n and D_p are the diffusion constants for electrons and holes, respectively, and τ is the minority carrier lifetime. When operated in passive mode, there is no external bias applied on the junction and no current flows due to the balance

of drift and diffusion of carriers. If ionising radiation is incident on the junction, electron-hole pairs are generated in the diode, with the average energy required to ionise the silicon being 3.6 eV. The minority carriers generated within the diffusion lengths L_p for *n*-type and L_n for *p*-type diodes will diffuse towards the junction. This current flow is detectable and can be read externally by the electrometer.

Applying an external bias across the diode affects the resulting signal. Under forward bias, current flows through the diode, increasing exponentially with the voltage, following the Shockley diode function (Shockley and Read, 1952). Under reverse bias, the depletion region increases in width due to the majority carriers in the silicon being attracted to the electrode and thus away from the junction. While this results in a larger sensitive volume at the junction, it is also accompanied by leakage current caused by lattice impurities, which is an undesired effect generating a baseline signal which varies with accumulated radiation damage (Moll et al., 2000) and therefore requires frequent and time-consuming recalibrations of the detector. Therefore for medical applications, silicon detectors are operated with no bias applied (passive mode).

The ability of a diode to detect radiation is dependent on the minority carrier lifetime, which is inversely proportional to concentrations of defects in the silicon lattice and, depending on the substrate type, trapped charge at the Si-SiO_2 interface due to radiation damage, in the case of MOSFET-type detectors. Carrier lifetime is affected by photon beams if the energy of secondary electrons generated in the silicon is at least 260 keV (Li, 2009); this creates generation and recombination centers (GRCs) in the silicon with a cross-section of about 10^{-3} of that of 1 MeV

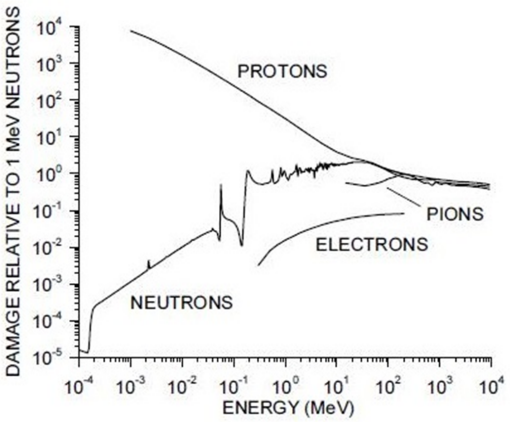

Figure 2.2: Displacement damage in silicon normalized to 1 MeV neutrons for a multitude of charged particles (Moll, 2006)

neutrons. There are two types of radiation damage that can affect the performance of silicon detectors: bulk damage which refers to atomic displacements based on non-ionising energy loss (NIEL) due to high energy-events that can be caused by protons, neutrons, electrons and high-energy photons. A physical displacement of a silicon atom to an interstitial place in the lattice can occur. The second type of radiation damage that affects silicon detectors is surface damage which is based on ionising energy loss (IEL) and is characterised by accumulation of trapped positive charges in the SiO_2-Si interface (Wunstorf et al., 1996).

Bulk damage is produced by inelastic collisions which occur when the incident radiation particle has enough energy to displace a whole silicon atom from its designated place in the lattice, causing a Frenkel defect (or Frenkel pair, referring to the displaced atom and its associated vacancy). Fig. 2.2 shows the charged particle bulk damage in silicon relative to 1 MeV neutrons. The energy required to induce a Frenkel pair in silicon is 25 eV; if the recoil atom's subsequent energy is 70 keV or higher, it can result in a cascade of interactions, producing both point

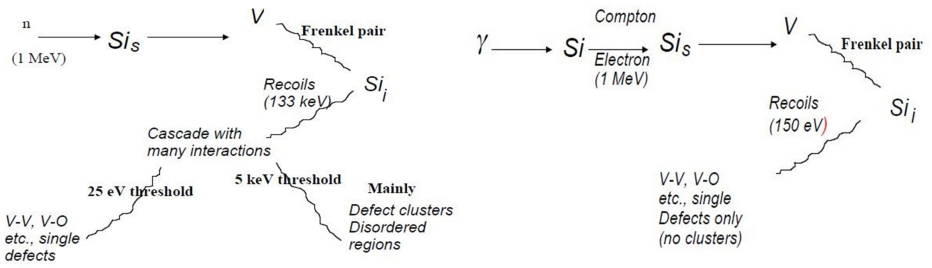

(a) (b)

Figure 2.3: NIEL bulk damage defects diagram (Li, 2009) by (a) 1 MeV neutrons; (b) Co-60 gamma photons

defects and clusters (Li, 2009), as shown in Fig. 2.3. Gamma photons resulting from Co-60 have energies of 1.17 MeV and 1.33 MeV; this is only enough to produce Frenkel pair point (single) defects and the energy of the silicon atom is not enough to produce cluster defects (Fig. 2.3).

The effects of bulk damage on detector properties include an increase in leakage current, substrate type inversion (in *n*-type substrates) and a decrease in charge collection efficiency. Leakage current increases due to formation of GRCs in the mid-band gap (Li, 2009; Borchi and Bruzzi, 1994). One way to mitigate this effect is to use the detector in passive mode (Bruzzi et al., 2007). Substrate type inversion under irradiation refers to *n*-type silicon and the effect of the donor dopants being suppressed by radiation-induced acceptor impurities (Moll, 2006). A solution to mitigate this effect is oxygen doping, which reduces the effect of donor removal (Moll et al., 2000). The creation of GRCs also affects the charge collection efficiency (CCE) of the diode, which depends on the minority τ, volume of detector, and distribution of the electric field. Increased carrier capture results in a lowered CCE, thus a lower sensitivity of the silicon detector over time.

Photoneutron damage may occur in silicon when the diodes are used in radiotherapy photon fields with energies 10 MeV and larger. Photonuclear reactions occur at these energies due to the energy of the incident photon being larger than the (γ, n) threshold energy, which generates photoneutrons in contact with the linac components such as jaws, MLC, target, flattening filter, etc., as well as generating photoneutrons in the patient and in the bunker walls and floor as a result from photon scattering. Typical mean photoneutron energies vary from 1 to 2 MeV (Kim and Lee, 2007). While the generation of photoneutrons in the linac bunker can affect the patient and personnel, it also can affect the radiation detectors by inducing defects in the bulk silicon. It is thus important to characterise the effect of photoneutrons have on silicon radiation detectors to obtain the lifetime of the QA device, as well as the time interval necessary before recalibrating the detector.

Surface damage in silicon occurs from IEL and manifests as an overall build-up of positive charge in the SiO_2-Si interface. Electron-hole pairs are generated in the dielectric material: electrons can escape the dielectric but the holes, having a smaller mobility, are trapped at the interface generating an accumulation of positive charges. Electron-hole pairs generated in the bulk silicon may interact with the accumulation layer at the silicon-dioxide-silicon interface increasing their probability of recombination with the trapped charges, thus reducing the sensitivity of the junction (Borchi and Bruzzi, 1994).

Silicon diodes have a higher Z than tissue, which leads to an over-response compared to tissue-equivalent detectors when the diodes are exposed to incident photons of energy below 200 keV. This is due to a higher ionisation rate per unit volume in silicon compared to tissue or water due to the photoelectric effect which is

proportional to the fourth power of the atomic number of the material. Thus the intensity of the silicon diode response changes as a function of photon energy in this range. Furthermore, the response of the *p-n* junction varies as a function of radiation angle of incidence due to the asymmetry nature of the junction, as all diodes are planar devices (Wong et al., 2012). Therefore in summary, silicon diodes have large sensitivity and linearity, and have very small sensitive volumes compared to ionisation chambers; they can be used in arrays to achieve high spatial resolution detectors with submillimeter pitch, as well as very high temporal resolution. However it is important to be aware of the limitations of silicon detectors when using them in radiotherapy, such as angular dependence, energy dependence at low energies and radiation damage effects in clinical radiation fields, and to characterise the diodes in terms of radiation damage, collection efficiency and angular dependence prior to their use as a medical radiation detector.

2.5.3 Diamond Detectors

Diamond is a radiation hard, tissue equivalent material (for photons) which changes its resistance when irradiated and can be used as dosimeter with photon scattering characteristics which mimic tissue. Diamond detectors usually have small sensitive volumes, which proves advantageous in small-beam fields for SRS or SBRT, they are waterproof and have good sensitivity, however the detectors present a dose rate dependence and a difficulty in attaching the electrodes to the surface of the crystal, as well as high manufacturing cost, low reproducibility (no diamond detector is identical to any other) and low fabrication yield (Heydarian et al., 1996). Diamond detectors necessitate pre-irradiation to mitigate the electric

polarisation effect (Podgorsak, 2005).

2.5.4 Fiber Optic Dosimetry

A scintillating fiber dosimeter is a type of detector comprised of a scintillator, an optical fiber light guide and a photodetector. The chemical composition of the scintillator can be organic, such as plastic polyvinyltoluene (PVT) mixed with a small percentage of organic fluorescent material (Beddar et al., 1992); or inorganic, such as NaI(Tl), CsI(Na), etc. Scintillators undergo prompt radioluminescence (RL), but some can present optical stimulation luminescence (OSL) properties when subjected to green laser light (Aznar et al., 2004). The fiber guide is made of polystyrene with PMMA cladding, to improve light transmission. The photodetector can be a PMT, a CCD camera (Frelin et al., 2006) or solid state photomultipliers such as Silicon PM (SiPM). Plastic scintillators are preferred for use in radiotherapy because they are tissue equivalent and can be used *in-vivo*; they are not affected by temperature or pressure and no dose conversions from one medium to another need to be made to the response (Beddar et al., 1992).

The limitations of the dosimeter include loss of signal over time as a function of radiation damage in the scintillating material, and generation of Čerenkov radiation within the optical fiber, which contributes to the scintillating signal when the kinetic energy of the electrons exceeds 146 keV. This contribution needs to be subtracted from the scintillator signal. For every 7.4 cm of optical fiber exposed to the radiation beam, the Čerenkov contribution from the fiber will be of the same order of magnitude as the optical signal from a 1 mm long Bicron BCF-60 scin-

tillator of 1 mm diameter (Frelin et al., 2006). One way to mitigate this effect is through the use of an air core light guide which minimises the Čerenkov light production but the air gap between the scintillator and the optical fiber reduces the number of photons transmitted to the readout electronics due to a mismatch of the refractive indices (Lambert et al., 2008; Beddar et al., 2004; Law et al., 2007). Effective subtraction of Čerenkov noise by use of an adjacent background fiber limits the use of the detector *in-vivo* due to increased thickness of optical fiber. Furthermore, if the dosimeter readout is based on the classic PMT, the use of the detector is limited to non-magnetic RT modalities, as PMTs are sensitive to magnetic fields. Thus the detector would not be suitable for mixed modalities such as CT-MRI or linac-MRI. If the readout electronics are based on SiPM, the dosimeter becomes very sensitive to temperature variations, which affect the gain.

2.5.5 Thermoluminescent Detectors

Thermoluminescent dosimeters are a type of scintillating phosphors such as LiF crystal doped with Mg and Ti, in which electrons and holes generated by incident radiation can get trapped in the energy band gap between the valence and conduction bands. The traps in the band gap are created by the dopants. The trapped charge can be forced to recombine and release visible light by thermally annealing the material up to 400 °C in an oven. The thermoluminescent light is detected by a PMT. Advantages of TLDs include small and versatile crystal size, no need for wires to connect the TLD to readout electronics, good reproducibility, and tissue equivalence of some crystals (Miljanić et al., 2002; Un et al., 2014). Because TLDs do not require wiring to be read out in real-time, they can be used *in-vivo*,

however this is also the main limitation of the TLD because it is not a real-time detector. TLDs necessitate pre- and post-irradiation thermal annealing, some crystals necessitating as much as 24 hours annealing prior to use (Attix, 2004). The readout of the crystals is sensitive to scratches and fingerprints on the surface of the TLDs, therefore extra care must be taken to handle the crystals. Furthermore, crystals with glow peaks around 100 °C are subject to trap leakage and must be read out as quickly as possible after irradiation.

2.6 2D Detectors and Semiconductor Arrays

2.6.1 Radiochromic Film

Radiochromic film is a self-developing film with high operational dose range from "less than 1 Gy up to many kGy" (Butson et al., 2003), comprised of a radiosensitive active polymeric layer material which changes colour when subjected to irradiation. The radiochromic films active layer interacts with the incident radiation to polymerise and change its chemical formula, with the resultant polymer having a higher optical absorbance than prior to irradiation. This relationship between the optical density and dose can be obtained using a calibration curve (Butson et al., 2003) and the delivered dose corresponding to the films optical density can be determined.

While radiochromic film presents excellent spatial resolution and good performance in high dose gradient beams (Butson et al., 2003), the film is not real-time, as polymerisation takes about 24 hours to fully develop after irradiation

and 48 hours to be completely stable. Furthermore, radiochromic film does not provide absolute dose measurements and can be dependent on scanner-induced non-uniformities. Radiochromic film cannot be re-used after irradiation and is sensitive to sunlight and some luminescent light sources, thus it must be stored in dark envelopes. It must be handled carefully, as scratches or fingerprints on the surface of the film will introduce artifacts in the optical density measured.

2.6.2 IBA I'mRT MatriXX

The I'mRT MatriXX detector is an IMRT dosimetry solution by IBA (Schwarzenbruck, Germany). The detector is a planar array of 1020 vented (open air) ionisation chambers arranged in a 32 $\times$ 32 square of total area 24.4 $\times$ 24.4 cm^2. Pitch of the detector is 7.62 mm. MatriXX has a 3 mm and 22 mm tissue equivalent build-up and backscatter, respectively. The ionisation chambers are cylindrical in shape, with diameter of 4.5 mm, height 5 mm and volume of 0.08 cm^3.

The MatriXX shows good linearity between 9 and 800 cGy, good reproducibility and is energy independent for 6 MV and 10 MV beams (Alashrah et al., 2010). However due to the large volume of the ionisation chambers, the detector suffers from volume averaging effects and overestimation of penumbra width by as much as 30% to 50% compared to reference ionisation chamber (Alashrah et al., 2010, 2013). The shortest possible sampling time using the MatriXX is 20 ms; as such, MatriXX cannot evaluate pulsed linac beams on a per-pulse basis. For warm-up, the detector necessitates a long power-on time of 60 min and large dose of over 1500 cGy (Alashrah et al., 2010).

2.6.3 Sun Nuclear MapCheck

The MapCheck device is a detector by Sun Nuclear (Melbourne, USA) comprised of a planar array of 445 *n*-type diodes arranged in a square. Total area of the detector is 22 $\times$ 22 cm^2, with detector spacing of 7.07 mm in the central 10 $\times$ 10 cm^2 area and 14.14 mm outside the center. The sensitive area of the diodes is 0.8 $\times$ 0.8 mm^2. MapCheck has 2 cm buildup and 2.2 cm backscatter layers which are tissue equivalent.

L'Étourneau et al. (2003) recognises the suitability of the MapCheck to perform routine QA for IMRT. MapCheck is characterised by good linearity and reproducibility with standard deviation of 0.15%. However, the detector is unsuitable for QA in VMAT and SBRT due to non-uniformity limitations arising from the geometry of the detector as a function of beam angle, angular dependence of diodes, and large pitch.

2.7 3D Detectors and Semiconductor Arrays

2.7.1 Gel Detectors

Gel dosimetry is a type of relative dosimetry which utilises gelatin placed in a volume phantom and mixed with a radio-sensitive solution to obtain a true 3D dosimetric image. The gels can be of two types: Fricke gel, named after Fricke dosimetry, which utilises the transition of Fe^{2+} to Fe^{3+} from a ferrous sulphate solution dispersed throughout the gelatin in order to obtain the dose distribution,

and polymer gel, which is similar to radiochromic film. The active component of polymer gels is the acrylamide monomer dispersed through the gel, which polymerises and changes its physical properties, a change that can be detected through a multitude of ways such as x-ray CT, optical CT, NMR and ultrasound. Gels are versatile detectors because they are tissue equivalent, they can be placed in anthropomorphous phantoms, enabling accurate patient QA, and they can be read out by a large variety of imaging modalities (Dosimetry, 2010).

The limitations of gels arise from the diffusion of ions following the irradiation of the Fricke gel, which effectively dissipates the spatial dose information, as well as the potential strengthening of the gel matrix over time and the continuous polymerisation in the polymer gel which could introduce image distortion (Schreiner, 2004; Podgorsak, 2005).

2.7.2 ScandiDos Delta^4

The Delta^4 is an array of silicon diodes within a cylindrical polymethylmethacrylate (PMMA) phantom, by ScandiDos (Uppsala, Sweden). The dosimeter consists of 1069 *p*-type silicon diodes arranged in two orthogonal planes inside the PMMA cylinder of length 40 cm and diameter 22 cm. Diode pitch is 5 mm within the central 6×6 cm^2 area and 10 mm outside the center. Total covered area of diodes is 20×20 cm^2 per plane. The diodes have a sensitive area of 0.78 mm^2. An inclinometer can be placed on the gantry head to provide angular information for VMAT treatments.

Advantages of the Delta^4 dosimeter include good linearity and dose rate response

(Bedford et al., 2009; Feygelman et al., 2011), the ability to produce 3D dose maps, and ability of irradiation from any angle around the cylinder. However it is not suitable for small-field dosimetry due to the large 5 mm pitch of the detector. According to a study by Aldosari et al. (2014), a pitch of 2 mm or less is necessary for dosimetry of small fields, as well as a fast readout mechanism. Furthermore, computationally expensive angular dependence correction needs to be performed post-treatment to account for the angular dependence of the diodes.

2.7.3 Sun Nuclear ArcCheck

The ArcCheck detector by Sun Nuclear (Melbourne, USA) is a 3D dose verification device designed for patient QA in rotational modalities such as helical tomotherapy and VMAT. The device constitutes of 1386 diode detectors arranged in a helical pattern inside an annular cylinder phantom made of PMMA. The phantom has a central cavity of diameter 15.1 cm and an outer diameter of 26.6 cm. The diodes are placed in the center of the annulus, at depth 2.9 cm and 1 cm separation (pitch), resulting in a helical array of diameter and length 21 cm. Each diode has a sensitive area of 0.8×0.8 mm^2 and a volume of 0.019 mm^3. The update frequency of the detectors is 50 ms.

Chapman et al. (2014) concluded that the ArcCheck can be used as a beam quality verification device for tomotherapy, replacing the combination of water tank and MapCheck technique and reducing QA time by more than half. Yue et al. (2014) have also reported very good accuracy of the ArcCheck system for use in tomotherapy. ArcCheck has good agreement with reference ionisation chamber,

and shows good reproducibility. Aristophanous et al. (2016) have reported that the ArcCheck is a suitable detector system for use in IMRT/VMAT, however the gamma passing rates can be affected by a field-size dependence of the system, which can have an impact on the sensitivity of the device. The detector response of the ArcCheck needs to undergo software angular corrections due to the geometry of the detector array, which may be time consuming.

2.7.4 PTW Octavius 4D

The Octavius 4D (PTW, Freiburg, Germany) is a QA device designed for IMRT and VMAT (Urso et al., 2016), comprised of a square array of ionisation chambers placed in a motorised cylindrical phantom which can follow the rotation of the linac head. The phantom has an electron density of 1.016 relative to water, a diameter of 32 cm and length 34.3 cm, and has a square cavity for the insertion of the detector. An inclinometer is placed on the linac head to provide angular information to the motorised phantom. The detector array Octavius 729 has 729 vented ionisation chambers arranged in a square covering an area of 27 $\times$ 27 cm^2 and detector spacing of 1 cm between the centers of the chambers. Each chamber is a parallel plate of 5 $\times$ 5 $\times$ 5 mm^3. Thickness of the array is 2.2 cm and the effective depth of the chambers is 0.5 cm. An SRS version of the Octavius 2D array exists, the 1000SRS, which is comprised of 977 liquid filled ionisation chambers covering 10 $\times$ 10 cm^2 and spatial resolution of 2.5 mm. The dimensions of the liquid IC are 2.3 $\times$ 2.3 $\times$ 0.5 mm^3. Sampling interval of the detectors is 200 ms.

Octavius 4D follows the rotation of the linac head, so as to keep the position of the array always orthogonal to the incident beam. Thus, dose reconstruction is performed using PDD measurements, which have to be carried out to calibrate the device. This way, dose reconstruction can be performed independently of the treatment plan (Allgaier et al., 2013).

McGarry et al. (2013) reported a good linearity, dose rate response and output factor correlation between Octavius, treatment plan and ionisation chamber. The inclinometer accuracy was found to be ±0.5°. When performing clinical deliveries, the gamma pass rate for head and neck plans was over 99% for global 3%/3mm gamma criterion for 6 MV and 10 MV flattening filter free (FFF), with 10% minimum threshold and 90% threshold. Discrepancies were found in high dose gradient regions where 3mm-3% gamma evaluation yielded a pass rate of about 90%. This was attributed to the poor spatial resolution of the 729 detector array, and was not present when the 729 detector was replaced with the 1000SRS. The pass rate when using the latter detector was found to be over 99%.

The limitations of the Octavius 4D include the necessity of warm-up for uniform response of the detector (McGarry et al., 2013), and no dose-per-pulse capability of the system. Furthermore, the large sensitive area of the ionisation chambers can lead to averaging effects in high dose gradient regions, especially when using the 729 detector array.

2.8 Conclusion

In radiotherapy and radiation protection, there is a significant variety of commercially available radiation detectors whose properties are known and have been thoroughly described in the literature. The ionisation chamber is the gold standard detector, due to its reproducibility, stability and energy independence. The most modern QA dosimetry solutions are comprised of detector arrays, which aim to perform dose reconstruction in the body and to maximise spatial resolution in treatment modalities such as IMRT, VMAT, tomotherapy and SBRT, although traditional detectors such as ionisation chambers still have a strong presence in contemporary QA. Current commercially available solutions have limitations such as necessity for detector warm-up prior to irradiation, spatial resolution limitations, temporal resolution limitations, and dose perturbation limitations (can only be used for pre-treatment and not *in-vivo*).

To address these limitations, the solution proposed by Centre for Medical Radiation Physics is a real-time multi-detector semiconductor QA device for use in IMRT, VMAT and SBRT, capable of dose-per-pulse sampling of the radiation beam, and for use in both pre-treatment quality assurance and as an *in-vivo* treatment verification system. The device uses an inclinometer and a moving phantom to follow the linac gantry in order to eliminate angular dependence of the silicon detectors. The detectors used with this prototype are the silicon epitaxial array MagicPlate-121 (Wong et al., 2012; Alashrah et al., 2010), and monolithic arrays MagicPlate-512 (Aldosari et al., 2014; Petasecca et al., 2015; Wong, 2011), DUO (Porumb et al., 2016) and OCTA (Porumb et al., 2016); they vary in detector area, sensitive volume and spatial resolution, and the latter two detectors are capable

of sub-millimeter accuracy. The properties of the MagicPlate-121 as a clinical detector have been thoroughly characterised by , and the MagicPlate-512 partially by.

In the following chapters, the CMRP QA device family MP512, DUO and OCTA will be thoroughly described, the electrical and dosimetric properties of the detectors DUO and OCTA will be investigated and the QA device will be used in conjunction with MagicPlate-121 and MagicPlate-512 detectors to characterise a multitude of treatment solutions and field sizes in a clinical environment, including standard step-and-shoot IMRT, low dose rate cobalt-60 beam profiling, and an adaptive motion radiotherapy case study using simulation of lung motion.

Chapter 3

Unified Platform Design Architecture

Following the development of 1D and 2D silicon array detectors by Centre for Medical Radiation Physics (CMRP) for use in radiotherapy, such as Dose Magnifying Glass (Wong et al., 2010, 2011), MagicPlate-121 (Wong et al., 2012; Alrowaili et al., 2015, 2016), MagicPlate-512 (Aldosari et al., 2014), DUO, OCTA, etc., a new data acquisition system was necessary to be built for 128-channel, 256-channel and 512-channel array detectors to acquire data simultaneously from each detector's pixels. The structure of the DAQ system was chosen to be modular and 'plug-and-play' to make it easy to use a multitude of detectors without the need to modify any hardware connection, or necessitate major electronic setup. The commercially available package LabView which was used previously by Wong et al. (2010, 2011) for DMG and MagicPlate-121 data acquisition has a number of limitations such as the maximum sampling rate, lack of real-time data visuali-

sation, maximum number of connected channels, and cost, which made LabView unsuitable for our requirements for fast real-time 512-channel dosimetry. Therefore CMRP has developed a specialised data acquisition package to address the aforementioned shortcomings.

The CMRP DAQ system is comprised of four main functional blocks: detector, readout electronics, firmware, and software. It features a high temporal resolution (order of microseconds to resolve pulse by pulse linac radiation), high dynamic range (in the order of 10^4-10^5) and a user-determined variable sensitivity to accommodate for detectors with small sensitive volume (and thus small signal), as well as radiation detectors exposed to high flux of x-ray beam (Fuduli et al., 2014). The system must also acquire a large number of channels (variable between 128 and 512) with frame rates up to the order of kHz.

This chapter focuses on the description of the hardware components, including radiation detectors, readout components and cylindrical phantom, and on the software development of the GUI.

3.1 Hardware

3.1.1 MagicPlate-121 Detector

The MagicPlate-121 (MP121) detector is a silicon array detector developed by Centre for Medical Radiation Physics (CMRP), University of Wollongong. The detector is comprised of 121 single silicon epitaxial diodes mounted on a 0.6 mm thick Kapton substrate using CMRP proprietary drop-in technology, arranged in

an 11 × 11 square array with 10 mm diode pitch (separation) and total sensitive area of 10 × 10 cm^2. The diodes were fabricated at the SPA-BIT microelectronics foundry in Ukraine. Each diode is comprised of a 50 µm thick *p*-type silicon epitaxial layer of resistivity 100 Ω-cm, grown on a 375 µm *p*+ silicon substrate of 0.001 Ω-cm. The sensitive area of each diode is 0.6 × 0.6 mm^2 and the total volume of each diode is 1.5 × 1.5 × 0.425 mm^3 (Wong et al., 2011). The MP121 detector and diodes have been characterised by Wong et al. (2012) and Aldosari et al. (2013) and have been found to have excellent reproducibility, linearity, percentage depth dose response, radiation hardness, and a long clinical life. The main shortcoming of the detector is the large diode separation of 10 mm, which despite excellent clinical performance, makes the detector unsuitable for small-beam radiotherapy such as SBRT and SRS.

3.1.2 MagicPlate-512 Detector

The MagicPlate-512 (MP512) detector is a monolithic dosimeter array of 512 submillimeter size ion implanted diodes on a *p*-type silicon substrate, designed by CMRP and manufactured at SPA-BIT foundry, Ukraine. The area of the detector array is 52 × 52 cm^2, with pitch 2 mm between pixels. The pixel element is a planar structure with a central *n*+ junction of 0.5 × 0.5 mm^2 surrounded by a uniform *p*+ implant for polarisation of the substrate and isolation of the pixels (Fig. 3.1). The substrate is 470 µm thick and has a low resistivity.

The back side of the detector has a similar *p*+ implant to realize the ohmic back contact and is polarised at the same potential of the front side diode. The detector

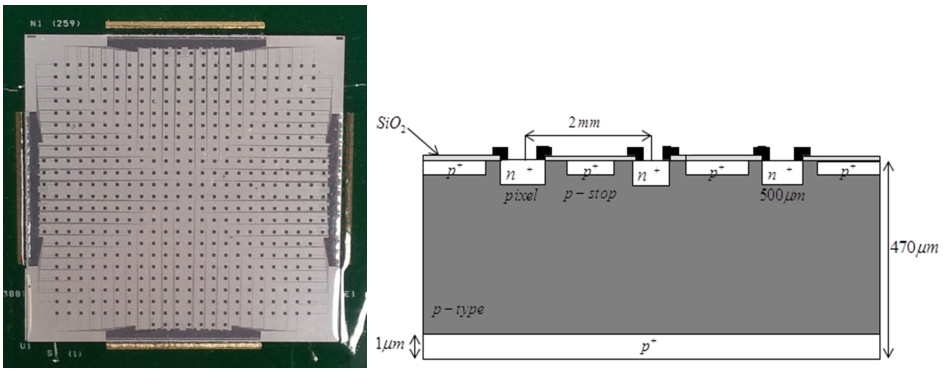

(a) (b)

Figure 3.1: MagicPlate-512 detector (left); schematic diagram of the detector construction (right)

array is covered by a thin layer of protective resin epoxy (approx. 100 μm) to avoid accidental damage of the connections and is wire bonded to a thin printed circuit board (PCB) of dimensions 31 $\times$ 21 cm^2 and thickness 500 μm, which provides the fan-out for connection of the sensor to the readout electronics. The MP512 silicon detector is operating in passive mode, as there is no bias applied to the diodes.

3.1.3 DUO & OCTA Detectors

DUO is a monolithic silicon detector comprised of 512 strips and pixels. The detector is arranged in two orthogonal linear arrays, each with 256 pixels, intersecting at their center, implanted on a 470 μm thick *p*-type silicon substrate. A schematic diagram of DUO's strip-pixel configuration is shown in Fig. 3.2a The array is manufactured on a low resistivity substrate and mounted on an identical circuit board as MP512 (31 $\times$ 21 cm^2 500μm thick PCB). The pixel is an *n*+ microstrip 800 μm long and 20 μm wide, surrounded by a uniform Boron implan-

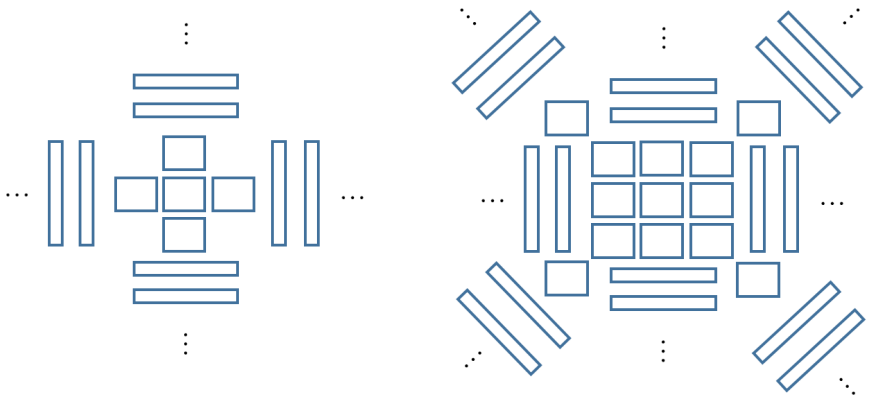

(a) (b)

Figure 3.2: Schematic diagram of (a) DUO and (b) OCTA central structures showing the arrangement of the strips and pixels in the center of the detectors (not to scale)

tation. The microstrip pitch is 200 µm. Five central (non-strip) pixels create the intersection of the orthogonal arrays; they have an area of 0.2 × 0.2 mm^2 each and realise a cross-shaped structure in the very center of the detector with pitch 50 µm. The back side of the detector has the same implant configuration as MP512.

OCTA is likewise a monolithic silicon strip detector with 512 pixels and central non-strip detector structure of 3 × 3 square pixels (Fig. 3.2b). The detector has four linear arrays that form two orthogonal crosses at 45° with respect to one another, intersecting at the center. The total area of the detector is 40.2 × 40.2 mm^2 and the area of the microstrip pixels is 40 × 800 µm^2. The central square pixels are 160 × 200 µm^2 in size and make up a small 3 × 3 square array with pitch 0.3 mm and total area of 920 × 920 µm^2. The pitch in between the microstrip pixels is 0.3 mm.

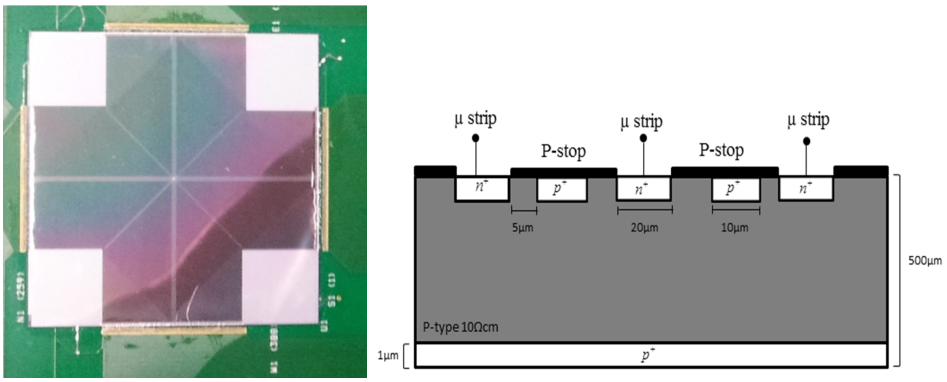

(a) (b)

Figure 3.3: DUO detector (left); schematic diagram of detector, showing pixels and substrate (right)

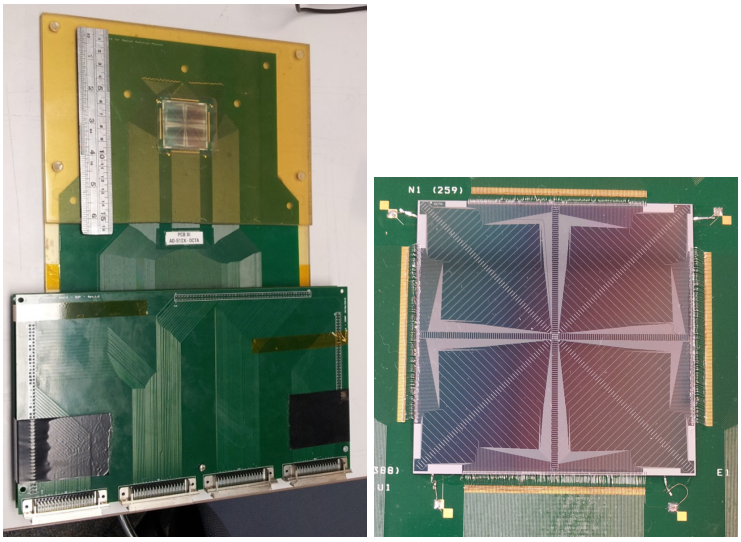

(a) (b)

Figure 3.4: OCTA detector mounted on PCB (left); close-up of detectors sensitive area (right)

3.1.4 Field-Programmable Gate Array

The interface between the DAQ electronics and computer (PC) software is established using an Opal Kelly XEM3001 integration module, based on the Xilinx Spartan 3 FPGA. The FPGA features an on-board electronically erasable programmable read-only memory (EEPROM) for device clock (PLL) configuration, a first-in first-out (FIFO) memory of 32 kilobytes, and offers simple and convenient connection to the PC via a standard USB2.0 communication protocol. A firmware which configures the FPGA and defines the I/O addresses used for communication with the PC has to be loaded into the FPGA every time it is powered on; this is because the firmware is stored in RAM and is not saved on the device when it is powered off. The communication achieved between the FPGA and the computer via USB2.0 will be described in Section 3.2.5.

3.1.5 Inclinometer

The inclinometer used in this project is the 12-bit digital gyroscope ADIS16209 by ANALOG DEVICES (Norwood, MA). The inclinometer is capable of single axis operation ±180° and double axis operation ±90°, has an accuracy of 0.1°, sampling rate of 31.5 kHz and an operating temperature range from -40 to 125 °C. The physical dimensions of the inclinometer are 9.2 mm × 9.2 mm × 3.9 mm. The purpose of the inclinometer is to be fixed to the linac gantry head, to read its angle and provide feedback to the phantom rotation system so that it can update its position accordingly when tracking the linac head.

3.1.6 Rotatable Phantom

The rotatable phantom has been designed and manufactured by CMRP and its purpose is to maintain an orthogonal angle between the linac beam and the plane of the detector array, thus eliminating the need for angular dependence corrections. The phantom is a polymethyl metacralate (PMMA) cylinder of 30 cm diameter, 40 cm length and a total mass of approximately 35 kg. It has a rectangular cavity of 20.5 cm $\times$ 17.5 cm $\times$ 5.1 cm for detector insertion. The detector is sandwiched between 2.5 cm thick SolidWater slabs to maximise water equivalence of the material immediately surrounding the sensitive volumes and replicate electron scattering conditions of water (Aldosari et al., 2014). The maximum range of electrons in water at 6 MV and 18 MV is 2 cm and 2.4 cm respectively (Berger et al., 2015). Thus, the SolidWater inserts ensure that the charged particle equilibrium (CPE) around the detector is not affected by the higher density (1.17 g/cm^3) PMMA bulk of the phantom, which could lead to an over-response compared to water.

The rotatable phantom uses a SICK ATM 60 SSI absolute optical encoder for determining the angle of the cylinder. The encoder has a measuring step size of 0.043° and accuracy of ±0.25°. The digital configuration interface used with the encoder was RS422. The phantom rotates with the use of a NEMA 24 stepper motor with torque 2.74 Nm, powered by a high current power supply and a GECKO stepper motor controller; the GECKO module is controlled by the FPGA through a fully proprietary serial communication protocol. The motor is connected to the cylindrical phantom via a timing belt of length 620-650 mm, which rests on a gear with 18 teeth; to avoid misalignment of the belt, the gear has lateral phalanges.

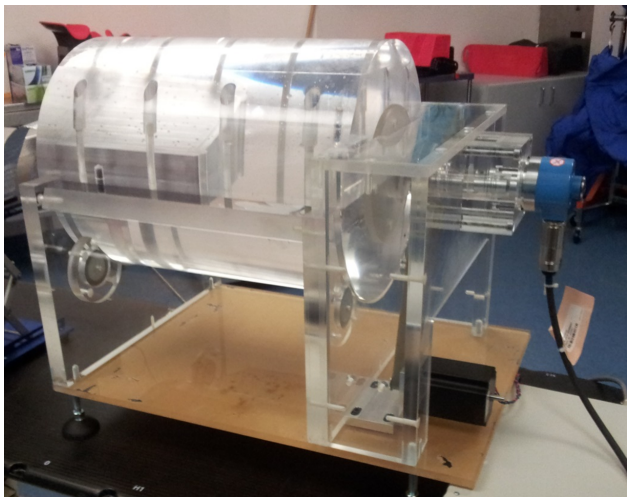

Figure 3.5: The rotatable phantom. The optical encoder can be seen connected to the cable on the right hand side

The gear connected to the motor has 64 teeth. The phantom rotates to match the angle read by the optical encoder to the angle reported by the inclinometer attached to the linac head, with accuracy of ±0.25°.

3.1.7 Readout Systems

The electrical current as a result of electron-hole pairs generated in the silicon from the incident irradiation is collected by a multichannel integrator. The analogue front-end is then interfaced to an analog-to-digital converter which communicates with the FPGA via a serial interface. In this project, two main architectures of analogue front-end have been adopted: the TERA6 from Instituto Nazionale di Fisica Nucleare (INFN) in Turin (Italy) and the AFE0064 from Texas Instruments (CA, USA).

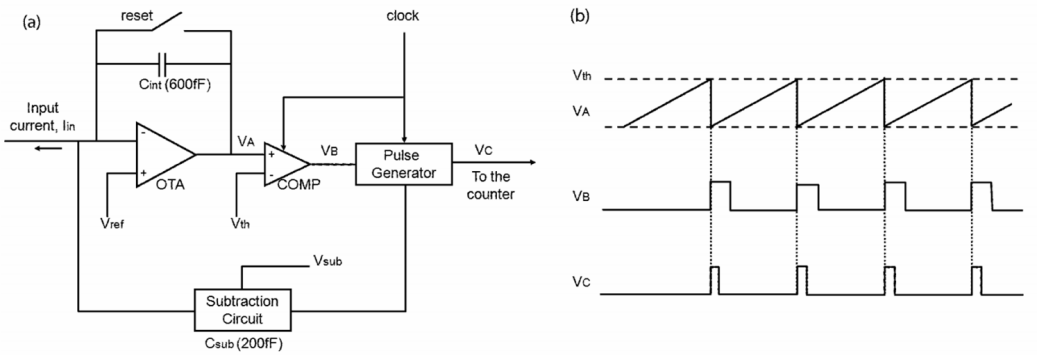

Figure 3.6: Schematic diagram of the TERA recycling integrator

3.1.7.1 TERA ASIC

The TERA application-specific integrated circuit (ASIC) is a 64-channel recycling integrator initially designed by the University of Torino microelectronics group for readout of pixelated ionisation chambers in hadron therapy (Bonazzola et al., 1998). The latest version of the chip, TERA6, is used as the readout system for the ImRT MatriXX detector by IBA. The chip is a 64-channel charge-to-frequency converter. The recycling integrator operates by counting the number of times a capacitor is charged by the input current from the detector and then discharged by the electronics.

The current signal from the detector charges a small capacitor Cint of 600 fF. This causes the output voltage, V_A, of the OTA to increase (Fig. 3.6). V_A is then compared to a reference threshold voltage, V_{th}, by a voltage comparator. When the threshold voltage is reached, the comparator sends a signal (V_B) to the pulse generator. The generator then outputs two pulses: one that is sent to the digital counter to be registered as an event (count), and one pulse is sent to the subtraction circuit. The subtraction capacitor is charged by the pulse from the generator, and

a pulse which is opposite in polarity to the input current is generated; this pulse is then added to the input current to subtract a charge quantum. The charge quantum can be varied in magnitude by varying V_{sub} (this can be adjusted externally using reference voltages) and it determines the unit charge needed for 1 count (Bonazzola et al., 1998). The TERA chip has 16-bit resolution with a maximum number of counts of 65535.

This approach of integrating charge and subtracting a known quantum charge from the integrating capacitor has the advantage of continuously counting as long as V_A is above V_{th}. The alternative would be to completely reset C_{int} which would introduce dead time and possibly lead to signal loss from the detector. The disadvantage of this approach is that if V_A is above the threshold voltage then the system will keep sending pulses to the counter until it is under the threshold; if the dose rate or current from the detector is too large, it may saturate the readout system.

Two TERA chips were used to provide a DAQ system with 128 useable channels for parallel readout. This readout system was used for MagicPlate-121 device.

3.1.7.2 AFE0064 System

The readout system used for 512-channel detectors is based on the AFE0064 multichannel electrometer chip (Texas Instruments, USA) and has been developed by CMRP. The chip, originally designed to read out Thin Film Transistor (TFT) imaging panels of commercially available linac EPID (acronym) detectors, is a 64-channel current integrator with two analog differential outputs, which are pro-

portional to the charge accumulated in a capacitor for each block of 32 integrators. The sensitivity (gain) of the chip can be varied by electronically adjusting the amount of charge stored by the capacitor, from 0.13 pC to 9.6 pC in 7 steps. The AFE has been interfaced to a quad channel Delta-Sigma Analogue to Digital converter (ADC) with resolution of 16-bit for each integrator. The AFE also provides a correlated double sampling of the analogue output in order to subtract the low-frequency noise and baseline from the raw input signal, thus being capable of high signal-to-noise ratio – a highly desired feature in medical instrumentation.

The FPGA (described above) is used to provide the clocks and sync circuits for synchronisation between the AFE and the ADC but also to provide the synchronization with the linac radiation pulses. A coaxial cable is used to receive the linac sync signal, and the FPGA instructs the AFE chip when to sample the detector. A total of 8 chips connected to 4 ADCs are used in this DAQ system to provide 512 channels for parallel readout of the detector. Asynchronous acquisition is possible by use of an internal trigger generator with a maximum frequency of 5 kHz. Instantaneous dose-per-pulse measurements are possible with this architecture.

The AFE-based readout system was used in all experiments involving 512-channel detectors. The readout can also be scaled down to only two AFE chips for a total of 128-channel system for MagicPlate-121; this was performed early during the work to validate the new front-end and verify its performance in comparison with the TERA system.

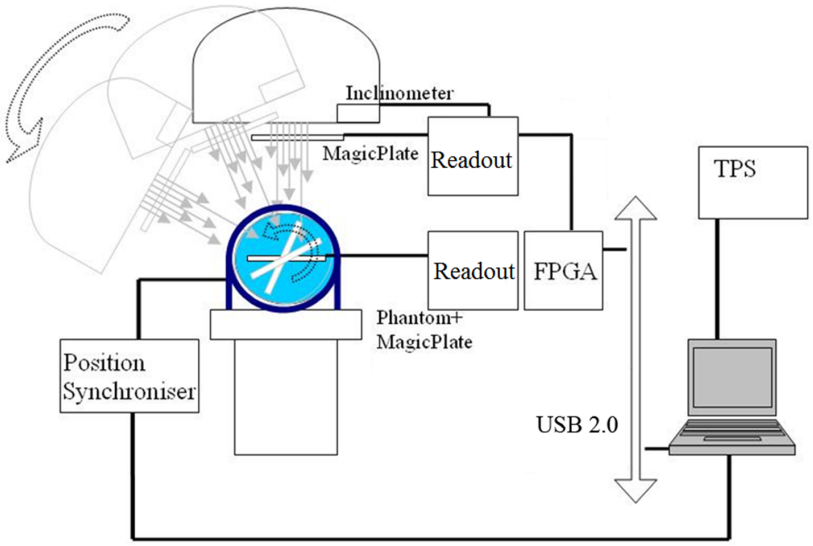

Figure 3.7: Schematic diagram of CMRP dual-verification QA device

3.2 Software

3.2.1 Introduction

The data acquisition software that was developed for this project has three main goals:

- to establish communication with the detector system and acquire data in a lossless manner;
- to save the raw binary to a file, as well as decode it and display it to the user in real-time in a meaningful way; and
- be able to perform analysis on the data by loading it in post-processing mode and displaying the results to the user with additional data handling tools.

In order to achieve these goals, the software had to satisfy a number requirements including robustness, stability, ease of use, and reproducibility, especially under high computational load, because the DAQ software was going to be used for high-bandwidth multi-detector real-time acquisition. Cross-platform capability

was possible within the chosen development environment, but it was not considered a priority, as 100% of data acquisition machines used by CMRP were running Windows.

Through trial and error of preliminary software and a number of versions, the optimum solution was determined to be a graphical user interface (GUI) software application comprised of two threads, each assigned with a standalone task, and each communicating with one another if necessary. The GUI software has been named Romulus Radiation Tools.

The threads that comprise Romulus are the acquisition thread, and the graphical interface thread. These threads are further comprised of specific tasks which will be described below.

3.2.2 The Development Environment

The Romulus software was coded in C++ and utilised the Qt application development network (version 2009.04) for the GUI and multi-threading modules. The compiler used to generate the final executable was 32-bit MinGW (Minimalist GNU for Windows) version 3.81.

3.2.3 The Qt Modules and Basic Structure

Qt integrated development environment (IDE) is a versatile framework for creating cross-platform projects which run regardless of the target machine's operating system (OS). Furthermore, the framework is based on object-oriented program-

ming, with a powerful emphasis on communication between objects and data exchange between classes.

A software project compiled using the Qt framework will always have the Qt backbone when it is instantiated (the *int main()* function), and the user code will be loaded as an object within this core. This has the advantage of making available to the programmer all the functionality of Qt at any time. The programmer then only needs to instruct the compiler to include the header of that module, for example for network functionalities using QtNetwork module, for the drawing functionality using QtOpenGL module, for the database functionality using QtSql module, etc., in order to use it within the code. Thus, the Qt core manages the whole application and most importantly, establishes the communication between the classes and the objects which require it. This is the most powerful advantage of the Qt framework, because it greatly simplifies the way information gets transferred internally between objects. The programmer is not restricted by the direction and flow of code, and multiple objects can access the same data at the same time without the risk of overwriting or bottlenecking.

The two threads in Romulus are Qt "objects" and they communicate with one another by the means of Qt's signal-slot protocol. A Qt-defined object, called a QObject, has the ability to emit a signal, such as a single number, a string, or an array. If it does so, this signal can be detected internally by another object or class, if that class was instructed to listen for the signal, which may perform an instruction once it receives the signal, or it can process the signal itself.

For example, signal-slot connections are made between push-buttons in the GUI and the class responsible for executing code associated with pressing the button.

The push-button, when clicked by the user in the GUI, will emit a signal, named *clicked()*. A function that listens for the *clicked()* signal of the push-button (which was pre-determined in the instantiation, or constructor, of the software), is then responsible to execute the code associated with the user pushing that button on the GUI and will do so as soon as it can, that is, as soon as the CPU is available to execute the code. Under general conditions when a program is idling, this occurs instantaneously. There is no restriction on the number of functions that listen for a signal. QObjects always emit signals when events occur, but it is up to the user to act on those signals or not, and to connect them to the appropriate classes.

3.2.4 Communication between Threads

The GUI code from within the graphical interface thread (thread A) is the code that is responsible for the visualisation of the program, and is the parent thread which calls the acquisition class (ACQ) in thread B to perform a measurement. When the user clicks the "Start" button, the GUI class emits initialisation parameters specific to the particular measurement (such as duration, sampling time, integration width, output file name etc.) which the ACQ class in thread B is configured to receive. At the end of the configuration signals, the GUI emits a *commence()* signal which instructs the ACQ class to start the measurement.

Once started, the ACQ will run as long as per the duration it received in the initialisation unless it is prematurely interrupted by the user. During the measurement, every 100 ms the ACQ will emit a data frame which the GUI will receive, decode and display to the user as real-time feedback from the detector. Once the

measurement is complete, the ACQ will confirm to the GUI the completion of the measurement with a *finished()* signal.

3.2.5 Communication via USB2.0 and the Firmware

The USB (universal serial bus) protocol is a standard for connecting devices to a host, usually a PC. Historically, the justification of the development of USB was to create a universal interface for connecting external devices to a host, regardless of their vendor. Work on USB commenced in 1994 as a joint collaboration between IBM, Compaq, Intel, Microsoft, NEC, DEC, and Nortel; first version USB1.0 was released in 1996; USB2.0 was released in 2000 (R. Murphy, 2016).

The USB interface is comprised of (a) the host controller, which is a hardware chipset (Cypress) that detects attachments and removals of USB devices on the computer, manages data flow, and provides power to devices; and (b) the root hub, which provides the physical connection between the device and the controller (R. Murphy, 2016). Each device is assigned an address by the host (7 bits, for a maximum of 127 connected devices per host), and data flow between the host and device endpoints is achieved through pipes (Fig. 3.8a). There are two types of pipes: control pipe, used for sending commands, querying, and configuring the device; and data pipe, used for data transfer to and from the device. Pipes are discerned by use of different endpoints, with Endpoint 0 reserved as control pipe for each device (Fig. 3.8a). Data is transferred as packets through the pipes. Packets are comprised of:

- 8-bit packet ID (mandatory)
- 7-bit device address (optional)

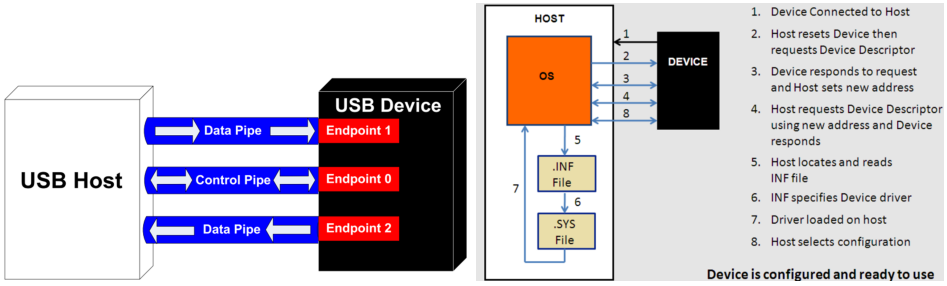

(a) (b)

Figure 3.8: (a) Diagram showing the pipe model communication between USB host and device; (b) Diagram of logical steps taken by the host controller when a new device is connected to PC

- 4-bit endpoint address (optional)
- Payload data up to 1024 bytes (optional)
- Cyclic redundancy check (CRC) for error detection (optional)

The packet IDs identify the type of each packet (eg. token, data, handshake packets etc.) and the controller can discern between packets from different devices travelling via the hub by reading the packets device address.

Each device has a unique driver: a software interface (file with .SYS extension in Windows) which acts as a 'translator' between software running on the PC and the device. The details of the driver (such as name, version, location, registry information etc.) are stored in an accompanying .INF file (R. Murphy, 2016). The process of connecting and configuring a device is shown in Fig. 3.8b.

The FPGA's device driver is supplied by the vendor, Opal Kelly. The communication between the application software (GUI) and the FPGA driver is dependent on the programming language used to code the GUI software. An application programmer's interface (API) which is language-dependent (C#, C++, Python, Java, etc.) is also provided by Opal Kelly in order to allow the developer to communi-

cate with the FPGA using his or her chosen programming language from within the developed software.

In the case of the C++ programming language, the API is a set of libraries and headers for the implementation of establishing communication from within a C++ software application with the device. It is comprised of one dynamic link library (DLL) file, one C++ header file, and C++ code file. These files need to be included in the Qt project. The API creates the handshake between the device driver and Romulus, which allows communication between Romulus and the FPGA. By including the API header, a new object named *okCUsbFrontPanel* can be declared, which will have direct access to the FPGA via the USB2.0 communication protocol. Through the new object, the system can be queried for the number of FPGAs connected, the serial ID of a particular device, and settings and data can be exchanged with the device. The following example code shows how to instruct the system to check for the number of connected FPGA devices:

```
okCUsbFrontPanel *xem = new okCUsbFrontPanel;
xem -> GetDeviceCount();
```

When the electronic readout system is connected via USB and powered on, it follows the process outlined in Fig. 3.8b to be identified and configured by the host PC. In order to control the readout system from the software GUI and for the data to be sent from the readout system to the GUI, the onboard FPGA needs to be configured using a firmware, developed in-house by CMRP. The firmware distinguishes itself from a device driver by the fact that it runs on the device (in this case on the FPGA), and not on the host, and by the fact that the commands used to communicate with the DAQ software are arbitrarily defined by the firmware developer, depending on the requirements and capabilities of the readout system. Thus the

USB standard becomes an underlying carrier for the GUI-FPGA commands and data flow. The firmware is a simple binary file with *.bit* extension and is loaded on the FPGA by calling the *ConfigureFPGA(path)* function in Qt. It creates a virtual circuit inside the FPGA and establishes the input and output addresses used for communication with Romulus, thus controlling the detector electronics, the inclinometer and the cylindrical phantom, and managing the data flow from the readout system. The scope and development of the firmware is explained in depth by Petasecca et al. (2012).

There are four types of instructions for communication with the readout system, as defined in the API: uploading firmware, inputs (wire-ins), single outputs (wire-outs), and datastream output (pipe-out). The structure for the API commands is as follows:

```
//firmware upload
ConfigureFPGA(std::string PathToFirmware);

//parameter input
SetWireInValue(int endpointAddr, int value, int mask);
UpdateWireIns();

//variable output
UpdateWireOuts();
GetWireOutValue(int endpointAddr);

//datastream from FIFO
UpdateWireOuts();
ReadFromPipeOut(int endpointAddr, int length,
                unsigned char *data);
```

The endpoint addresses used for these commands need to be agreed on by both the firmware and software developers. It is worth noting that the “endpoints” here should not be confused with the endpoints in the USB protocol; they are different. The *SetWireInValue* command accepts 16-bit decimal or hexadecimal parameters (up to 65535 or 0xFFFF for this DAQ system, although the FPGA is capable of 32-bit commands) and prepares the value to be sent to the *endpoint* on the FPGA.

This command has the capability of updating individual bits in the *endpoint* using the *mask*. Thus, multiple parameters, such as flags, can be configured using the same address, by modifying individual bits in that address. For example, the flag (boolean) for single or continuous acquisition can be the least significant bit of address *0x02*, while the flag for the use of internal or external sync trigger can be the third last significant bit of the same address. These two bits can be updated individually, or simultaneously using one SetWireInValue command with the mask 0x03 (Table 3.1).

Table 3.1: Example of masks used for settings which share a common destination address on the firmware

	Command bits	Mask
Both flags	0101	0x05
Only flag 2	0100	0x04
Only flag 1	0001	0x01

Table 3.2: Structuring of serialised data for (a) TERA based readout; and (b) AFE based readout

Header 0xFFFF 0xAAFF	Ch_0	Ch_1	Ch_2	...	Ch_{127}	Header 0xFFFF 0xBBFF	Inclin.	Opt.Enc.

(a)

Header 0xFFFF 0x003F	Ch63 AFE00	Ch63 AFE01	Header 0xFFFF 0x003E	Ch31 AFE00	Ch31 AFE01	Header 0xFFFF 0x003D	Ch62 AFE00	Ch62 AFE01	Header 0xFFFF 0x003C	Ch30 AFE00	Ch30 AFE01	...	Header 0xFFFF 0x0000	Ch0 AFE00	ch0 AFE01	Header 0xFFFF 0xBBFF	Inclin.	Opt.Enc.

(b)

Table 3.3: Logical sorting of data in the unmapped datafile

#ch	date	comments					
AFE0 Ch0	Ch1	...	Ch63	AFE1 Ch0	Ch1	...	Ch63
frame 0							
frame 1							
frame 2							
...							

The *GetWireOutValue* command requests the value from the FPGA at a particular address. For example, if the value of the angle of the inclinometer is configured to be accessible at address *0x19*, then the command *GetWireOutValue(0x19)* will return an integer which is directly proportional to the inclinometer angle, and which can be converted to degrees by applying a simple coefficient.

The *ReadFromPipeOut* command requires multiple parameters for data output: the pipe-out address pointing to where the data resides in the FPGA, the number of bytes to read, and container in which to place the data. The data is in raw binary and needs to be decoded before being displayed on the GUI; this will be covered below.

For the AFE data format, the header index is within the range 0-63 and it represents the number of channels on the AFE chip. Depending on the number of channels the user wishes to use, which dictates how many AFE chips are enabled for acquisition (2 for 128-channel, 4 for 256-channel, 8 for 512-channel), each header is then followed by the channels with identical index from all the connected AFE chips in consecutive order. Table 3.2 shows the example for 128-channel data format, where channel 63 from both chips follow the first header. For 512-channel data, there would be 8 channels following each header. One container with complete data from all the channels is referred to as one *frame*.

3.2.6 Data Decoding

To decode the data from each pixel, a simple operation for converting between base 256 to base 10 must be performed with a deserialisation procedure for a

correct mapping of the channel to its physical position on the detector array. For example, if the value as unsigned chars for pixel 15 is ‘A0’, then this word can be separated in the two bytes ‘A’ and ‘0’. These bytes correspond to the integers 65 and 48, respectively, when converted to a decimal number (type casting). The final step to reach a decimal number is to multiply the most significant byte by 256 and add to the least significant byte. Thus, 65 multiplied by 256 and added to 48 yields 16688, which is the value of pixel 15 in decimal.

When the data is decoded from base 256 to base 10, it goes through a number of steps. The data is converted from raw number to percentage of the dynamic range pre-selected (gain) and then it is saved to a number of text files. The first line of all files contains in tab-delimited format the number of channels, the date and time of acquisition, and any comments associated with the measurement. The first text file contains the default output from the AFE converted in percentage of dynamic range. The arrangement of the pixels in this file is dependent on the routing of the detector used; for example in the case of MP121 detector, pixel 1 connects to channel 1 of the AFE, pixel 2 connects to channel 2, etc. (Fig. 3.9), while for MP512, pixel 1 connects to an AFE channel corresponding with the shortest possible physical wire between the two, due to detector wiring constraints on the PCB. The pixels are tab-delimited in the file, where each column corresponds to one pixel. Every row in the column corresponds to a frame at a particular time after the measurement is commenced, which depends on the sampling frequency of the detector. The columns are arranged with channel 0 from AFE0 on the first column (left) and ending with channel 63 on AFE7 in the last column (right), for a total of 512 channels (Table 3.3).

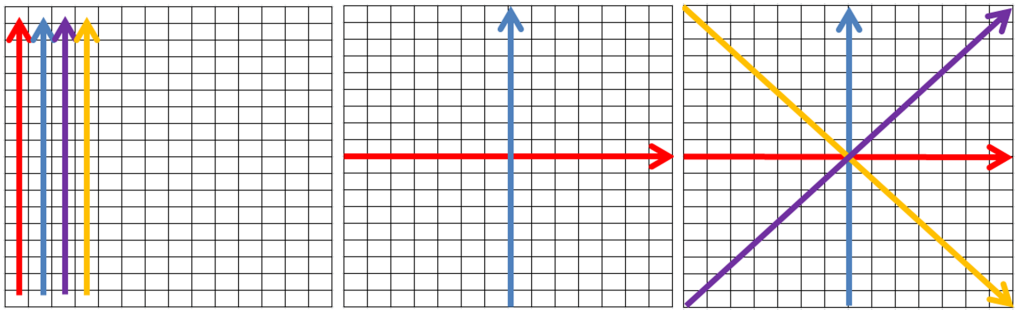

(a) (b) (c)

Figure 3.9: Diagram of the data saving pattern on a 2D grid for (a) MagicPlate 121 & 512; (b) DUO; and (c) OCTA detectors. The color of the arrows shows the direction of the pattern, starting from red; then blue; purple and yellow

The second text file is the detector-dependent output and contains the same columns as the first; however they are rearranged to form a logical pattern which corresponds to the detector used (Fig. 3.9). This is determined by the mapping mask in Romulus file output and is dependent on the user choice of detector. A third text file containing debug raw data is also outputted. Data is stored the same as in the first text file, however the ADC response is left in raw differential format and not converted to percentage of dynamic range. Two extra files can be created if the user loads the equalisation factors into the GUI, corresponding to the default configuration of the GUI, and mapped arrangement, with the equalisation factors applied to the data.

3.2.7 Equalisation Factors

The semiconductor detector arrays used in this project are comprised of multi-channel pixels whose responses are slightly different from one another due to local substrate heterogeneities and parasitic capacitance associated with the connection

routing. Moreover, each pre-amplifier channel has a variation of the gain which can vary within 0.1% to 0.5% of the dynamic range (Texas Instruments, 2009). To mitigate this issue, a protocol has been developed to obtain a per-pixel correction factor which can be applied to ensure a smooth, uniform response of the detector. These equalisation factors are then stored to a file and can be re-used if necessary.

This feature is available in the menu section of Romulus, under Tools. The procedure involves irradiating the detector with a large field using a clinical linac at 10 cm equivalent depth in water, where the radiation field is uniform. The typical field used for this procedure is a 20 $\times$ 20 cm^2 square field. This way, we can assume that all the pixels will observe the same dose and any differences in response are solely due to the electronics or intrinsic pixel properties. By taking an average of the pixels response <X>, the ratio between the average and the individual response yields a per-pixel coefficient for the equalisation, F_i. This can then be applied to each pixel to obtain its equalised response, $(Y_{eq})_i$:

$$F_i = \frac{X_i}{< X >}; (Y_{eq})_i = \frac{X_i}{F_i} \tag{3.1}$$

The equalisation factors are stored in a tab-delimited file of extension *.calib*, starting with channel 0, and depending on the detector used, the file will be populated with 128, 256 or 512 coefficients. Loading the factors can be done from a *.calib* file, but it can also be loaded from a previous acquisition measurement with the *.bin* extension. The latter performs the data decoding and stores it in a temporary file, determines the average response and outputs the equalisation factors in a final *.calib* file.

3.2.8 Mapping of Detectors

The 512-channel detectors MagicPlate-512, DUO and OCTA all have different pixel positions on the detector plane and their PCB wiring is optimized to minimise distance from the pixels to the electronics. Unlike MagicPlate-121 and DMG, which have a direct correlation between the pixel number and the associated channel number, the wiring of the 512-channel detectors resulted in a very complicated logical sorting of the pixels with respect to the corresponding electronic channel. The datasheets obtained from the CMRP microelectronics foundry provided the pinout of the high-density connectors; these had to be correlated with the female counterpart on the electronics and the sequence of preamp channels of the AFE. This process was then verified experimentally using the setup shown in Fig. 3.10.

The correlating procedure was performed in order to realise the mapping of the detectors and to establish the software re-routing to visualise the data in 2D. The GUI thread in Romulus receives the frame from the ACQ thread during measurement, decodes it and passes it through a function which rearranges the pixels in a new array, depending on the detector chosen. Each detector has its own corresponding rearrangement mask. The new array is then passed to the plot, which visualises the data accordingly.

Once the software mapping algorithm was completed, it was verified experimentally using laser optical stimulation (Fig. 3.10). A green laser of beam diameter 0.5 mm and variable intensity was used to raster-scan in x-y across the pixels to verify the software mapping.

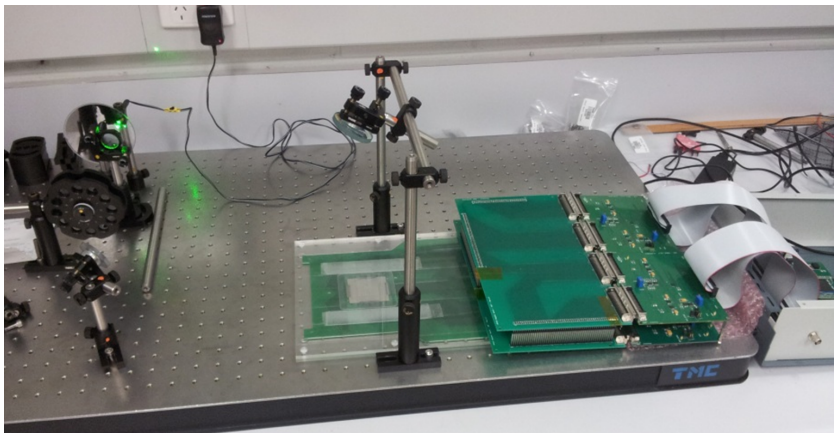

Figure 3.10: Experimental setup adopted for verification of the detector mapping by the means of a focused laser. The green laser passes through a series of filters before being guided using the reflecting mirrors onto the detector to allow for scanning of the detector surface.

3.2.9 The ACQ Thread

In previous DAQ software before the Romulus release version, the class and functions responsible for querying and retrieving detector data from the FPGA were part of the GUI, which in turn was updating the graphs with the real-time data; this single thread was responsible for all of the software's functions. However, upon investigating the raw data files from the detector, it was found that this approach induced data losses due to the long processing time of the GUI data when decoding and plotting, which was preventing the software from acquiring all the frames from the FPGA's FIFO. About 10% of frames were lost per measurement, and it was unclear which section of the measurement they were missing from. Thus, the data handling code was separated from the GUI code by the use of separate threads. Since most modern computers and laptops have processors with two or more cores, this approach ensured that data loss was completely prevented. The data acquisition and storage code was moved in the ACQ thread and was sep-

arated from the GUI code, making use of Qts signal-slot capability to establish inter-thread communication.

In principle, the ACQ code is very simple. A class is used to contain all the measurement parameters from the user input and received from the GUI; the *commence()* signal triggers the execution of a function named *process()*. The *process()* function configures the FPGA by passing the user preferences and signals to the FPGA to start acquiring. Fig. 3.11 shows a flowchart of the core ACQ function responsible for Romulus' data acquisition.

When acquiring, an output file is created and opened for writing using the user-specified filename, and a while loop is created which constantly queries the FPGA if it has new data in the FIFO. If the flag is true, the data is requested from the FPGA and stored to the open file. Every 100 milliseconds, a timer triggers a signal to be sent to the GUI thread from the ACQ. This signal contains a data frame which will be decoded and displayed to the user in real-time in the GUI.

Once the measurement duration set by the user has elapsed, the while loop terminates, the output file is closed, the function exits with an emission of a *finished()* signal and the measurement is concluded. If the user chose to automatically decode the data at the end of the acquisition, a signal relaying this information is emitted and captured by the decoding function, which executes the task. Romulus then resumes idling whereby accepting user input and waiting for the next measurement.

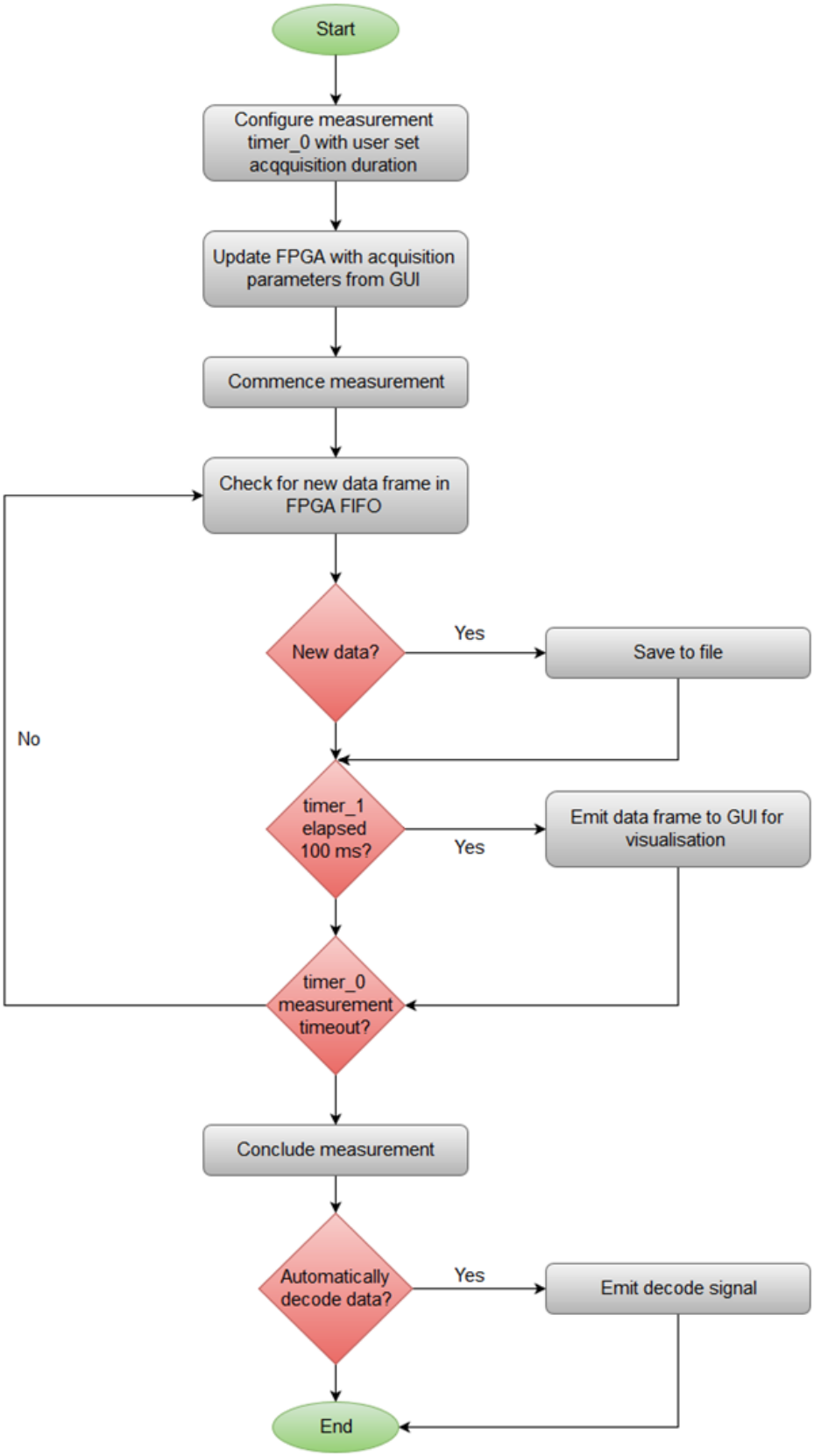

Figure 3.11: Flowchart diagram of the data handling function which comprises the core of the acquisition thread

3.2.10 The GUI Thread

The user interface thread, or GUI thread, is the code responsible for handling the user inputs, real-time visual updates and post-processing. The GUI thread triggers the ACQ to take a measurement, at the request of the user.

There are two main sections of the GUI, each contained in its own window: the acquisition mode, and the off-line data analysis mode.

3.2.10.1 GUI: Acquisition Mode

The Romulus acquisition window is comprised of four main areas: Menu options at the top of the window, the real-time data plots, the user input parameters and the status notification, including the status bar at the bottom. The most common measurement parameters such as file name used for saving the data, comments associated with the current measurement, duration of measurement and integration width can be found on the bottom-right of the window. Additional advanced settings can be accessed and set from the top menu. In the top-right, there is a visual Status label which informs the user whether the device is powered on, connected, or ready for measurement. Table 3.4 shows the colors associated with the various statuses of the system. The status bar at the bottom of the window provides short-term feedback for user actions, such as decoding status and confirmation if equalisation factors have been applied successfully. Based on the detector connected, the user can choose which graph layout to use from the top menu. The graphs are available in two forms: the frame-by-frame response, and the integral response. This applies to 1D and 2D graphs as well. Romulus saves a *.cfg* config-

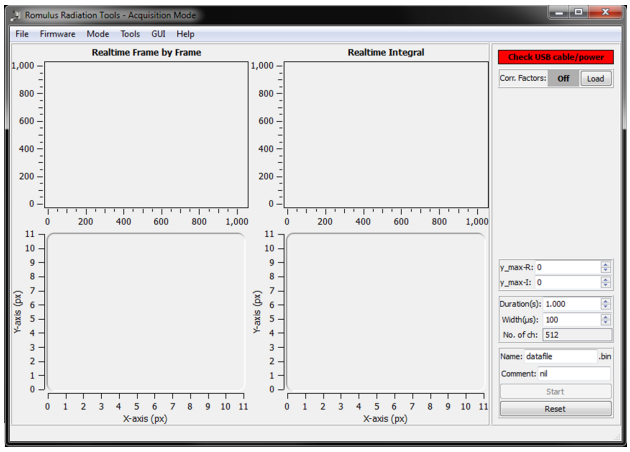

Figure 3.12: Screenshot of Romulus Radiation Tools software showing default window

uration file in the folder of the executable to recall position, size and visibility of GUI windows when it is restarted.

The parameters that the user can modify are:

- Number of channels to use (depends on detector but can be defined separately in case the user would like to visualize only a section of the detector connected.)
- Detector used (and thus graphing and 2D mapping)
- Loading of firmware
- Duration of acquisition
- Integration width
- Name of output file
- Comments associated with acquisition
- FIFO buffer size
- Sensitivity (gain) of ADC
- Choice between internal and external trigger
- Frequency of sampling
- Phantom motor power
- Zeroing of optical encoder
- Zeroing of inclinometer
- Inclinometer reset
- Loading of equalisation factors

- Automatic or manual decoding of data
- Plot ranges
- Plot zooming/panning
- FPGA/acquisition reset

To acquire a measurement, the user connects the electronics to the computer and powers on the system. When launching Romulus, it will inform the user using the status label if the device is connected, and if it is, the device's serial number will be available for query, and it will prompt the user to load the firmware in the FPGA (Table 3.4). The status label will turn green to show that the electronics is ready. The user will then set the desired duration, sampling frequency, trigger mode, integration window, file name and optionally comments, followed by pressing Start button.

The status label will inform the user that the acquisition is in progress and will display how many seconds are left. The user has the choice of terminating the acquisition prematurely by pressing the Stop button or letting it finish. If the *auto-decode* flag is enabled, Romulus will automatically perform the conversion to decimal when the acquisition is complete; alternatively, the user can manually decode the data at a later time.

3.2.10.2 GUI: Data Analysis Mode

The off-line post-processing tools component of the GUI is separate from the DAQ. The post-processing mode, or data analysis mode, allows the user to analyse the detector data on a per-pixel basis, or visually using 2D mapping of the detector arrays, and has statistical analysis tools available for finding average response,

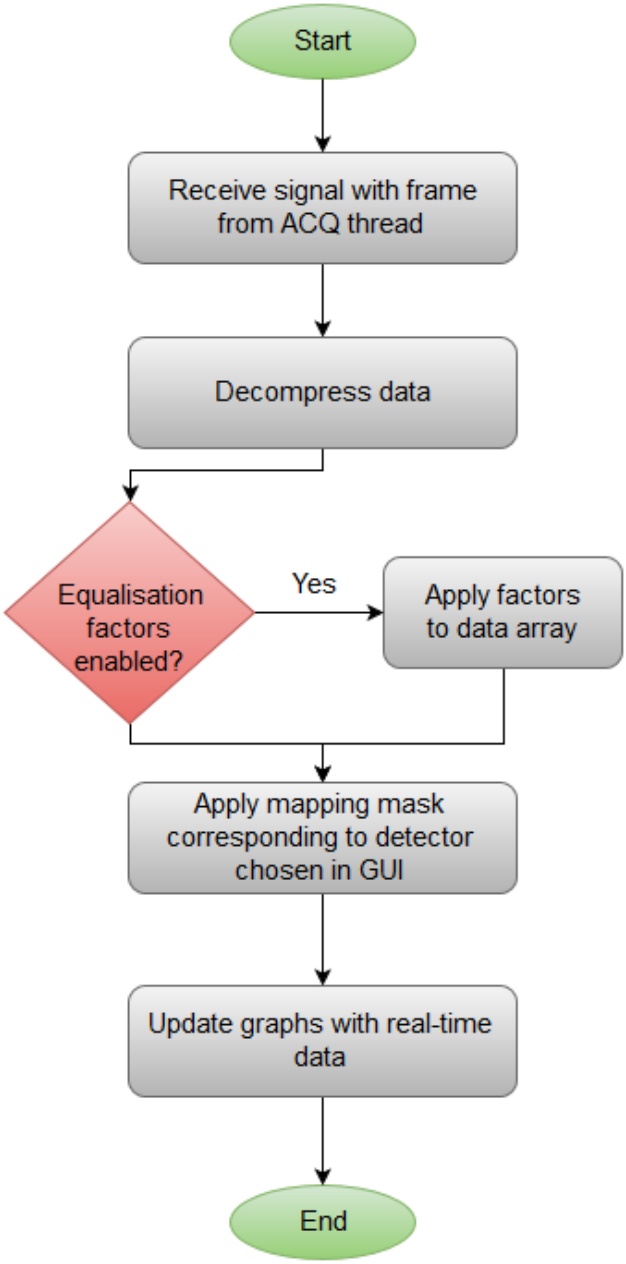

Figure 3.13: Flowchart of real-time visualisation function in DAQ thread

Table 3.4: Colors used by the GUI Status label to provide feedback to user of what instruction the software is performing at that time

Status	Color
Check USB cable/power	Red
Device connected	Light green
Load/Reload firmware	Blue
Ready	Green
Acquiring	Yellow
Terminated	Orange
Decoding	Dark green
Obtaining corr. factors	Yellow
Creating .calib file	Light yellow
ATTENTION	Red

standard deviations and integral dose. Each detector has its own dedicated 2D map, based on the geometrical configuration of the pixels. For example, the 512 channels for the DUO are arranged in a cross shape, while for the MP512, they are arranged in a square array.

The default graphs shown are the response versus channel number, unsorted, and response versus time for a user-defined pixel number. 2D graphs showing the frame-by-frame and integral response can be shown at the user's request, using the *2D maps* checkbox on the right. A horizontal slider allows the user to cycle through all the frames individually to analyse the pixel response and 2D maps of the beam. A detailed analysis of the pixel response can be done using the Statistical Analysis toolbox, which can be accessed from the bottom-right of the window. The toolbox is the core feature of the statistical analysis performed by Romulus, as it performs mathematical operations (summation, average, standard deviation, baseline subtraction) on the data from the graph that displays the tem-

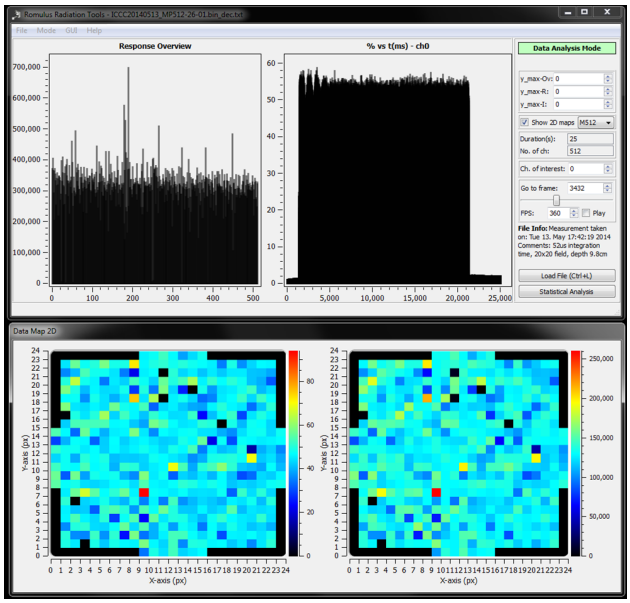

Figure 3.14: Screenshot of Romulus Analysis Mode window and the pop-up 2D mapping window showing MP512 response

poral response of the pixel, to quantitatively determine the dose received by the detector. A region of interest can be selected on the graph using the *Select ROI* button, which creates a "rubber band" using the mouse position, and the toolbox automatically outputs the number of frames inside the ROI, the duration, charge collected, average response, uncertainty based on two standard deviations, and integral response. The latter is directly proportional to the dose. If a ROI is defined using a constant time difference between the two reference points, then a point of interest feature exists, where the time window is pre-set to a certain value and a single point is selected on the graph. The ROI can also be set using the preferred time flags using the two Limit input boxes.

A baseline subtraction can be performed by choosing a ROI on the graph with background counts and subtracting the average counts from every frame. This can be undone by pressing the button again. The baseline subtraction ensures that any

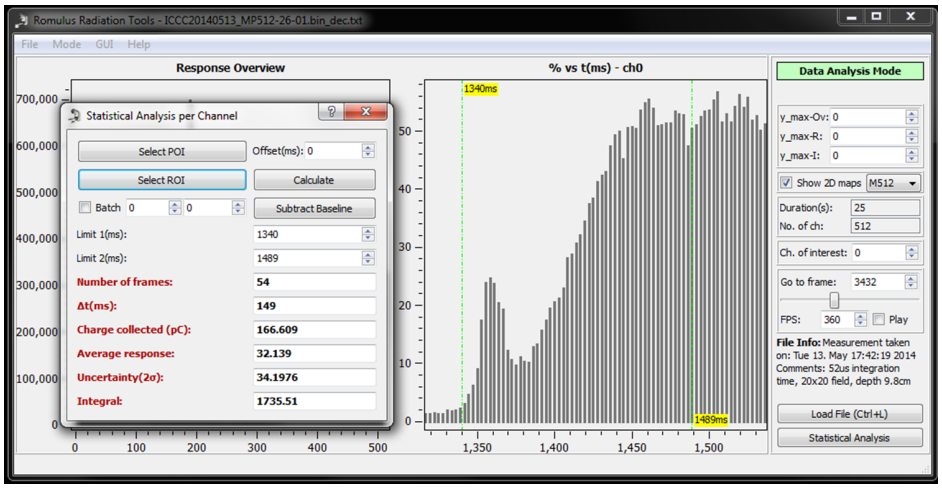

Figure 3.15: Screenshot of Romulus showing the response versus time for a chosen pixel (background) and the statistical analysis window (foreground)

noise present in the pixel's response can be removed. There is a batch function which automates the procedure for all the pixels of the detector. Two input boxes next to the batch checkbox allow the limits to be set, in milliseconds, for the region of interest where to obtain the integral response for each pixel. Because the beam is turned on across the detector at the same time, choosing one ROI is generally acceptable for all pixels. The batch data gets saved in a tab-delimited text file, with the integral response from each pixel, which can be further analysed.

3.3 Applications of the Unified DAQ System

3.3.1 MP121 and Dual Verification

The application of the MagicPlate-121 for use in IMRT/VMAT as a fluence detector mounted on the linac head, and as a dose detector in a phantom, will be

described in Chapter 4. The thin detector will be used for verification of the transmitted beam shape and intensity, and a simultaneous verification of the dose distribution from a second MP121 detector inserted in the central plane of a cylindrical phantom will be performed in comparison with treatment planning software (TPS) distribution in that plane.

3.3.2 MP512, DUO, OCTA and SBRT/SRS

The characterisation of detectors MagicPlate-512, DUO and OCTA will be presented in Chapter 5. The characterisations described will include electrical I-V and C-V traces, linearity, uniformity, spatial resolution, temporal resolution and charge collection efficiency. The verification of dose distribution in a plane using MagicPlate-512 for small stereotactic low dose rate photon beams will be described in Chapter 6, and the application of MagicPlate-512 detector for use in stereotactic motion adaptive radiotherapy will be described in Chapter 7. The latter will evaluate the performance of the MP512 detector in a case study performing QA using a lung motion phantom.

3.4 Conclusion

In this chapter, the realisation of the data acquisition software for a prototype dual-verification quality assurance device was presented and hardware elements comprising the prototype were described. The two readout systems for the device based on different ADCs were outlined and their differences described. The de-

tectors used in this work were described in detail. The final assembled device was shown in a clinical environment.

The QA device is intended to be used for quality assurance in IMRT and VMAT modalities, as well as small-beam stereotactic radiotherapy. The device will be utilised in a number of studies, as described in the following chapters. Future work relating to the acquisition software includes the importing of treatment plan data from the planning system into Romulus, and 3D dose reconstruction in the phantom by back projection and forward projection using the response of the linear array in the center of the rotatable phantom.

Chapter 4

Application of the MagicPlate System as a Dual-Verification Quality Assurance Device for Intensity Modulated Radiotherapy

4.1 Introduction

Quality assurance in radiotherapy is performed using commercially available detectors and dosimetry systems, such as ionisation chambers, film, gel, array detectors such as MapCheck, Delta^4, ArcCheck, etc. In light of the limitations of the commercially available detectors as outlined in the literature review in Chapter 2, a solution is proposed by CMRP which addresses these shortcomings by developing a prototype dual-verification quality assurance device for IMRT and VMAT which eliminates the angular dependency of dose measurements, and that can also be used intra-operatively to verify the radiation treatment as it is being delivered by the linac. In this chapter, the novel QA approach named the MagicPlate Dosimetry System (MPDS) is presented. MPDS is based on the semiconductor array detector MagicPlate-121, and is capable of performing pre-treatment as well as intra-operative QA as a transmission detector. This chapter describes the system and presents results which validate the principle of operation of the system.

4.2 Materials & Methods

The purpose of this study is to perform pre-treatment QA with two detectors in transmission mode (MPTM, mounted on gantry head) and dose mode (MPDM, measuring the response inside the phantom) (Fig 4.1), and intra-operative real-time QA with the transmission detector mounted on the linac head, while following the gantry rotation to eliminate the angular dependence of the detector. The expected differences in response operating the detector in transmission and dose

mode are related to the type of material surrounding the detector and the presence (or lack) of charged particle equilibrium. In the phantom, the MPDM array will be detecting a response very similar to that of tissue, while the MPTM will show a response which will be indicative of the fluence of the beam, less the dose. MPTM can also be subject to gantry head scatter from collimators and shielding, which is not covered in this study. The ability of the MP121 to determine the dose in the phantom with respect to the treatment planning system (TPS) dose will be determined, as well as the ability of the system to detect errors in the real-time delivery will be tested. The latter will be performed by introducing a known error in the linac dose rate and observing the response of the transmission detector. Due to the fact that the QA device does not have TPS importing capability at the time of performing this study, the verification will be done by comparing the pre-treatment QA result, which is verified against the TPS, with the *in-vivo* real-time data from the detector.

4.2.1 MagicPlate-121 Detector

The 11 $\times$ 11 epitaxial array MagicPlate-121 has been described in Section 3.1.1. Two copies of the detector are used in this study: one placed in the phantom for dose acquisition, and one mounted on the linac head and used for transmission mode measurements. The perturbation induced by the MP121 detector being inserted in the beam next to the linac exit window is less than 1% (Wong et al., 2012; Alrowaili et al., 2015).

(a) (b)

Figure 4.1: (a) The MagicPlate system, showing the MPDM inserted in the rotatable phantom on the patient couch (disengaged; not following the linac head), and the shielded MPTM mounted on the linac head; (b) the system following the linac head.

4.2.2 Readout System (TERA)

The readout system of the detector adopted for this experiment is based on the TERA6 front-end and has been described in Section 3.1.7.

4.2.3 Rotatable Phantom System

The rotatable phantom designed by CMRP has been used to provide water equivalent environment for the inserted MP121 detector which measures delivered dose. It is comprised of the PMMA drum, SolidWater inserts surrounding the detector, driver motor, optical encoder and inclinometer, and has been described in Section 3.1.6.

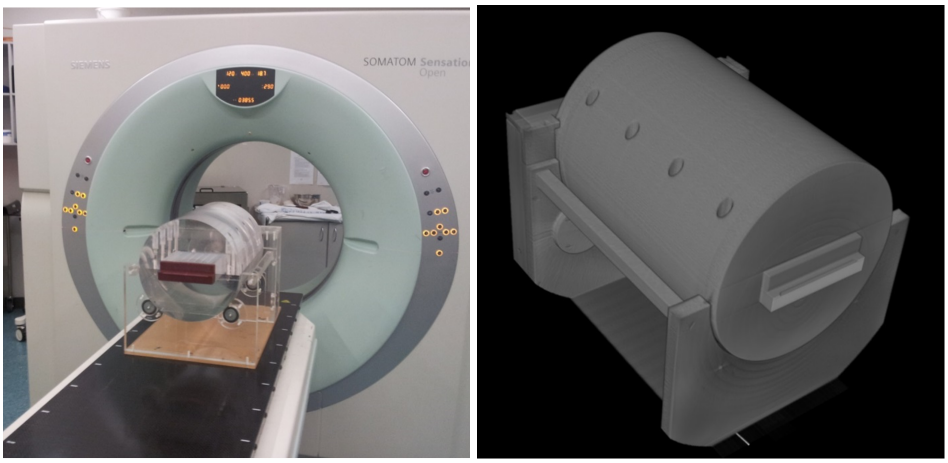

(a) (b)

Figure 4.2: (a) Rotatable phantom placed on a Siemens CT couch to be imaged. Optical encoder and motor were removed to avoid imaging artifacts in the CT scan due to the high-Z materials; (b) the CT image of the phantom which was imported into the TPS.

4.2.4 Rotatable Phantom Electron Density Map

In order to perform treatment planning (TPS) with the CMRP phantom, it had to be scanned by a Computer Tomography (CT) simulator and its volume, with associated densities, imported in the TPS. The rotatable phantom has been scanned using a Siemens SOMATOM Sensation CT scanner, in order to obtain the CT numbers of each voxel required for treatment planning. The voxel volume used was $2 \times 2 \times 2$ mm^3. The data was exported in DICOM files of dimension 512×512 pixels, which corresponded to 1.024 px/mm.

4.2.5 Treatment Planning

The Pinnacle^3 by Philips was the TPS used to perform the treatment planning. CT data for the rotatable phantom was imported and a treatment plan consisting

of a 5 $\times$ 5 cm^2 photon beam of 6 MV, 600 MU/min and delivering 100 MU was created. The gantry angle for the beam is 0° and the isocenter of the beam corresponds with the center of the phantom, and thus, the center of the detector. The plan was delivered using a Varian 2100EX clinac at Illawarra Cancer Care Centre, Wollongong, Australia.

4.2.6 Experimental Setup

The calibration factor (counts/cGy) was obtained for MPDM, by irradiating the detector at standard conditions using the linac. The standard conditions represent the set of parameters that are chosen to have, in a specific point in a solid water phantom, 1 MU/cGy. For a 6 MV linac with the detector placed on top of 10 cm SolidWater backscatter and depth 1.5 cm (d_{max} for 6 MV), source to surface distance of 100 cm (SSD), and irradiated with a 10 $\times$ 10 cm^2 field at 600 MU/min. We delivered a total dose of 100 MU or 100 cGy in such conditions. The calibration factor recorded corresponds to the amount of charge collected by the detector, which is directly proportional to the dose delivered at that depth.

The equalisation factor of the detector, as described in Section 3.2.7, was obtained by keeping all of the irradiation parameters the same, except for moving the detector at 10 cm depth and using a 20 $\times$ 20 cm^2 field. At these conditions, the dose distribution can be considered flat within 1% variation across the entire field. The equalisation factors were used to eliminate any variations in the response due to different intrinsic properties of the individual pixels.

The rotatable phantom was placed underneath the linac head with the center of ro-

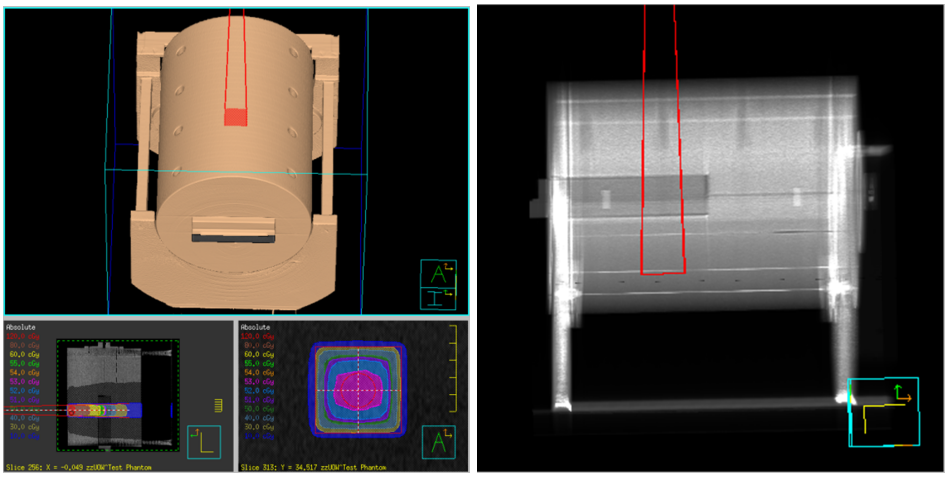

(a) (b)

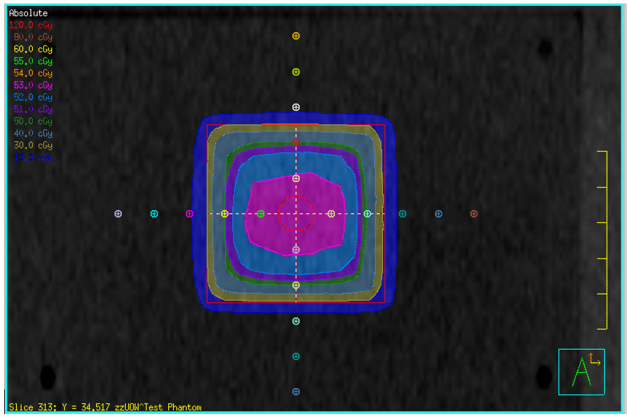

(c)

Figure 4.3: (a) (b) Screenshots of Pinnacle treatment planning software showing a 5×5 cm^2 6 MV photon beam incident on, and traversing through, the cylindrical phantom; (c) isodose curves at the depth of the MP121 detector inside the phantom. The points along the horizontal and vertical plane of the profile are 1 cm apart and denote the sample points for the TPS and MP121 profile comparison.

tation correspondent to the isocenter of the linac. The phantom was set to follow the linac gantry and its "home" position set to be 0 degrees when the linac head is perpendicular to the patient couch. The detector is then horizontal and parallel to the patient couch guarranteeing the beam perpendicular to the beam. This function has been implemented within the firmware of the system in order to maintain a normal angle of incidence between the photon beam and the 2D detector at all times. The ability of the phantom to follow the linac head has been investigated by rotating the gantry from 0° to 45° and back to evaluate the effects of the backslash of the belt driving system. The differences between the gantry head angle (inclinometer) and phantom angle (optical encoder) were recorded and compared.

When performing radiotherapy at the hospital, prior to irradiation of the patient, the pre-treatment quality assurance routine is performed. The MPDM obtains a dose map of the beam, while in parallel the detector mounted on the linac head records the 'fluence' of the beam as a function of time, as the treatment is being delivered (Alrowaili et al., 2015). The response of the detector in the phantom is then compared to the TPS and if it agrees, the data from the transmission detector is stored in Romulus, where it acts as the reference "fluence" map for the real-time *in-vivo* measurement. A threshold of 10% is placed on the difference between the planned and delivered fluence per frame, and if the latter exceeds the threshold, the system will warn the user and recommend shutting down the beam. The threshold can be varied on a per-treatment basis by the user.

A 50 MU plan has been generated in the TPS and two versions of the plan were delivered to the phantom. The first 'treatment' was according to the reference TPS plan and its purpose was to verify the reproducibility of the system. The second

treatment had a known error introduced, which was a 20% decrease in linac dose rate after the first 20 MU, to observe if the MPDS responds to the discrepancy. The result was plotted and compared. The response from the central pixel is presented in this study as a proof of concept, despite data being available from the entire array, in order to simplify the presentation of results. In a real QA scenario, the response of all the pixels would be compared to the verified pre-treatment data.

4.3 Results

The data showing the phantom tracking the linac is presented in Fig 4.4. The agreement between the inclinometer and the optical encoder as a function of time is within ±1.5° except for two outlying sections. This demonstrates that the rotatable phantom successfully tracks the linac gantry as it rotates to deliver radiation. There are two regions on the curve at around 25° for both gradients, occurring at 6 s and 16 s into the measurement, where the encoder lags in one position for about 400 ms. This might be due to an irregularity on the transmission belt which is causing the phantom to stagnate shortly before catching up with the gantry. This uncertainty is not compounded to the surrounding points; it is localized to those regions around 25 degrees and does not affect the rest of the dataset.

The expected dose at the detector level inside the phantom is between 50 cGy and 53 cGy, according to the TPS, as shown in Fig. 4.3. Using the TERA readout system, the calibration factor was found to be 2350 ± 250 counts/cGy by measuring the response of the detector at ‘standard’ conditions prior to inserting it in the phantom. The MPDM was found to have a very uniform response after the

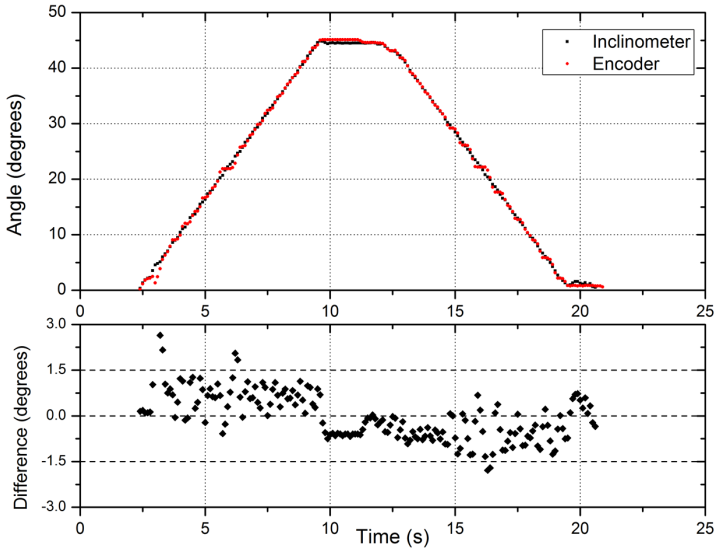

Figure 4.4: The angle of the linac gantry (inclinometer) and phantom (optical encoder) as a function of time. The difference in the positions is less than 3° at all times.

equalisation factors were applied, as shown in Fig. 4.6. The response of the pixels in the 5 × 5 central region was in the range of 124000 ± 2000 counts, which corresponds to 52.8 ± 0.5 cGy. The dose drops off to about 9 cGy to 10 cGy in the out-of-field region close to the penumbra, which is in good agreement with the TPS. The response across the profile of the MP121 compared with the TPS agrees within 1.3% for the lateral (horizontal) profile, and 3% in the penumbra region. The sup-inf profile (vertical) agrees within 1.3% in the interumbra region, and within 1% for all other points. The profiles are shown in Fig. 4.5. Errors are shown by the size of the points, and are due to statistical uncertainty between repeated measurements (two standard deviations).

The response of MPDM and MPTM as a function of time are shown in Fig. 4.7. The response of the detector in the phantom is larger compared to MPTM, as expected, due to the charged particle equilibrium which is reached in the Solid

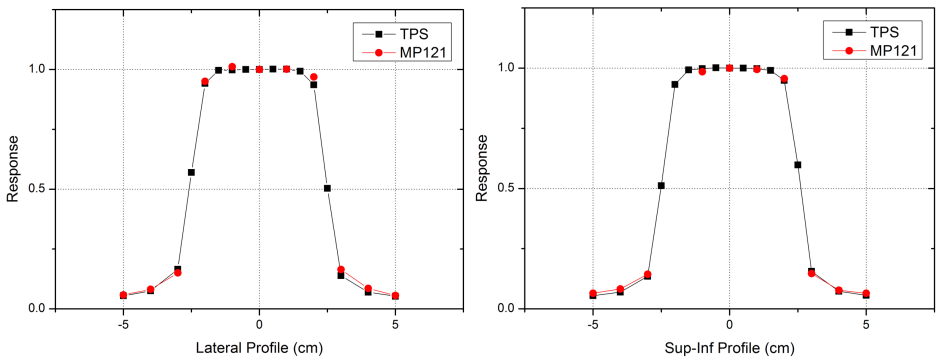

(a) (b)

Figure 4.5: Comparison of profiles of planned dose by TPS and delivered dose by linac, for horizontal profile or right-left profile (a) and vertical profile (superior-inferior) (b). The response is normalized to the central pixel.

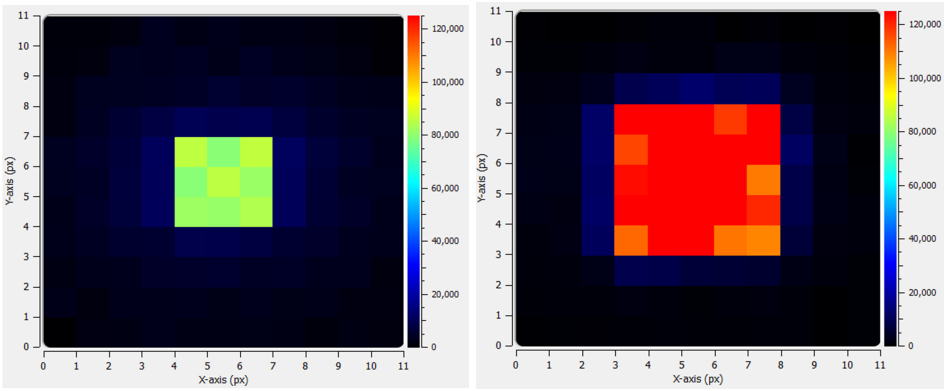

(a) (b)

Figure 4.6: Response in counts of MP121 in transmission mode (a) and dose mode (b) for 50 MU delivered dose by 5×5 cm^2 beam, as displayed in Romulus. The color scale is identical for the two plots.

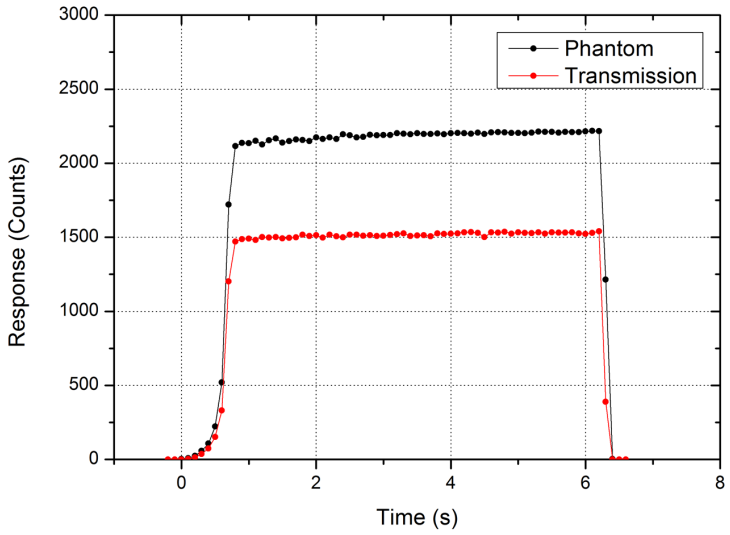

Figure 4.7: Response of the central pixel for both transmission and phantom detectors as a function of time. The response in the phantom is clearly higher due to the charged particle equilibrium. When the transmission response is normalized to the dose response in phantom, the differences in the curves are less than 2% per frame.

Water phantom. This equilibrium is not present above MPTM because the detector is surrounded by air, which has a much smaller cross-section of interaction of the x-ray photons in comparison with the phantom.

4.3.1 Error Evaluation

Fig. 4.8 shows the response of the MPTM as a function of time for the pre-treatment (control) phantom measurement and the two test measurements. There is a slightly larger difference at 0.6 to 0.7 seconds between the control and the test measurements in the transient build-up region of the curve; this is due to the integration time of 100 ms used in these measurements which is very large compared to the pulse repetition rate of 360 Hz for Varian machines. Thus when

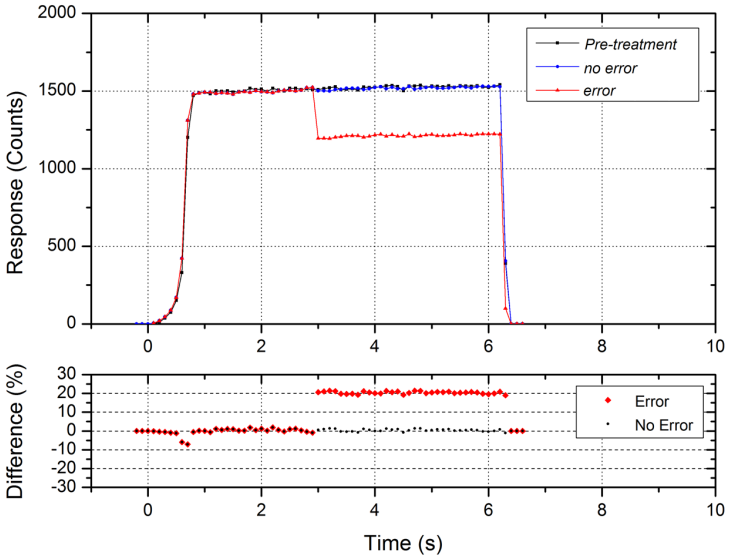

Figure 4.8: Response as a function of time showing the agreement between the MPTM pre-treatment measurement and two cases of real-time intra-operative measurements, one with error and one without error.

the sampling point with respect to beam-on varies by a few milliseconds between different measurements, it can induce large discrepancy in the high dose gradient transient region of the curve.

The response of the treatment plan without an error agrees within 2% to the control. The response of the plan with the introduced error clearly shows the 20% difference between the control and the linac real-time beam after the first 20 MU (3 seconds beam-on). The real-time response monitoring of Romulus successfully alerted the user of the unusually low dose rate observed during the delivery of the plan with the error, by means of visual warning using the status label, and a warning sound being played. The user was able to abort the treatment – manually or automatically, depending on the configuration in Romulus – before it continued to irradiate the target in an unexpected manner compared to the pre-treatment control. Thus the QA device was successful in identifying the deviation from the

pre-treatment QA using real-time response from MPTM that can be used during the patient treatment.

4.4 Conclusion

In this study, two MP121 detectors in conjunction with the rotatable phantom were used to validate the concept of a prototype dual-verification quality assurance device for intensity modulated radiotherapy, named MPDS. The device was able to perform pre-treatment QA to compare the delivered dose with the TPS, and also real-time intra-operative verification using one MP121 detector as a beam fluence monitor, configuration which is possible only thanks to the transparency of MP121 to the beam which is not perturbed by its presence (deviation inferior to 0.2% from nominal intensity (Wong et al., 2012; Alrowaili et al., 2015, 2016). The MPDM agreed with the TPS within 1% to 2% across the profiles, and the real-time intra-operative monitoring successfully warned the user of a 20% drop in dose rate during a measurement, which led to the user successfully shutting down the beam prematurely due to the unexpected and undesired quality of the beam with respect to the planned TPS dose. The system successfully tracks the movement of the linac gantry using the inclinometer and optical encoder within 3° at all times.

While one of the obvious limitations of the system is the low spatial resolution of the MP121 arrays (1 cm pitch), the study does demonstrate the proof of concept. Improvements to this study include the real-time verification of the beam for varying field size and delivered dose, introduction of rotation in a VMAT study

to assess the ability of the system to verify the treatment as a function of gantry angle, importing of the TPS data directly into the Romulus data acquisition software in DICOM format, and performing the QA with a detector that has a higher spatial resolution than MP121 with also a higher temporal resolution to improve the capability of detecting errors timely.

Chapter 5

Characterisation of 512-channel Monolithic Silicon Pixelated Detectors Magicplate-512, DUO and OCTA

Part of this chapter has been published in IEEE Transactions on Nuclear Science:
C.S. Porumb., M. Petasecca, M. Newall, A.H. Aldosari, I. Fuduli, P. Metcalfe, M. Carolan, M.L.F. Lerch, D. Cutajar, V.L. Perevertaylo, A.B. Rosenfeld, 2016, *Characterisation of silicon diode arrays for dosimetry in external beam radiation therapy*, **Accepted, May 10 2016** doi:10.1109/TNS.2016.2567446

5.1 Introduction

The Centre of Medical Radiation Physics has developed three novel monolithic silicon array detectors with different pixel configurations, high spatial resolution and small sensitive volumes. The detectors, coupled with the DAQ system developed by CMRP, attempt to address the limitations present in quality assurance of small-beam radiotherapy, such as the necessity for high spatial resolution and real-time feedback for multi-channel detectors. In this chapter, the characteristics of the detectors MP512, DUO and OCTA are investigated, to determine the performance and application of these detectors for use in SBRT. The chapter focuses on detectors MP512 and DUO for clinical characterisation, while for OCTA, the Charge Collection Efficiency (CCE) and charge sharing study has been performed. The clinical characterisation of OCTA has not been performed in this study due to a technical difficulty with the detectors high-density connectors at the time, which prevented the acquisition from the whole detector and thus, only test structure measurements have been performed.

5.2 Materials and Methods

5.2.1 Detectors

This study was performed using detectors of the family MagicPlate (three detectors with varying pixel-to-pixel pitch and arrangement of the pixel arrays). The detectors have been described in sections 3.1.2 and 3.1.3.

5.2.2 Readout System

The AFE-based readout system in conjunction with Romulus Radiation Tools was used to record the measurements of the detectors. The full description can be found in section 3.1.7.

5.2.3 Test Structures

In order to obtain the electrical characterisation and CCE of the individual silicon pixels, test structures of the central intersection of the detectors DUO and OCTA have been supplied by the CMRP microelectronics foundry. The test structures were manufactured from the same wafer from which the whole detector array has been produced. A p^+ back junction establishes a common back contact. The test structures were placed in a dual in-line (DIL) ceramic package, containing 13 pixels each, while the MP512 test structure contained 8 pixels. Two samples for each detector were available in this study. Two test structure samples with identical properties were used for each detector, for statistical purposes.

5.2.4 Pre-Irradiation Characterisation

In order the determine the variation of the properties of the detector as a function of the accumulated dose, a pre-irradiation characterisation has been performed in terms of I-V, C-V, and CCE.

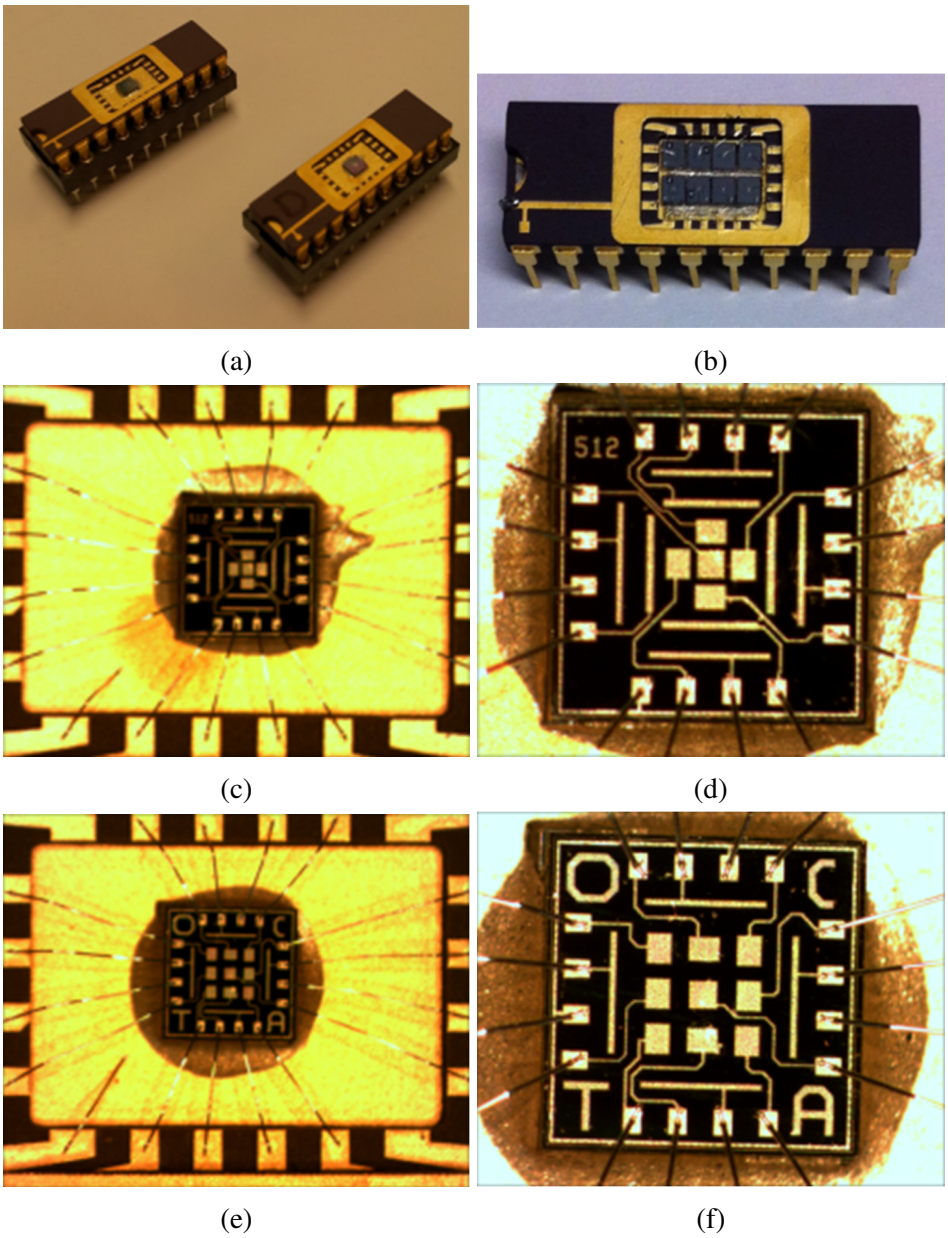

(a) (b)

(c) (d)

(e) (f)

Figure 5.1: (a) DUO and OCTA test structures; (b) MP512 test structure (top right); DUO structure enlarged (c)(d); OCTA structure enlarged (e)(f)

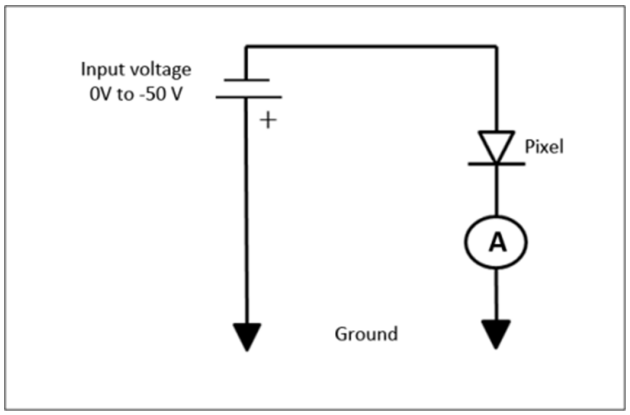

Figure 5.2: Circuit used for IV characterisation

5.2.4.1 I-V Characteristics

The current-voltage characteristics have been measured for DUO and OCTA test structures using a Keithley Semiconductor Measurement Unit (SMU) 237 at constant laboratory temperature of 24 °C. The I-V curves have been investigated in the reverse bias range of 0 V to -50 V in 1 V increments. A 1000 ms pause was introduced between varying the voltage and the readout of the pixels to ensure stabilisation of the pixel response. The test structures were placed in a dark Faraday cage made of aluminium to prevent electromagnetic interference and photocurrent generation due to ambient light.

A custom LabView interface was used to control the parameters of the measurements and to save the data. Uncertainties of the current-voltage data were dependent on the 5.5 digit accuracy scale of the instrument.

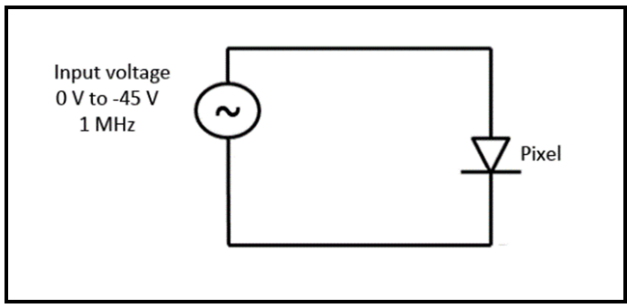

Figure 5.3: Circuit used for CV characterisation

5.2.4.2 C-V Characteristics

The capacitance-voltage characteristics were measured using a Boonton 7200 capacitance meter for DUO and OCTA test structures. The voltage range was 0 V to -45 V in steps of 1 V. To ensure full stabilisation of the pixel capacitance, a 2000 ms delay time was added between applying the bias and reading the response. The test structures were placed in a dark aluminium cavity which acted as a Faraday cage against electromagnetic interference and prevented ambient light from generating photocurrent electron-hole pairs. The capacitance meter was zeroed prior to each pixel readout. The measurements were performed at a constant laboratory temperature of 24 °C to replicate standard clinical operating conditions, and were controlled using a custom LabView interface which set the acquisition parameters and saved the data. Uncertainties were dependent on the 3.5 digit scale of the instrument.

5.2.5 Linearity

The ability of a radiation detector's response to be directly proportional to the incident dose is defined as linearity. An ideal detector is linear with respect to incident

dose (Bocci et al., 2012). The linearity of MP512 and DUO was investigated in this study in the range 50 MU to 500 MU in increments of 50 MU. The detectors were tested in 'standard conditions' in a Solid Water phantom. A Varian 2100 EX clinac was used to irradiate the detectors with a 6 MV beam. The readout system was synchronised to the linac pulses using the external trigger from the linac. The integration time used was 52 µs for MP512 and 100 µs for DUO, to maximise the detectors' SNR.

5.2.6 Uniformity

The detectors MagicPlate-512, OCTA and DUO consist of 512 pixels each; subsequently, the response from each pixel is different due to local substrate defects and pre-amplifier gain variation, as discussed in section 3.2.7. The uniformity of the detectors MP512 and DUO was investigated in this study by irradiating the detectors using a flat field and analysing the deviation of the pixels response. The detectors were placed in Solid Water at 10 cm depth and 10 cm backscatter and irradiated by clinical linac. A 20×20 cm^2 field was used to deliver 100 MU of radiation at 600 MU/min dose rate. In these conditions, the radiation field is completely flat and we are expecting that each pixel should read out the same response. The average response was computed and the result was presented as a statistical distribution of the differential response.

5.2.7 Radiation Damage

It is a requirement of medical radiation detectors to be as stable as possible during their life to avoid frequent and time consuming recalibration procedures. Change in response with respect to delivered dose by photon or electron MV energy radiotherapy beams is generally a problem that can be mitigated by delivering a pre-irradiation dose to the detector. Radiation damage studies were performed for MP512 and DUO using photons and photoneutrons generated by photon beams with energy higher than 10 MV. It is important to understand the amount of photon irradiation required to stabilise the response of the detectors. Due to the fact that silicon detectors are prone to radiation damage as described in Chapter 2, incident radiation such as photons and charged particles will induce damages in the silicon substrate in the form of atomic displacements in the lattice and cluster damage leading to electron-hole recombination centers and generation of trapped charge carriers in the SiO_2 dielectric. In the case of linac radiation with energy lower than 10 MV, point defects and positive charge accumulation in the silicon dioxide are the dominating types of radiation damage. Cluster defects may occur when operating the linac at high accelerating energies above 10 MV, when damage due to photoneutrons may occur. Sensitivity of the diodes drops dramatically as a function of radiation dose, and eventually stabilises after a several kGy.

Prior to commencing radiation damage study, the response of the MP512 test structures, as well as the MP512 and DUO arrays, were irradiated at 'standard conditions' and measured using Romulus DAQ software. To induce photon radiation damage, each device was irradiated by a Co-60 gamma source at the Gamma Technology Research Irradiator (GATRI) facility, at the Australian Nuclear Sci-

ence and Technology Organisation (ANSTO, Lucas Heights, Australia). MP512 test structures were irradiated up to 40 kGy water equivalent absorbed dose, in steps of 10 kGy. The best manufacturing combination of substrate type and *p*-stop implantation concentration was chosen based on results obtained with the test structures. Subsequently, the whole MP512 array has been tested for radiation hardness and results compared with the test structures for validation. DUO array was irradiated up to 140 kGy in steps of 20 kGy. During irradiation, temperature was kept constant at 30 °C and no bias applied, respectively.

The effect of photoneutron radiation was investigated using an 18 MV medical Clinac (Varian, USA) at St. George Cancer Centre (Sydney, Australia). Average neutron energies generated by linacs above 10 MV are in the order of 1 to 2 MeV and equivalent dose of 4.5 mSv per 1 Gy of photon dose at surface of water phantom (dErrico et al., 1998). The detector was placed in a 20×20 cm^2 field at 90 cm SSD at the surface of 10 cm thick solid water backscattering material. To maximise the exposure to neutrons and prevent thermalisation, no buildup material was placed on top of the detector. After each irradiation step of approximately 3000 MU at 18 MV, up to a maximum irradiation of 9795 MU corresponding to approximately 2×10^{10} n/cm^2 (1 MeV equivalent) photoneutrons, the detector response was tested in standard conditions by a 6 MV photon beam.

5.2.8 Charge Collection Efficiency and Charge Sharing

The charge collection efficiency (CCE) and charge sharing study was performed by means of ion beam induced charge collection (IBICC) for DUO and OCTA,

using their associated test structures. IBICC is a spectroscopy technique based on the stimulation of a charge pulse generated by the interaction of charged particles inside the semiconductor detector substrate. The particles are focused on a area of approximately 1 μm and the system records the position of the pencil beam and the corresponding amplitude of the response of the detector when the beam is at that position. The co-registration of position and amplitude of the response allows for the creation of a charge collection efficiency map of the detector. Please refer to Cornelius et al. (2013) for further information. The study was performed at the ANTARES linear accelerator at ANSTO. A He^{2+} microbeam of energy 5.5 MeV and diameter 1 μm was used to perform the study. The beam was raster-scanned in x-y across the test structures, covering a total area of 1 $\times$ 1 mm^2 with a resolution of 2 μm. The bias across the pixels was varied from 0V to -40V in increments of 10 V. For each test structure, four pixels were investigated and the response of two of the pixels – one square pixel and one strip – is presented. The response of each pixel and its amplification channel was calibrated against a Hamamatsu PIN diode which acted as the reference detector for evaluation of the full charge collection efficiency. The IBICC procedure is the same as used by Tran et al. (2015).

5.2.9 Spatial Resolution

The spatial resolution of detectors MP512 and DUO was evaluated against radiochromic film. The detectors were irradiated by a 6 MV linac beam of size 3 $\times$ 3 cm^2, at depth 1.5 cm d_{max}, dose rate of 600 MU/min and 10 cm SolidWater backscatter. The film was scanned using a Microtek ScanMaker i800 48-bit flatbed scanner in transmission mode. Six scans were performed prior to irradiat-

ing the film, with the first three being discarded to account for scanner warm-up. The last three scans were split into their RGB components and the red component was averaged across 2 $\times$ 2 pixels to obtain the average optical density of a 0.5 $\times$ 0.5 mm^2 equivalent area. The profiles were then normalised to the center of the interumbra and compared. The FWHM and penumbra studies were performed using a shape-preserving fitting tool in MATLAB by MathWorks (Natick, MA) to qualitatively assess the spatial resolution of the MP512 and DUO detectors.

5.2.10 Timing Study

An investigation of the ramp-up of four Varian iX Clinac machines at ICCC (Wollongong, Australia) and Peter MacCallum Cancer Centre (Melbourne, Australia) was performed using the MagicPlate-512 detector and Romulus software. The study was performed to observe the behavior of the linacs in the transient period of the dose ramp-up, to qualitatively assess if there would be any discrepancy between the planned dose and delivered dose when delivering small doses in the order of a few MU. The duration of the ramp-up was investigated as well by looking at the time it took the dose rate to reach equilibrium with respect to time. The MP512 detector was irradiated at 'standard conditions' in SolidWater and a pixel was chosen from the centre of the detector to plot the response versus time. The integration width was 52 µs and the duration of the beam-on time was 10 seconds, for a total dose of 100 MU. The same measurement was delivered using a gated treatment, where a pause of 750 ms was introduced in the beam-on time to effectively split the 100 MU dose in four parts, in order to simulate the delivery of short-MU dose. The impact of the start-up transient on the short-MU delivery was

discussed.

5.3 Results

5.3.1 Pre-Irradiation Characterisation

The I-V and C-V traces have been performed using the test structures for DUO and OCTA. The I-V trace in Fig. 5.4 shows that the majority of pixels from both detectors have a leakage current in the order of 10^{-9} A and undergo breakdown after 45 V. Fig. 5.5 shows the C-V trace of the DUO and OCTA test structures. The capacitance drops with a high rate at low applied bias and begins to reach a stabilisation after about 30 V.

5.3.2 Linearity

The detector arrays demonstrate a good linearity response as a function of dose, as shown in Fig. 5.6. The MP512 and DUO demonstrated linear responses with sensitivity 1.88 nC/cGy and 1.43 nC/cGy, respectively. Higher sensitivity of MP512 was expected due to the larger sensitive volume of the pixels.

5.3.3 Uniformity

MP512 has been fabricated using three different *p*-stop concentrations (boron doped implant under the field silicon oxide) identified by low, medium and high concentration. The *p*-stop implantation concentration plays a main role not only in

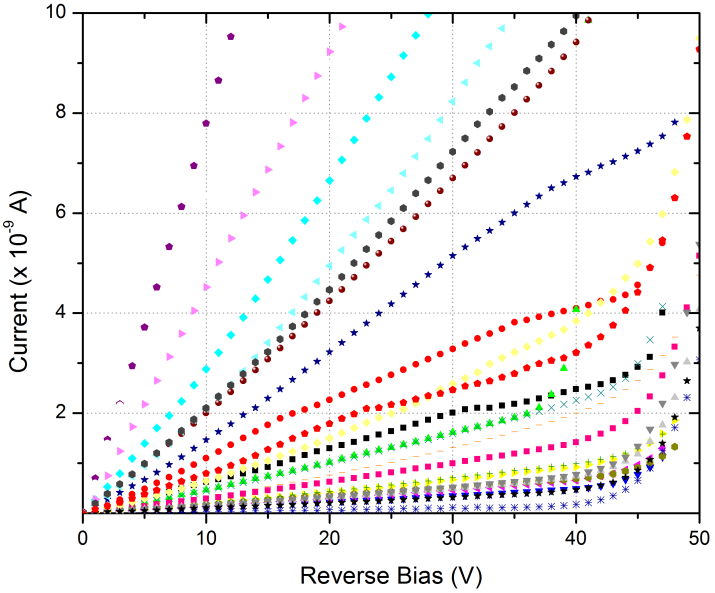

(a)

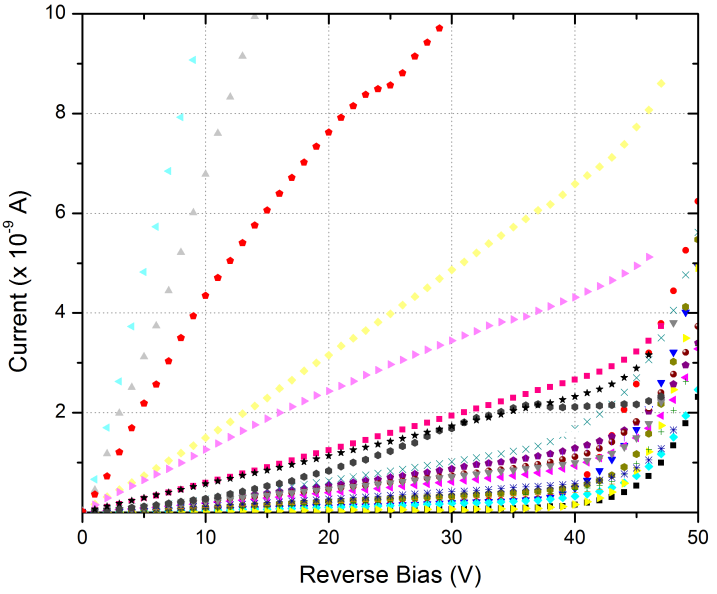

(b)

Figure 5.4: I-V traces for (a) DUO and (b) OCTA. Each curve represents the response of a pixel from the test structures.

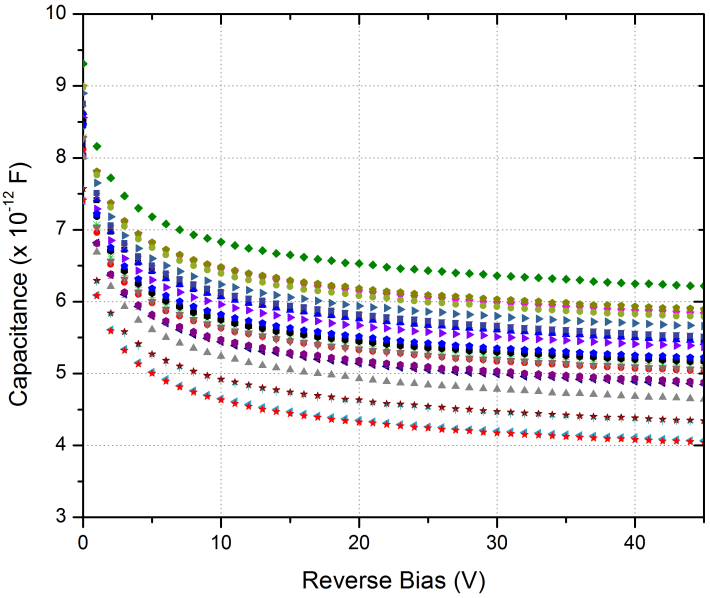

(a)

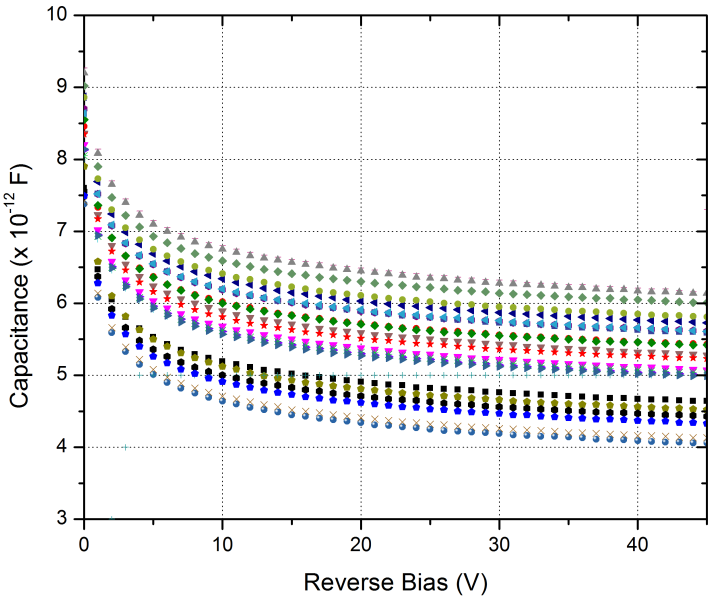

(b)

Figure 5.5: C-V traces for (a) DUO and (b) OCTA. Each curve represents the response of a pixel from the test structures.

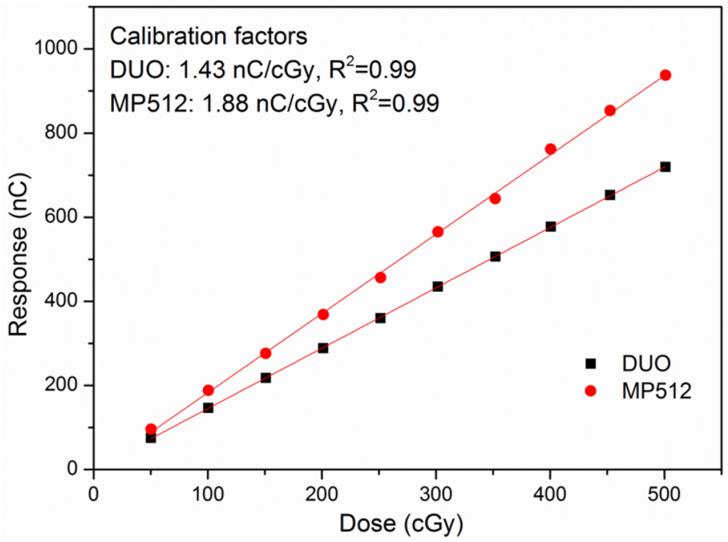

Figure 5.6: Linearity response of MP512 and DUO. A higher gradient is present in the MP512 data due to the larger sensitive volume of the pixels compared to DUO

the pixel isolation but also in compensating the superficial defects of the substrate, affecting the array response uniformity particularly when the device is operated in passive mode. When the detector is irradiated by a flat x-ray beam with size of 20×20 cm^2 within a water equivalent plastic phantom at depth of 10 cm, the sample fabricated with Low concentration (Fig. 5.7a) shows a pronounced non-uniform response across the pixels, in the shape of a ring. Fig. 5.7b shows, on the same color scale, that a higher p-stop concentration mitigates the non-uniformity. Fig. 5.8a shows the comparison of the profiles extracted from the flat response of three samples with different *p*-stop implantation concentration without any equalization.

The variation of the flat field response of the Low *p*-stop concentration samples is approximately 500% along the ring, and represents a discrepancy which cannot be compensated by an equalization procedure. The variation for the Medium and

High concentration samples is approximately 9% and can be compensated by the equalization procedure with a final uniformity of the detector response which is within 0.5% for 98% of the pixels as demonstrated in Fig. 5.8b.

The distribution of the defects across the wafer is normally distributed with cylindrical symmetry (Sze and Ng, 2007). Impurities in the substrate in the form of thermal donors may increase the effective doping concentration locally and consequently increase the weak electric field, present in passive mode due to the built-in potential, in proximity of the pixel junction, thus increasing the depletion region and the amount of charge collected by the pixels. A low concentration *p*-stop implant is not able to compensate for such substrate defects which generate the rings on the detector response map when it is irradiated by a uniform photon beam.

Fig. 5.9 shows that also DUO, when manufactured with High concentration *p*-stop has a good response's uniformity with 95% of DUOs pixels within 1% of the mean, while over 68% deviate within approximately 0.5%. The detector thus shows very good uniformity across its pixel response.

5.3.4 Radiation Damage

In order to obtain a stable response independent of the amount of accumulated dose (Rikner and Grusell, 1987), a pre-irradiation is carried out of DUO and MP512 detectors (samples with High *p*-stop). Detectors' sensitivity and response, as a function of delivered dose, is shown in Fig. 5.10. DUO stabilises its response within ±1.5% after irradiation with 80 kGy (dose in water) and above, by a Co-60 gamma photon source, although it is evident that the variation becomes even less

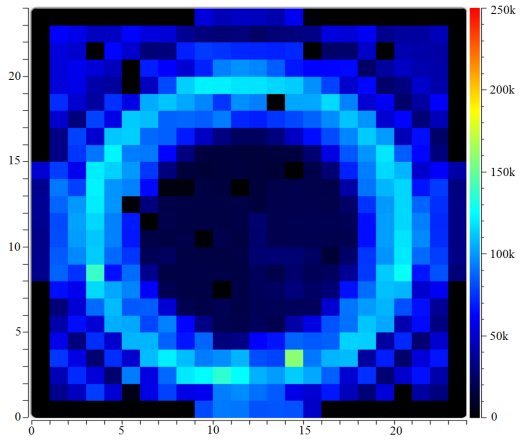

(a)

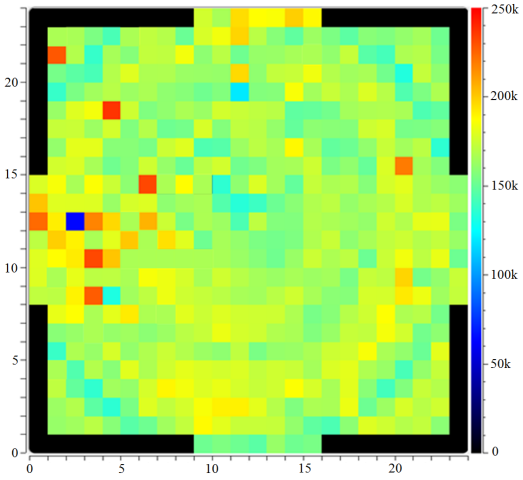

(b)

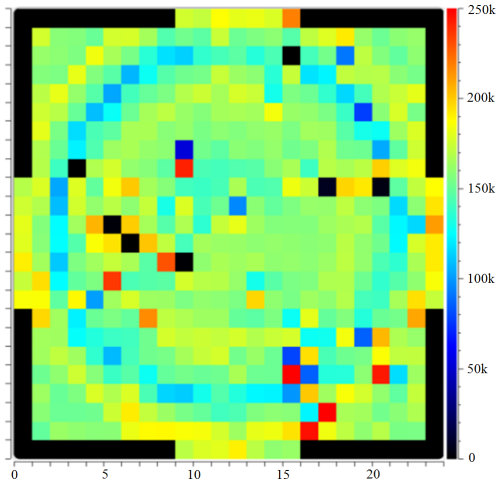

(c)

Figure 5.7: MP512 pixel response map of the samples fabricated with (a) Low p-stop concentration, (b) Medium concentration, and (c) High concentration. Colour scale is normalised to the same value in all maps.

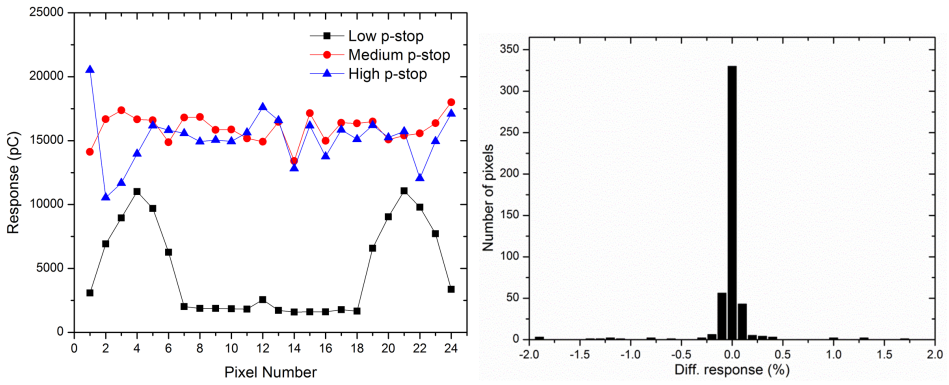

(a) (b)

Figure 5.8: (a) MP512 vertical profile of the response to a flat field. The artifacts are clearly visible on samples with Low *p*-stop concentration, but less pronounced when Medium and High *p*-stop is adopted; (b) Statistical distribution of pixel response for MP512 manufactured on Cz wafer with High *p*-stop and equalized

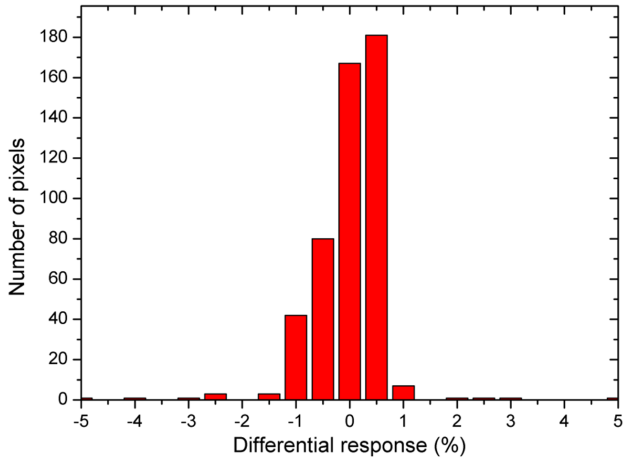

Figure 5.9: Statistical distribution of pixel response for DUO manufactured on Cz wafer with High *p*-stop after equalization

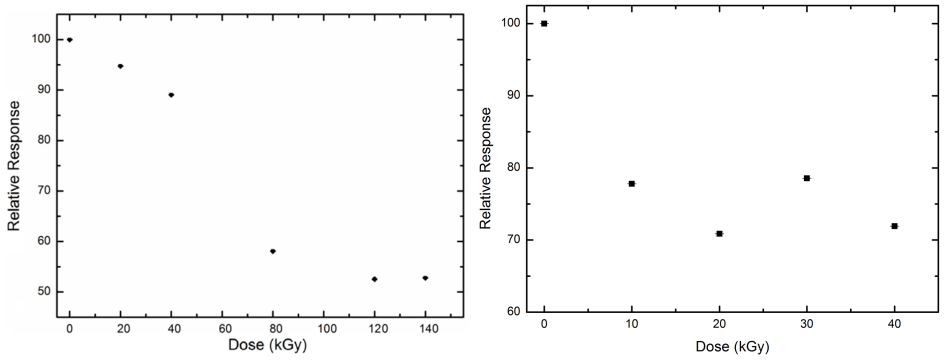

(a) (b)

Figure 5.10: Variation of the response of DUO (a) and MP512 (b) as a function of the accumulated dose by irradiation with a Co-60 gamma source

at doses over 100 kGy. The MP512 (High *p*-stop) shows stabilisation of response at doses as low as 20 kGy with a variation of approximately ±5%. Fig. 5.11 shows the expected linear increase of the leakage current density as a function of the accumulated dose (Kraner, 1984) for both DUO and MP512 after normalisation in respect to the detector volume.

Fig. 5.12 shows the relationship between detector response and equivalent neutron dose; it is clear that the response of the MP512 detector decreases with photoneutron dose with a rate which is approximately 1% per 33 Gy of 18 MV photon dose delivered. The direct implication of this result is that when subjected to photoneutron fields, the MP512 detector requires recalibration after about 65 Gy of delivered dose, due to the response of the detector nearing 2% variation as it is subjected to radiation damage.

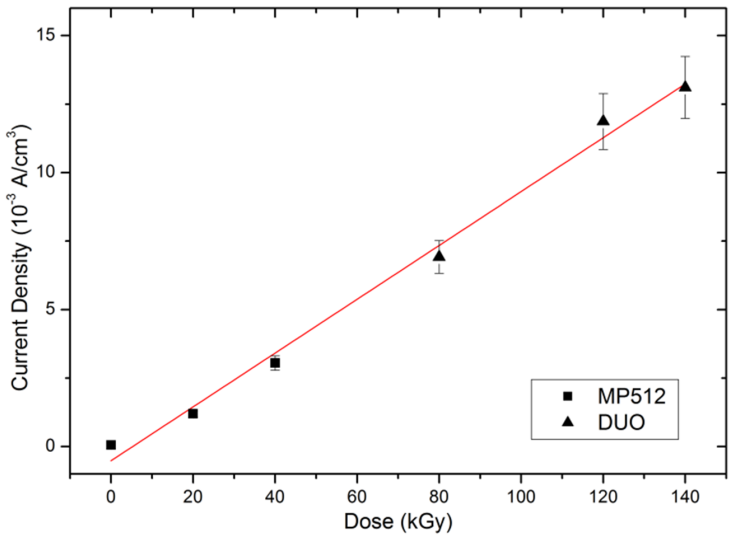

Figure 5.11: Variation of the leakage current as a function of the irradiation dose of MP512 and DUO (High *p*-stop) after normalisation to the detector volume. Error bars are calculated as one standard deviation from the mean value of the current measured in both the detectors for several pixels. The radiation damage factor alpha is calculated from the slope. Its value is $(9.83 \pm 0.4) \times 10^{-5} A \cdot cm^{-3} \cdot kGy^{-1}$ and it represents the variation per kGy of the leakage current density. The regression coefficient R^2 is 0.991. The value is comparable with values measured in literature (Moll, 2006)

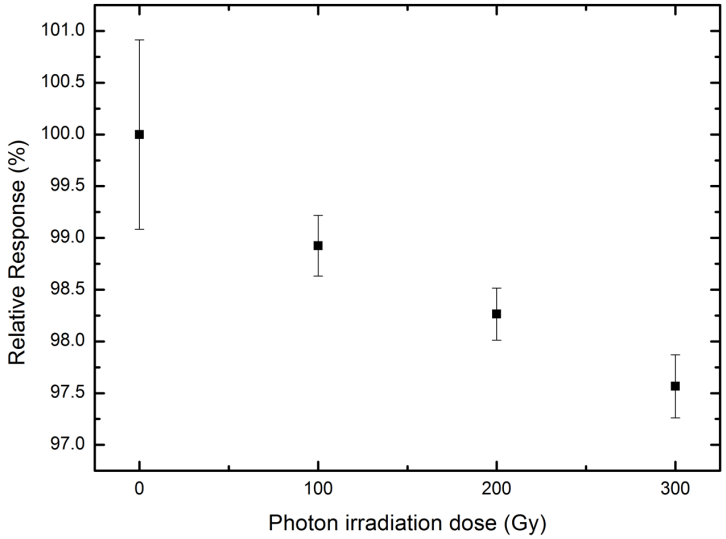

Figure 5.12: MagicPlate-512 detector response as a function of 18 MV photon irradiation dose

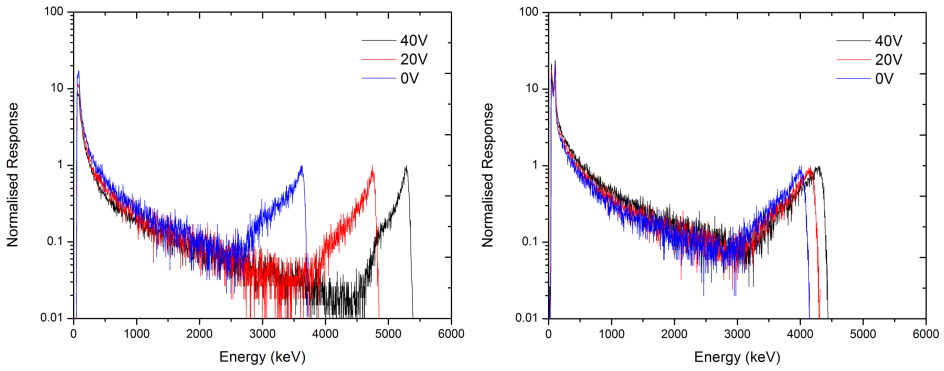

(a) (b)

Figure 5.13: Spectra of charge collection response for DUO pixel (a) and OCTA pixel (b) at negative bias voltages varying from 0 V to 40 V. The energy of incident alpha particles is 5.5 MeV

5.3.5 Charge Collection Efficiency and Charge Sharing

The charge collection efficiency and crosstalk of the inner part of the DUO and OCTA test structures has been also investigated by using a 5.5 MeV He2+ pencil beam. Alpha particles of this energy have a maximum range in silicon of approximately 28 µm (SRIM, 2015). Fig. 5.13 shows the energy spectra collected by DUO and OCTA central test structure pixels for 5.5 MeV alpha particles at five different operating reverse bias: 0 V (passive mode), 20 V and 40 V. Energy axis is calibrated by using a PIN diode HAMAMATSU (Japan). The spectra symbolise the histogram of the energies collected for the detectors central pixels, with the low energy tail of the graph being attributed to the area around the pixel where only very low residual energy is collected by events occurring at a large distance from the junction.

For the DUO test structure response, approximately full CCE (96%) is obtained with the reverse bias of 40V, while for passive mode 66% of the signal is collected,

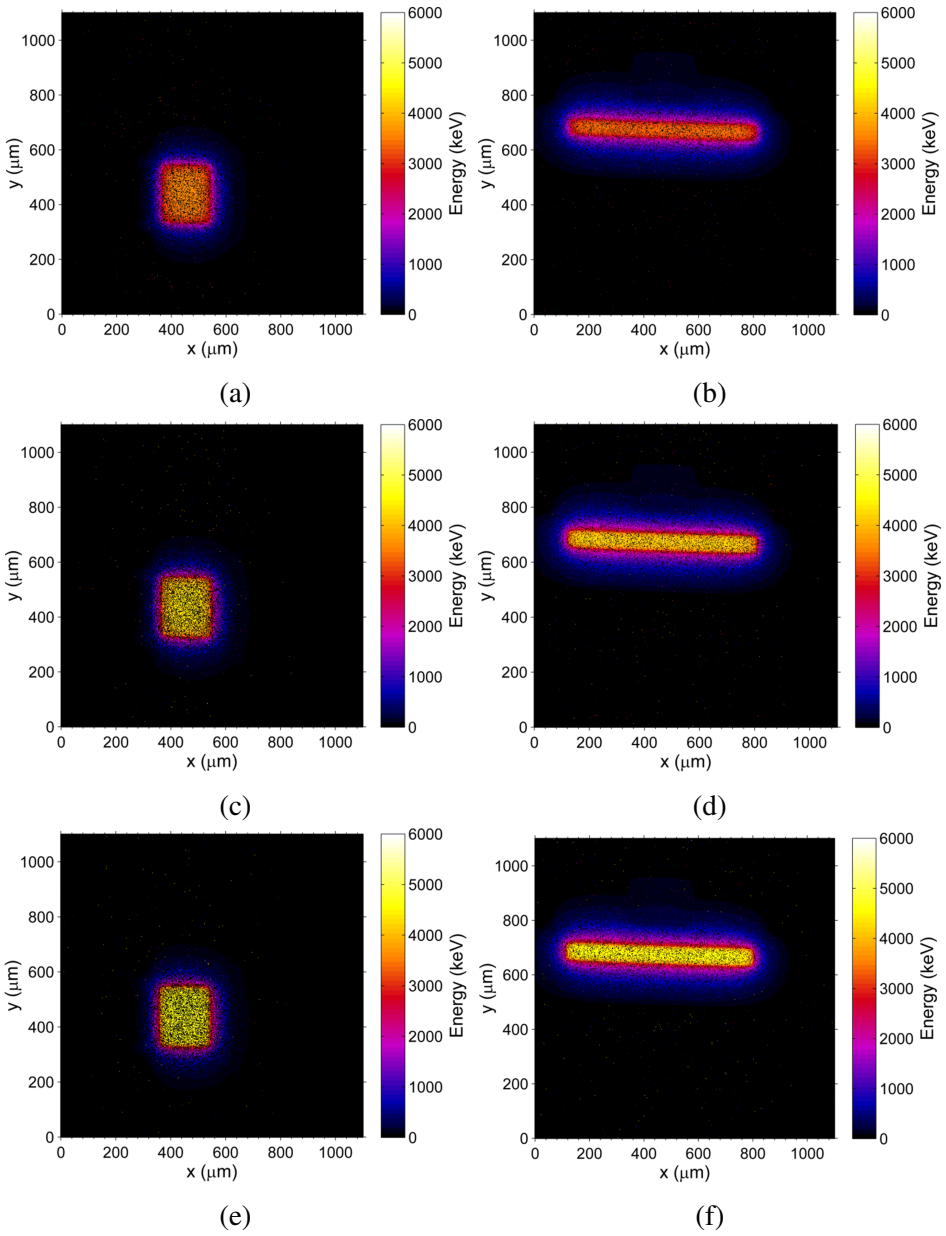
y (μm)
x (μm)
Energy (keV)
0
200
400
600
800
1000
1000
2000
3000
4000
5000
6000
(a)
(b)
(c)
(d)
(e)
(f)

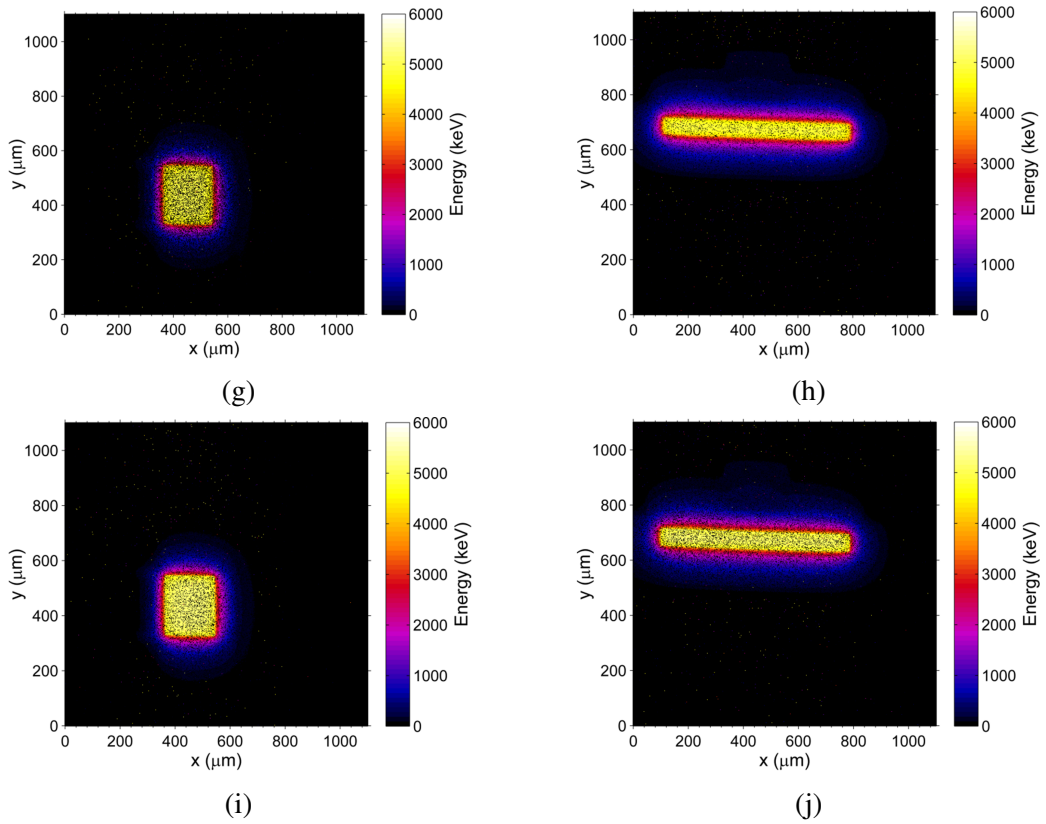

Figure 5.14: 2D map of charge collection for DUO pixels for applied bias of 0 V (a,b), 10 V (c, d), 20 V (e, f), 30 V (g, h), and 40 V (i, j).

corresponding to a range in silicon of approximately 16 µm (Ziegler, 2015). The result confirms that the size of the depletion region in the semiconductor varies with applied bias as expected by the theory; in the case of 40 V, the depletion region in the detector is within 5% of the range of 5.5 MeV alpha particles, meaning that nearly all the electron-hole pairs generated by the alpha ionisations are collected as signal and only 5% of the carriers recombine along their path toward the electrodes. In the case of 0 V bias, the depletion region reaches a depth of only few microns but the diffusion length combined with the depleted region reaches a value of approximately (15 ± 0.5) µm.

The OCTA spectra for the different voltages is much less spread out compared to DUO; the peaks from all three biases are within a range of only 300 keV, corresponding to a CCE of 73% in passive mode; 76% at 20 V bias; and 78% at 40 V. In comparison, the DUO energy range is 1800 keV for the three peaks. This is clear from both the median maps in Figs. 5.14 and 5.15 and from the spectra in Fig. 5.13, where OCTA is obviously suffering of larger recombination effects. The significance of this result is that OCTA has a higher CCE (and thus a higher SNR) in passive mode compared to DUO. The depletion region does not seem to vary in size much with applied bias compared to DUO. The reason for this is possibly due to two combined effects: first of all, the size of the junctions in OCTA is slightly larger than in DUO with a larger area per pixel, extending the depleted region in passive mode to a larger area, and secondly, crosstalk between OCTA's pixels is higher than in DUO, enhancing the charge collection efficiency.

Fig. 5.14 shows that the crosstalk between the pixels for DUO is minimal with no charge collected and recorded in adjacent pixels for the central pixel response, and

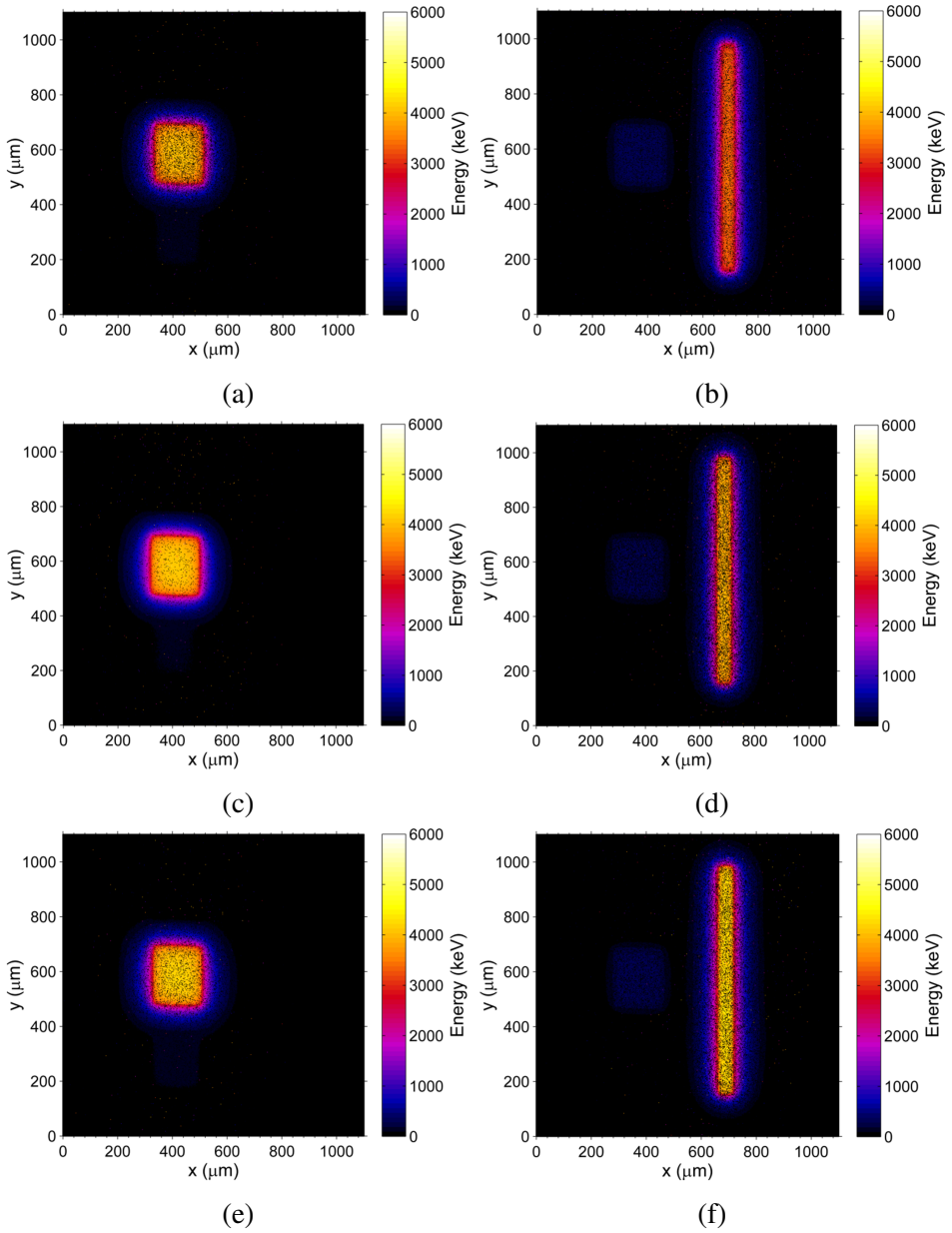
y (μm)
x (μm)
Energy (keV)
0
200
400
600
800
1000
1000
2000
3000
4000
5000
6000
(a)
(b)
(c)
(d)
(e)
(f)

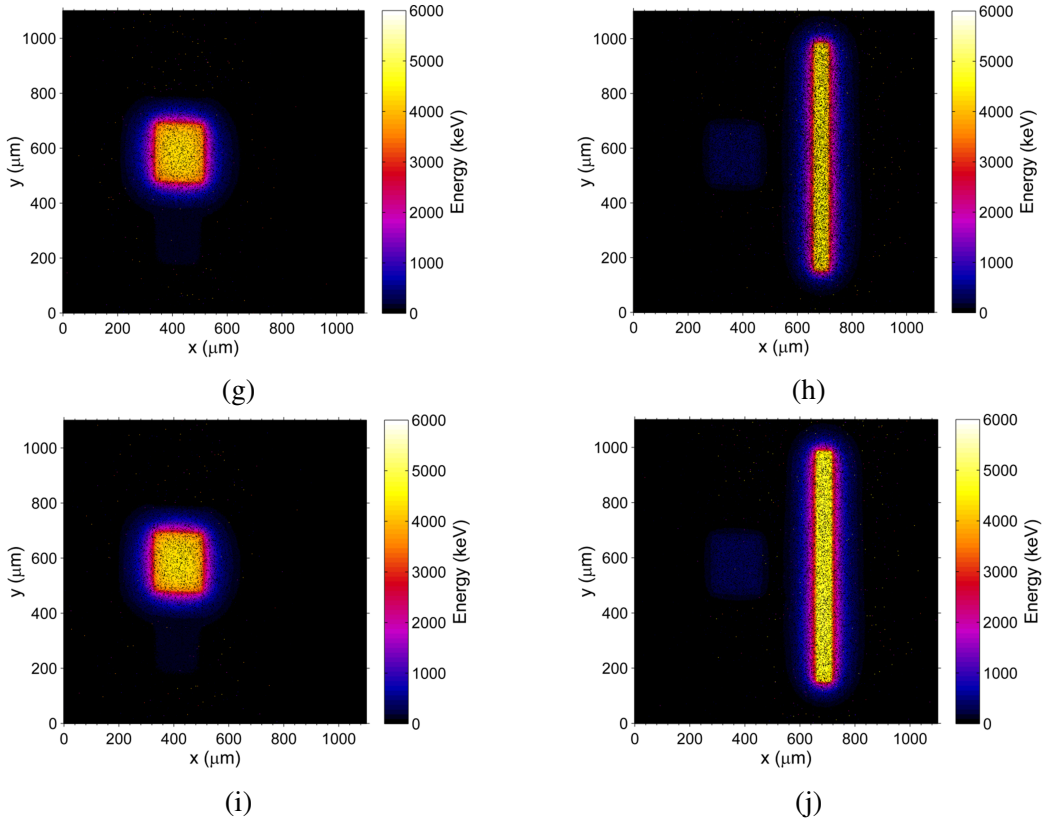

Figure 5.15: 2D map of charge collection for OCTA pixels for applied bias of 0 V (a,b), 10 V (c, d), 20 V (e, f), 30 V (g, h), and 40 V (i, j).

approximately less than 20% charge collected around the *n*+ junction. This confirms that the DUO detector's spatial resolution is not affected by charge sharing or crosstalk, even with the small pitch of 200 µm. Fig. 5.15 shows the OCTA test structure response. The central pixel of the OCTA test structure shows a good response with no crosstalk with adjacent pixels. There is a slight crosstalk between the strip pixel and the adjacent square pixel, about 10% of the charge collection occurring in the strip. However this could not lead to an over-response of the strip because it is related only to events with very low energy which are not counted in the charge collection efficiency. The crosstalk could instead lead to a reduction of the effective spatial resolution when subjected to steep dose gradient x-ray radiation fields.

5.3.6 Spatial Resolution

In a monolithic silicon pixelated detector, spatial resolution is not only defined by the pixel pitch and sensitive volume size, but can also be affected by the crosstalk of adjacent pixels, particularly when exposed to a continuous energy spectrum of photons such as the one generated by Bremsstrahlung in medical linacs. To investigate the DUO's and MP512's effective spatial resolution, we compared their response to that of radiochromic film, which is widely used for dosimetry profiling in hospitals and has the advantage to have a spatial resolution limited by the capabilities of the optical scanner used to read out the film.

Fig.5.16 shows the response of MP512 and DUO in comparison with EBT3 film for the 2×2 cm^2, 1×1 cm^2 and 0.5×0.5 cm^2 fields with a variation of the

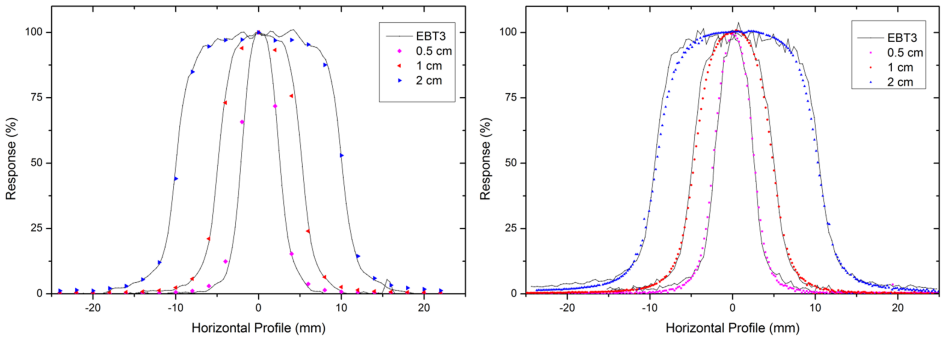

(a) (b)

Figure 5.16: Profiles reconstructed by MP512 (a), and DUO (b) in comparison with EBT3 film for three stereotactic field sizes

FWHM of the dose profile of less than 0.35 mm for DUO and 0.6 mm for MP512, while the discrepancy for the measurement of the penumbra width (20%-80%) is up to 0.58 mm and 0.57 mm for DUO and MP512, respectively. The results, expressed in mm, are tabulated in Table 5.1. The irregularity in the film profile is due to irregularities of the surface of the film which leads to a perceived change in the optical density.

5.3.7 Timing Study

The timing study has been investigated for four identical Varian Clinac machines at ICCC, Wollongong, and Peter MacCallum Cancer Centre, Melbourne. The ramp-up of the linacs LA1 and LA2 is shown in Fig. 5.17. The linacs are identical models from the same vendor, however the ramp-up transient is different due to the calibration of the machine. The transient of LA2 (Fig. 5.17b) shows a negative gradient for a few milliseconds in the build-up curve before the dose per pulse continues to increase. An oscillation in the dose rate is further present up

Table 5.1: Comparison of FWHM and penumbra width (20%-80%)

	FWHM (mm)			Penumbra (20%-80%) (mm)			Difference FWHM (mm)			Difference Penumbra (mm)		
FS (cm)	0.5	1	2	0.5	1	2	0.5	1	2	0.5	1	2
EBT3	4.73	10.16	20.04	1.85	2.1	2.46						
MP512	5.32	9.88	19.86	2.13	2.67	2.91	-0.6	0.28	0.18	-0.29	-0.57	-0.45
DUO	4.85	9.9	19.87	1.98	2.85	3.38	-0.19	0.35	0.35	-0.37	-0.26	-0.58

The comparison is for MP512 and DUO detectors with respect to EBT3 film. Statistical uncertainties for the FWHM are less than 2% for DUO and 3.6% for MP512. The uncertainties in the data points are calculated as two standard deviations of the mean of five repetitions. The average uncertainty in film measurements is 1.9% and the procedure for obtaining the film uncertainty is outlined in (Aldosari et al., 2014).

to three seconds from beam-on time, with a period of about 1 second. The overall statistical variation between the individual dose transient maxima and minima is about ±10% of the dynamic range. LA1 shown in Fig. 5.17a has a build-up which presents no special behaviour of the dose rate. LA1 from Peter Mac has an elevated dose rate for the first 750 ms of beam-on time, before it stabilises for the remainder of the measurement. LA2 (Fig. 5.17d) has an interesting oscillation of the instantaneous dose rate for the first three seconds of beam-on time before also stabilising within ±2% of the dynamic range.

Despite these different transient characteristics, the overall total delivered dose of 100 MU is within ±0.5% for the four linacs, which means that despite the different beam quality of the linacs, the dose delivered is as expected, at least for relatively long beam-on irradiations where the total duration of beam on is much higher than the ramp-up of the dose rate.

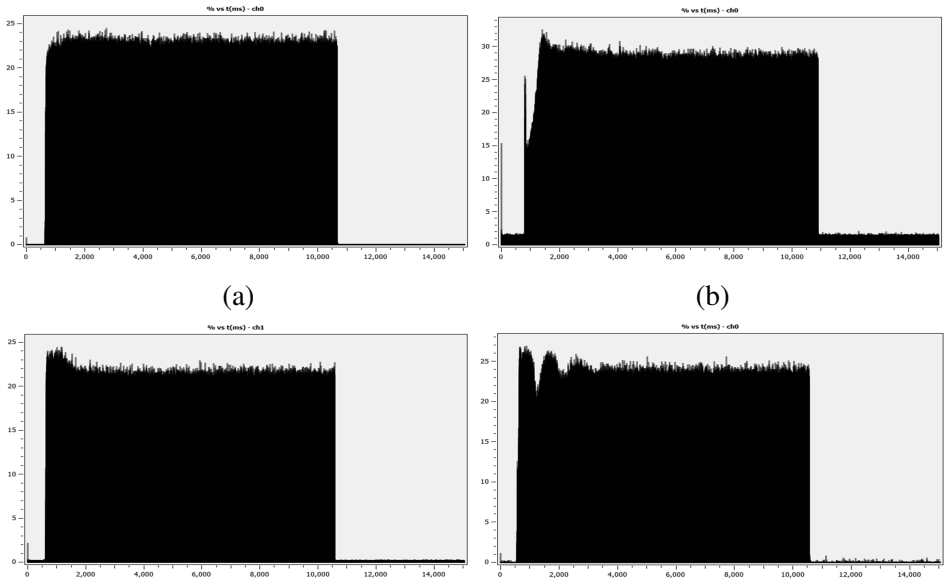

(a) (b)

(c) (d)

Figure 5.17: Response of identical Varian Clinac iX accelerators at Illawarra Cancer Care Centre, Wollongong (a), (b); and Peter MacCallum Cancer Centre, Melbourne (c), (d), delivering 100 MU of dose. The ramp-up transient is clearly different for each linac

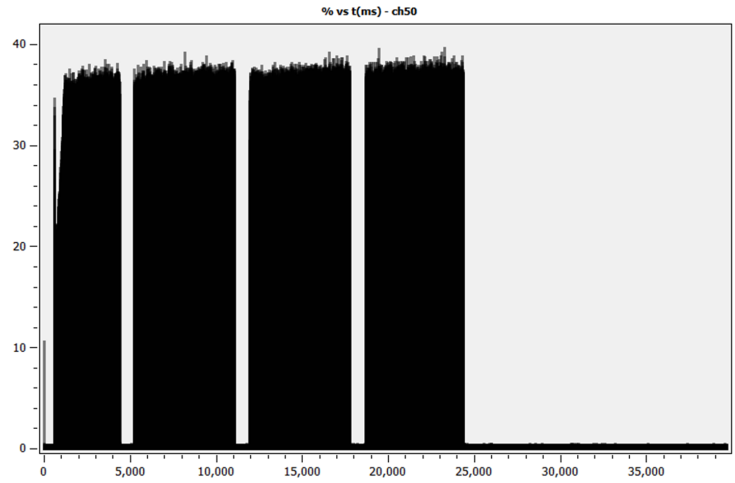

Figure 5.18: Response of ICCC Varian linac when using gating

However in the case of short-MU due to the gating, it is clear that the first beam-on segment is affected by the stabilisation issue of the current flowing through the electron gun, but the subsequent segments do not suffer of the same issue and the dose delivered is properly shaped as a function of time, reducing the impact of the dose fluctuation (Fig. 5.18). This feature may have a potential impact of dose delivery by linac for short MU treatments.

5.4 Conclusion

In this chapter, the characterisation of detectors MagicPlate-512, DUO and OCTA has been performed using a clinical linac for the arrays and a He^{2+} microbeam and electrometers for the test structures. The DUO detector presents excellent dose linearity and small statistical variation of pixel response. The pre-irradiation dose required for the stabilization of the response is 120 kGy. DUO spatial resolution and crosstalk has been evaluated by the measurement of a 6 MV photon beam of 3

$\times$ 3 cm^2 field size and compared to EBT3 film. It has been found that FWHM of the reconstructed profile is within 0.6 mm and the penumbra (20%-80%) is within 0.1 mm. Crosstalk between the DUO's pixels is minimal and charge collection efficiency for 5.5 MeV He^{2+} ions is over 60% even when no bias is applied. The leakage current when under reverse bias is in the order of 10^{-9} A and capacitance is in the order of 10^{-12} F. The MP512 detector also showed excellent linearity and stabilisation of response after pre-irradiation with total dose of 20 kGy. Beam profile reconstruction comparison with EBT3 film shows a discrepancy in FWHM within 1.1 mm and 20%-80% penumbra within 0.3 mm due to a larger detector pitch. Three different boron implantation doses have been also evaluated to optimise the response of the detector in terms of uniformity and isolation between the pixels. A low *p*-stop concentration generates a ring artifact with a radius of ~17 mm around the center of the detector due to the silicon wafer manufacturing and residual impurities in the monolithic substrate affecting the rate of recombination of generated electron-hole pairs. This effect can be mitigated by using the largest dose of boron implantation. Stability with radiation damage has been also evaluated in a photoneutron field by irradiation by an 18 MV medical linac, where the MP512 detector shows a pronounced decrease of the response as a function of the total irradiation dose. The device requires a recalibration every 65 Gy delivered dose when using beam energies of 10 MV and higher, to account for decrease in response due to cluster defects in the silicon lattice caused by non-thermalised photo-neutrons (commercial p-Si diodes have similar degradation sensitivity at 18 MV). The OCTA detector has a charge collection efficiency of 72% when in passive mode, ranging very little to 78% at 40 V reverse bias. The central pixel does not show any crosstalk, while the strip pixel shows a crosstalk of about 10% with

one of the adjacent square pixels.

Chapter 6

Application of The Magicplate-512 System to Characterise a Co-60 Theratron Radiation Source for Small Animal Treatment

This chapter has been published in Journal of Instrumentation:
C. S. Porumb, J. B. Davies, V. Perevertaylo, A. B. Rosenfeld, M. Petasecca, 2016, *Characterisation of a cobalt-60 small-beam animal irradiator using a realtime silicon pixelated detector*, Journal of Instrumentation, vol. 11, P04014, doi:10.1088/1748-0221/11/04/P04014

6.1 Introduction

Animal treatments involving external beam radiotherapy are performed to maximize the life expectancy for animals with tumors. Further, the treatment of artificially-induced tumors in small animals such as mice or rats may help develop our understanding of the behavior of certain cancers in humans, and how to control them more efficiently. Often, irradiation of small animals is performed using low dose rate irradiators which are less expensive than medical linacs and their very low dose rate can be tolerated because animals are typically immobilised and they can be irradiated for longer time than humans.

In this chapter, the characterisation of an irradiator THERATRON cobalt-60 located at ANSTO (Lucas Heights, Australia) and adopted for cell and small animal low dose rate irradiation with three pencil beams is presented. The irradiator is equipped with three lead collimators to shape the gamma-ray beam to circles of approximately 5, 10 and 20 mm in diameter. The irradiator is also provided with a fast mechanical shutter. The pencil beams are intended for the irradiation of the head of an animal (mouse or rat) whilst collimator is shielding the remaining of its body, with the intention to study the effect of ionising radiation on nervous system function. Due to the size of the target volume, it is important to estimate the shape of the delivered dose accurately and identify the irregularities in the profiles, if any. There was a need to substantially improve the characterisation of the radiation fields previously performed with an ionisation chamber, as the volume averaging effect of the ionisation chamber sensitive volume prevented the accurate determination of high dose gradient profiles realised by the means of the small radius collimators. Use of radiochromic film is recommendable for their

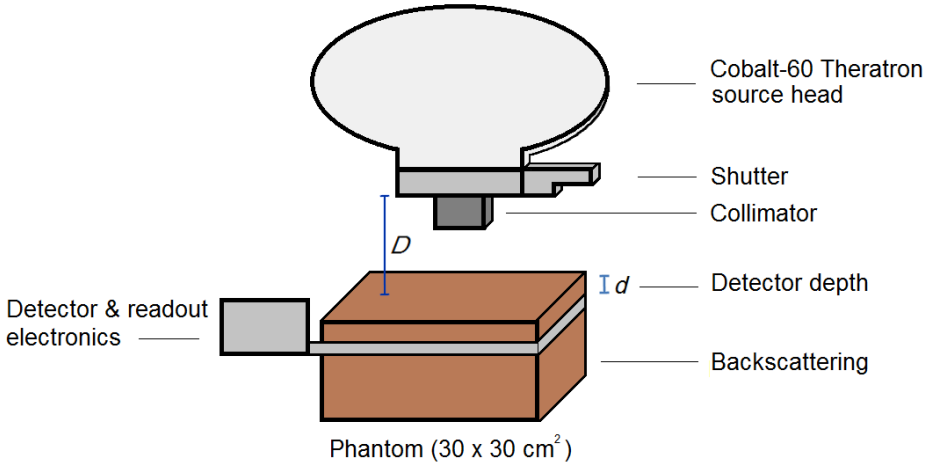

Figure 6.1: Schematic diagram of experimental setup. The source-to-axis (SAD) distance is labeled as *D*

intrinsic spatial resolution for the profiles but cannot characterise the performance of the mechanical beam shutter and the percentage of dose delivered during the beam-on/beam-off transient.

The percentage depth dose, beam output factors, and beam profiles are presented, as well as the timing study for the source's shutter using a real-time semiconductor detector array.

6.2 Materials and Methods

In this study, the MagicPlate-512 detector system developed by CMRP was used for the real-time acquisition, alongside a calibrated Farmer ionisation chamber and EBT3 radiochromic film, to characterise a Theratron, 6 TBq, Co-60 gamma irradiator equipped with three collimators of diameter approximately 5, 10 and 20 mm.

6.2.1 Readout System

The AFE-based readout system in conjunction with Romulus Radiation Tools was used to record the measurements of the detector response. The full description can be found in Section 3.1.7. For this study, an accompanying software named 3DdataView was written to display the beam profiles in 3D to allow for a better understanding of beam irregularities or asymmetry encountered.

6.2.2 Ionisation Chamber and Film Dosimetry

The ionisation chamber that was used in this study is a thimble type PTW Farmer ion chamber (Freiburg, Germany) of volume 0.6 cm^3 and energy detection range of 30 kV to 50 MV. The chamber has an accompanying Solid Water phantom block of $30 \times 30 \times 2$ cm^3 with a specifically machined cavity for the chamber's sensitive volume to be inserted in the center of the phantom, which eliminates any air gap between the Solid Water and the detector. The ionisation chamber was used as the benchmark reference detector for the percentage depth dose measurements.

The high-resolution mapping of the profiles was achieved with Ashland Gafchromic EBT3 film (Wayne, NJ). The film is self-developing, it is nearly tissue equivalent, it presents no orientation dependence and it has high spatial resolution. The film needs at least 24 hours developing time to ensure a stable polymerisation has occurred. The change in optical density (absorbance) of the film with respect to dose is not a linear relationship; thus it is necessary to obtain a calibration curve in order to correctly reconstruct the measured dose as read by the film. The film was scanned with a Microtek ScanMaker i800 48-bit flatbed scanner, in transmission

mode.

Prior to any measurements, the dose rate of the gamma source was calculated using the ionisation chamber. The calculation accounted for temperature and pressure in the room and its purpose was to determine the length of irradiation to obtain a suitable signal-to-noise ratio for all the detectors, in other words, to place the dose delivered to the films in the center of the optical density calibration curve. The measurement of the ionisation chamber was converted from exposure (X) to dose rate (D_w) in cGy/min using the equation

$$D_W = \frac{x \times k_{TP} \times k_{DK} \times N_W}{t} \times 60, \tag{6.1}$$

where k_{TP} is the temperature and pressure correction factor, k_{DK} is the decay compensation factor, N_W is the conversion factor from Roentgen to Gray (0.967 cGy/R), and *t* is the duration of the acquisition in seconds.

A SolidWater backscatter of 6.5 cm was used; 24 cm source-to-axis distance (SAD), as depicted by the length D in Fig. 6.1. The detector depth was 15 mm. Irradiation of the MP512 detector was performed under the same conditions prior to conducting this study, to determine the optimum acquisition parameters including duration of measurement, width of integration window and measurement frequency.

The MP512 consists of 512 pixels and the response of each pixel is different from its adjacent neighbors due to local substrate defects and parasitic capacitance associated with the connections' routing. The equalisation procedure described in Section 3.2.7 has been applied to the data. The equalisation factors were applied

to all of the MP512 detector datasets. The calibration factor of the MP512 was calculated using the highlighted central pixels of interest in Fig. 6.2a.

The calibration curve for EBT3 film was obtained using eight square samples of 3×3 cm^2. Each sample was irradiated with a different dose, as determined using the ionisation chamber, ranging from 50 cGy to 500 cGy in increments of 50 cGy, except for samples 7 and 8 where increments of 100 cGy we used. All squares were cut from one sheet of film to ensure sample uniformity due to identical batch used; they were numbered in the corner using black pen, arranged in order of increasing number and placed in a clear template receptacle, to fix position of each sample and eliminate any scanner-induced irregularities. The films were pre-scanned six times using the Microtek scanner, to ensure proper scanner warm-up and only the last three scans were used for analysis. The parameters of the scan were 48-bit RGB color transmission mode, 72 dpi (0.35278 mm/px), no applied filters. The last three scans were split in their RGB channels using ImageJ (v.1.4.3.67) and only the red component of the scanned images was used. The scans were averaged and a region of interest within each film was used to obtain the optical density prior to irradiation. The same process was applied to the larger profile film sheets. Once the samples underwent irradiation, they were allowed to develop for 48 hours, after which the scanning procedure was repeated, again discarding the first three images to allow for scanner warm-up. The OD was then plotted against dose and a 3rd order polynomial fitting curve was obtained.

6.2.3 Percentage Depth Dose

The PDD measurements were obtained using the IC and MP512 detectors. The SAD was set to be 24 cm (Fig. 6.1). This distance was arbitrarily chosen to be the typical distance where the animals will be placed for treatment, and was kept constant throughout the measurements. The IC was placed in the 2 cm thick Solid Water insert; 6.5 cm of backscatter was used. The measurements were performed at depth varying in increments of 5 and 10 mm, from 10 mm up to 50 mm with the shortest possible pauses between measurements, to minimise the detectors' temperature dependence and the IC's atmospheric pressure dependence. The measurements were taken using an open field without any collimators in the beam, to maximise lateral electronic equilibrium; equivalent field size when using no collimators is 10×10 cm^2. Duration of IC measurements was 100 seconds each. MP512 parameters were chosen to maximise the response of the detector due to the low dose rate of the source. The beam-on duration of the MP512 measurements was 20 seconds, with a 2000 µs integration window, 200 Hz repetition rate. Two datasets were acquired using dynamic range 0.5 and 1.2 pC per frame. The depth dose was sampled at each point twice with the IC and three times with the MP512, to establish a statistical fluctuation uncertainty.

6.2.4 Beam Output Factors

The output factor of a photon beam (OF) is a parameter that "increases with an increase in collimator opening or field size" (Podgorsak, 2005). Especially in small beams where lateral electronic equilibrium is not fully established, it is important

to determine the output factor of the beams to quantify the dose ratio between the open beam dose and the collimated beams. The output factors of the beams were obtained using EBT3 film and MP512. A region of interest in the center of each beam was used to determine the average dose. Areas of 5×5 mm^2, 4×4 mm^2, and 2.5×2.5 mm^2 were chosen as regions of interest in the film dose maps for the 20 mm, 10 mm and 5 mm beams respectively. In the case of MP512, four central pixels were used for the two larger beams, while two pixels were used in the case of the 5 mm beam. The response of the pixels was averaged, then normalised to the 10x10 cm^2 open beam and plotted. Film factors were corrected for the varying beam-on time using a normalising time coefficient, to compare the dose for the same beam-on time.

6.2.5 Beam Profiles

The measurement of the beam profiles was performed using the MP512 detector and radiochromic film for each collimator, at depth 1.5 cm and SAD 24 cm. The MP512 parameters were a 40 second beam-on time, 200 Hz repetition rate, 2000 µs window and 0.5 pC dynamic range per pixel. Three measurements were performed for each profile and averaged. A 2D map of the beams was produced and horizontal & vertical profiles were generated from the center of each beam.

Film measurements were performed using 6×6 cm^2 film samples. A pre-scan and was performed prior to receiving dose for each film sample, as described in Section 6.2.5. Depth, SAD and backscatter were unchanged from MP512 measurements. Based on the output factors, each film sample was irradiated for a

period of time corresponding to a 200-300 cGy dose, in order to obtain good SNR and to ensure a relatively central placement on the OD calibration curve. Samples were then left to develop and scanned after 48 hours. Horizontal and vertical profiles were extracted from the center of the maps and compared with the MP512 profiles using MATLAB curve fitting tool (shape-preserving). Penumbra study (20%-80%) and FWHM study was also performed using the profiles and compared for the two dosimeters.

The time it takes for the shutter to fully open (ramp-up) and close (ramp-down) has been investigated to evaluate the effect of the transient on the total dose delivered. The SAD was 24 cm, depth of detector 1.5 cm, and 10 $\times$ 10 cm^2 equivalent field (no collimator) was used. Fig. 6.2 shows the schematic diagram of the normalized response of pixels as a function of time. A raising edge is defined as the time interval between 5% and 95% of the normalised transient, depicted as Δt_1. A falling edge is defined as the interval between 95% and 5% of the response, depicted as Δt_2. Knowing the average dose rate from the cobalt-60 source, the delivered dose during the transients can be calculated; in this study, the doses associated with the raising edge and falling edge are defined as D_{t1} and D_{t2}, respectively. The seven pixels from each edge and four pixels from the center (Fig. 6.2a) were chosen to analyse the timing of the shutter. Beam-on duration was set to 20 seconds.

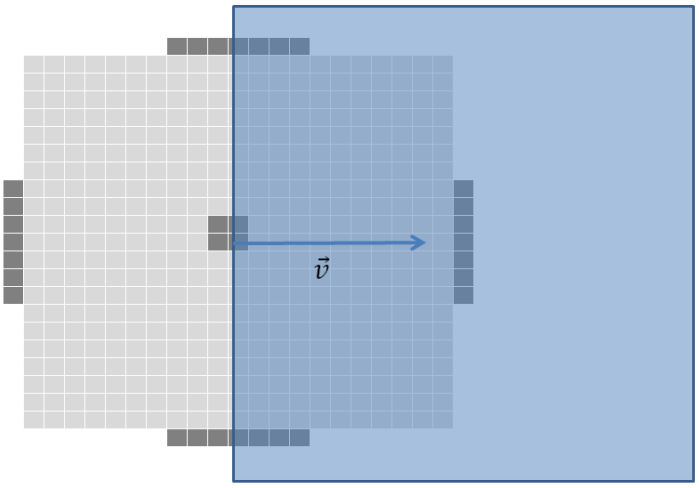

(a)

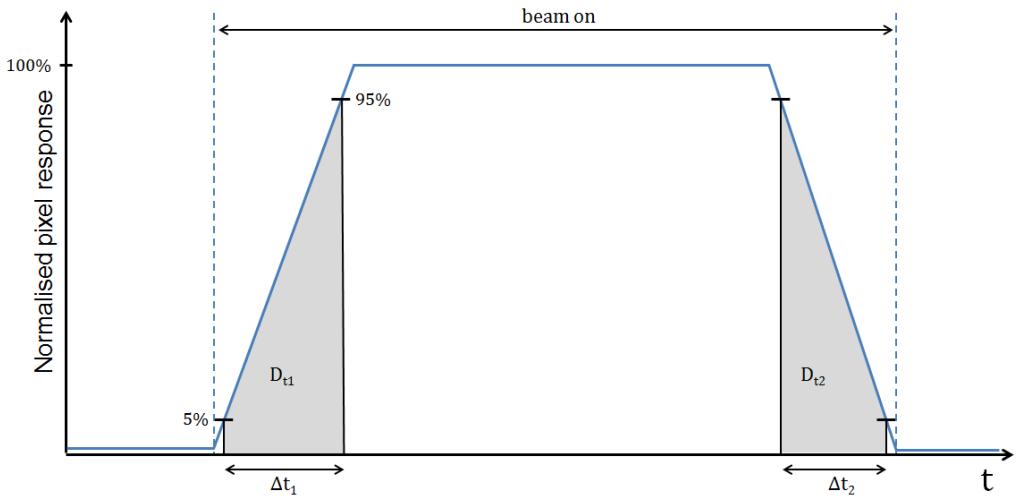

(b)

Figure 6.2: (a) Diagram showing, in beams eye view (BEV), the pixels of the MP512 (in dark grey) used for the timing study, and the shutter (blue) sweeping across the detector in the open sequence; (b) Diagram outlying the ramp-up and ramp-down transients in the response of the pixels, as a function of time

6.3 Results and Discussion

The radiation source of the Co-60 irradiator emits gamma rays continuously with an average dose rate which was determined to be (10.65 ± 0.03) cGy/min at 1.5 cm depth in Solid Water, using the ionisation chamber. Compared to the instantaneous dose rate of a clinical linac that ranges from 0.5 to 6 Gy/min at the same depth, it is clear that the dose rate of the Theratron source is very low. While the usual application of the MP512 detector and readout system is optimized for use in clinical linac quality assurance, in order to maximise the SNR in this specific application, MP512 has been set with the third highest sensitivity available (0.5 pC full dynamic range) and the longest integration time available (2 ms) assessing the uncertainty associated with MP512 measurements within a maximum of ±3% (two standard deviations) for repeated measurements. The calibration factor of the MP512 was calculated to be 242.5 ± 0.03 pC/cGy.

6.3.1 Percentage Depth Dose

The comparison between IC and MP512 percentage depth dose response is shown in Fig. 6.3. Ion chamber measurements had negligible statistical fluctuation between the two measurements for each depth, with the remaining uncertainty being only the limitation of the electrometer's smallest increment of 0.2%. In contrast, the MP512 experienced a statistical fluctuation of 1% on average in the response of the repetition of the measurements for each depth, with the extremes ranging from 0.36% to 2.4% difference between repeated measurements. This discrepancy is due to the fact that the DAQ system was operating in high stress conditions to

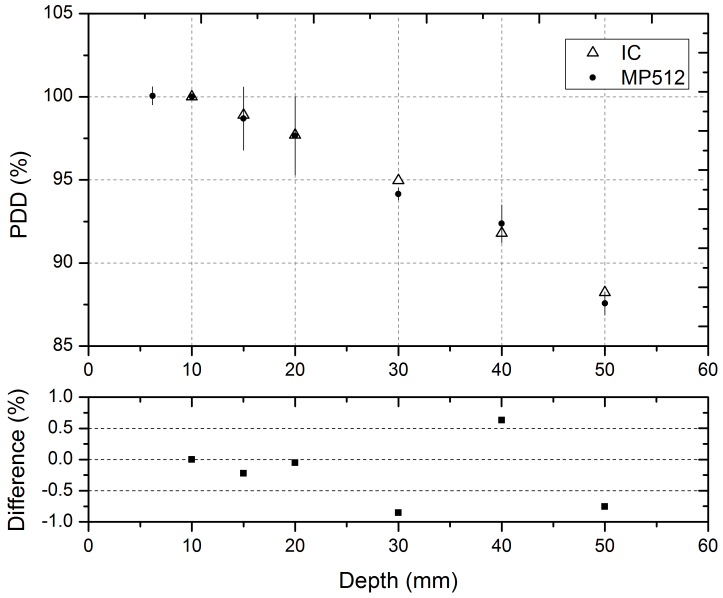

Figure 6.3: Percentage depth dose response for ionization chamber and MagicPlate-512 detector. The percentage difference is shown between the two dosimeters.

maximise the SNR due to the low activity of the source, as mentioned in Section 6.3. Typical operation parameters for the system in a MV linac measurement range from 50-100 µs integration window, 360-400 Hz repetition rate, and 9.6 pC maximum dynamic range. In this study, the window was set to 2000 µs, the repetition to 200 Hz, and maximum dynamic range was set to 0.5 and 1.2 pC. The extremely low dynamic range makes the fluctuation of the signal collected from the detector through the connecting cables very significant and the DAQ becomes very sensitive to radiofrequency fluctuation and external noise sources such as microphonic interference and light. To minimise these effects, a special care have been taken for designing a proper RF shielding of the cables and a dark plastic envelope to keep the detector light-tight without compromising the dosimetric measurements. Under these conditions, the response of MP512, after normaliza-

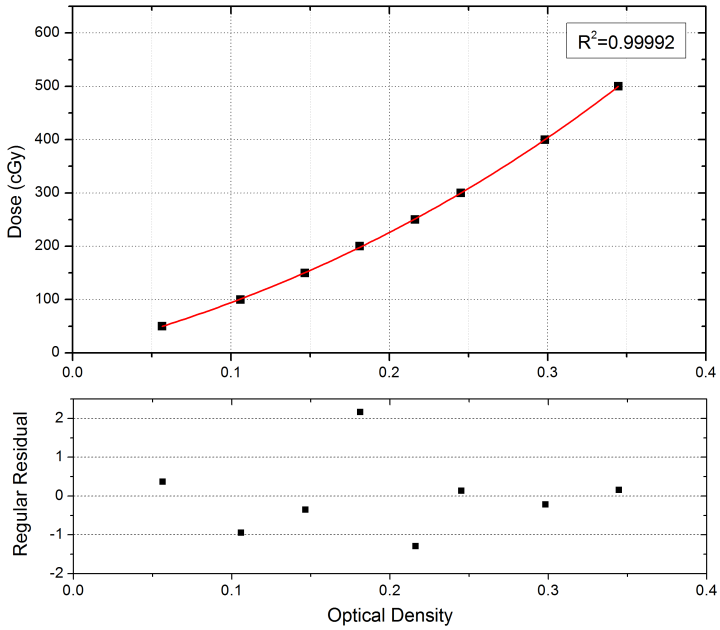

Figure 6.4: Calibration curve for EBT3 film. The equation of the polynomial fit is $D = 1273x^3 + 1548x^2 + 761.6x + 1.415$; $R^2 = 0.9999$

tion at d_{max}, agrees with the ionisation chamber measurements within one standard deviation.

6.3.2 Beam Profiles

The approximation for the estimated delivered dose resulted in the EBT films receiving a dose ranging from 230 cGy to 300 cGy. The beam profiles in the horizontal and vertical axis of the BEV are shown in Fig. 6.5, and the FWHM and 20%-80% penumbra values are summarised in Table 6.1. The horizontal and vertical profiles taken from the 2D dose maps show a symmetric dose buildup and drop-off for the 20 mm and 10 mm collimators. Of particular interest is the 5 mm beam profiles and the evident asymmetry of the dose distribution. A 3D repre-

Table 6.1: Comparison of FWHM and 20%-80% penumbra for EBT3 film and MagicPlate-512

	Beam Diameter (mm)	Horizontal Film	MP512	Difference (mm)	Vertical Film	MP512	Difference (mm)
FWHM	20	23.172	22.282	0.89	23.333	22.405	0.928
	10	12.05	12.035	0.015	11.98	12.02	-0.04
	5	5.218	5.637	-0.419	6.062	5.751	0.311
Penumbra	20	2.017	2.655	-0.638	1.954	2.365	-0.411
	10	2.527	1.763	0.764	2.13	2.775	-0.645
	5	1.606	0.862	0.744	2.358	1.507	0.851

sentation of the 5 mm beam profile measured by film is presented in Fig. 6.5g to better visualise the asymmetry. Besides the reduced lateral electronic equilibrium, this small beam is also affected by irregularities present in the collimator due to its machining, and is thus asymmetric. The differences in penumbra and FWHM between film and MagicPlate detector are lower than 0.9 mm showing the suitability of MP512 to perform the quality check of the beam profiles in real-time prior to animal or cell samples irradiations. Spatial resolution of the EBT3 film is limited by the capabilities of the optical scanner and the uncertainty in the optical density curve fitting.

6.3.3 Beam Output Factors

The output factors for the different pencil beams are shown in Fig. 6.6. The uncertainties in the graph are due to the statistical variation in the film response and

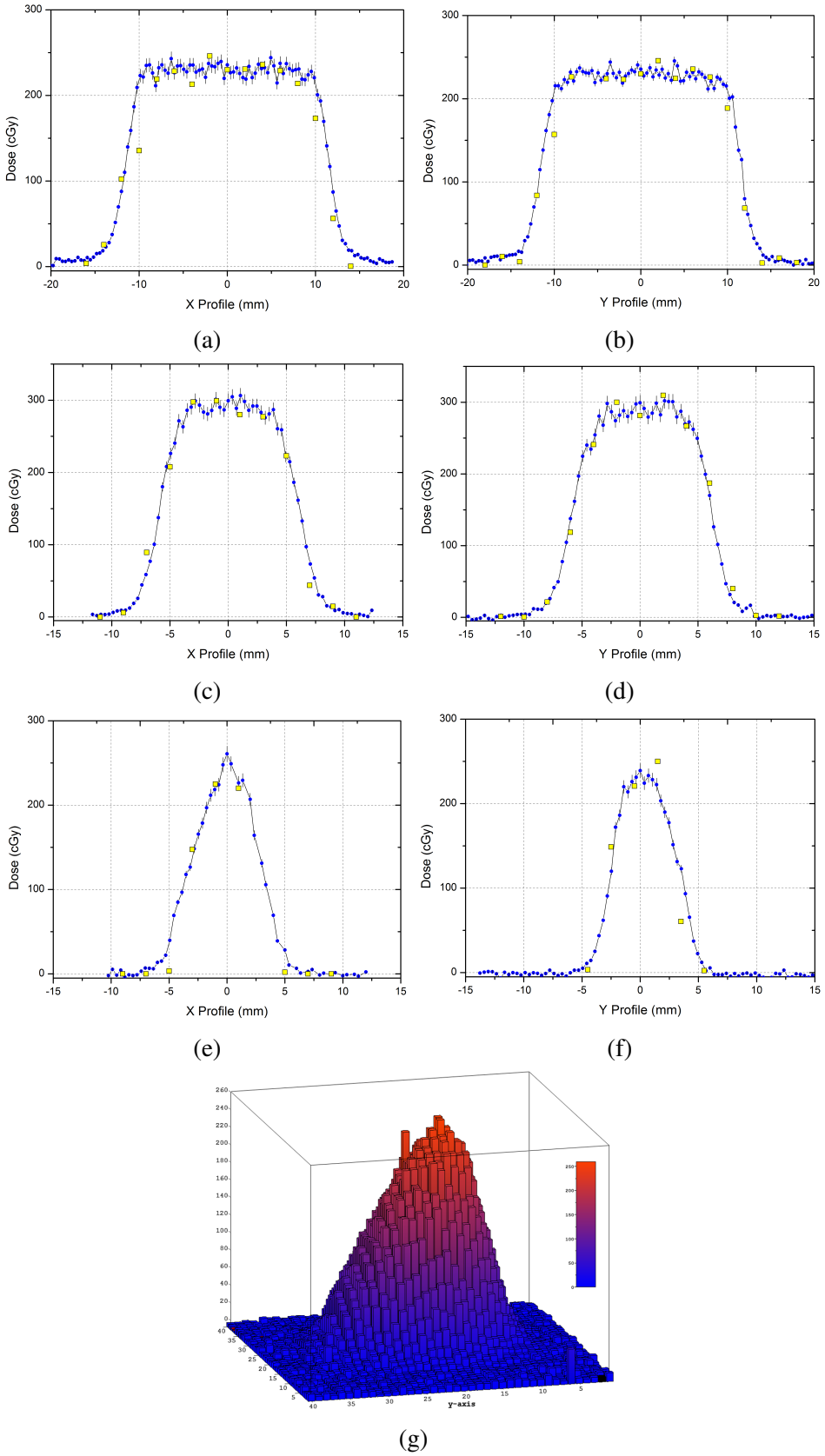

Figure 6.5: Dose profile measurements for (a)(b) 20 mm; (c)(d) 10 mm; and (e)(f) 5 mm beams using EBT3 film (blue) and MP512 (yellow). Error bars are due to the uncertainties in film response and alignment; (g) asymmetry of the 5 mm profile shown in 3D.

low SNR due to the very low dose rate delivered by the Co-60 irradiator. The error bars in the 5 mm data point are larger due to the asymmetry of the dose profile which affects the average dose calculated across the region of interest. The MP512 and film results agree within one standard deviation. The relatively large discrepancy between the ionisation chamber and MP512 results is due to the effect of the air gap on the response of the detector. Generally, silicon detectors over-respond to small-field dose with diameters of 20 mm or less (Underwood et al., 2013; Charles et al., 2012). The fact that the MP512 under-responds indicates that the perspex build-up envelope used to encase the detector is too thick and the secondary electrons generated inside the PMMA are filtered out without reaching the detector and reducing its response with respect to larger field size beams. Indeed the output factor of small beams can be modulated by the thickness of the air gap between the detector and the build-up material (Charles et al., 2012). Thus, the discrepancy in the MP512 output factor with respect to ionisation chamber can be mitigated by increasing the air gap above the detector array.

6.3.4 Shutter Timing Study

The irradiator is equipped with a pneumatic electronically controlled shutter to control the source exposure time. The shutter generates a ramp-up (and a ramp-down) dose distribution with respect to time because of its aperture mechanism which can potentially affect the accuracy of delivered dose if it is not taken into account.

The ramp-up and ramp-down transient study has been performed with the Romu-

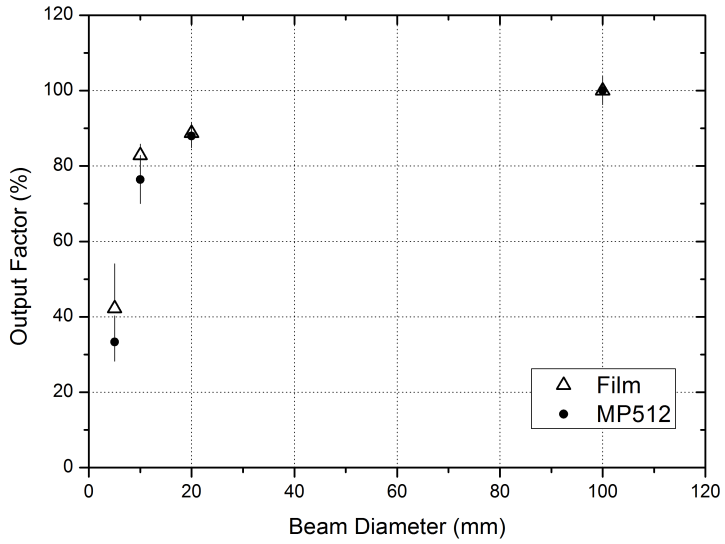

Figure 6.6: Output factors for EBT3 film and MagicPlate-512

lus data analysis toolkit. When the shutter is opened, the pixels on the left started 'seeing' the source before the pixels on the right (Fig. 6.2a). The duration of the shutter reaching the right quadrant was about (250 ± 10) ms. There was no delay between the top and bottom quadrants 'seeing' the source, as the pixels were exposed to the beam at the same time in the vertical direction. For the central pixels of interest, Δt_1 was found to be (151 ± 15) ms, and Δt_2 was (165 ± 15) ms. The dose (D_{t1}) associated with the interval Δt_1 was calculated to be ($1.23 \times 10^{-2} \pm 0.05 \times 10^{-2}$) cGy, and D_{t2} was calculated to be ($1.37 \times 10^{-2} \pm 0.05 \times 10^{-2}$) cGy, corresponding to a total transient dose of ($2.60 \times 10^{-2} \pm 0.0007$) cGy. The transient dose becomes non-negligible for small-dose irradiations (less than 1 cGy) and should be taken into account.

When the beam is turned on, the shutter exposes the cobalt source at a constant speed of about 20 ± 2 cm/s. It was observed that there was a variation of the Δt_2 parameter across the pixels in the horizontal direction, in the form of a residual tail

response as a function of time for the pixels in the left quadrant, when compared to pixels in the right quadrant, indicating that the shutter's speed is not constant when closing and concealing the source. It was found that in the first 50 ± 5 ms of the shutter beginning to close, the shutter covers about 50% of the MP512 detector's pixels, from right to left, corresponding to a shutter speed of around 55 cm/s. About 75% of the detector is covered in 250 ± 20 ms; at this stage, the shutter slows down to 16.5 cm/s. The remaining 25% in the far left quadrant of the detector takes up to 750 ms to be fully shielded by the shutter from the moment it begins to close. The average shutter closing speed was calculated to be (26 ± 4) cm/s. Thus, the shutter will traverse the 20 mm pencil beam in about 77 ms, and the 5 mm beam in 19 ms. Uncertainties in these results were due to the statistical fluctuations of the detector response. These were minimised by removing the noise baseline of the pixels of interest, if present.

The variation in the shutter speed as it closes is due to the shutter's transport mechanism. By default, the shutter is kept closed by a spring. When opening, a motor drives the shutter towards the spring, leading to a constant speed as observed by the MP512 detector; the motor actively keeps the shutter in the open position. To close the shutter, the power to the motor is temporarily cut off, leading to the spring relaxing and moving the shutter to conceal the source. About halfway through the movement, the motor re-engages to prevent the shutter from slamming and induce damage to the mechanical transport system. This 'active open' system ensures that even in the event of power loss, the source is automatically shielded by the spring-acted shutter.

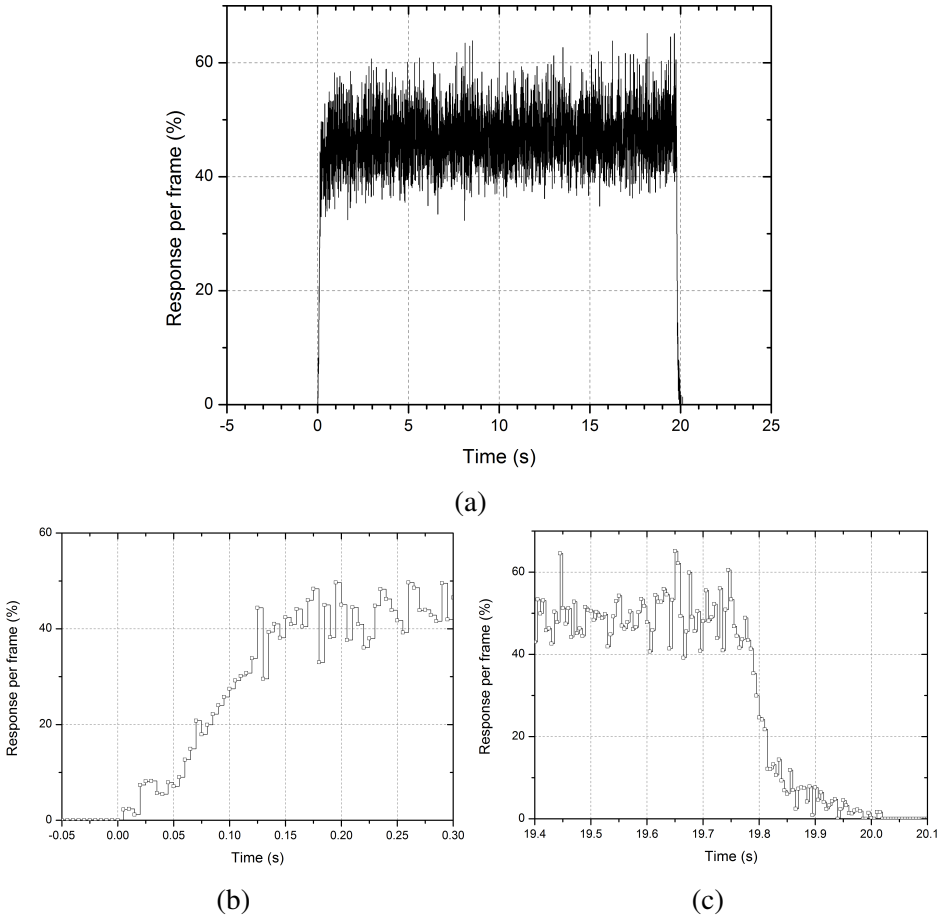

Figure 6.7: (a) Response of one pixel of interest from the center of MP512, chosen arbitrarily out of the four. The response is shown as a percentage of the dynamic range (0.5 pC); (b)(c) expanded view of the transients

6.4 Conclusion

In this study, the characteristics of a Theratron Co-60 source were investigated using an ionisation chamber, radiochromic EBT3 film and a silicon detector array system by CMRP, named MagicPlate-512. Dose rate of the Co-60 source was found to be (10.65 ± 0.03) cGy/min at 1.5 cm depth in SolidWater. Percentage depth dose measurements taken with IC and MP512 agree within 1% up to a depth of 50 mm in SolidWater. It was found that the 20 mm and 10 mm diameter beams have uniform penumbra regions. The 5 mm beam showed a significant asymmetric dose profile due to irregular machining of the lead collimator, which was visualised in 3D by the use of a plugin software of Romulus developed for this study. Full-width at half-maximum studies and 20%-80% penumbra evaluations performed with EBT3 film and MP512 agree within less than 1 mm. The uncertainties are due mainly to the very low level of current generated by the beam in the detector, of the order of few pA and the critical effect of radio-frequency interferences on the signal integrity. Output factors obtained with film and MagicPlate detector agree within one standard deviation for all three pencil beams, and the MP512 system under-responds compared to ionisation chamber at small field sizes, due to airgap thickness. MagicPlate-512 has been used to characterise the radiation source's shutter opening using a high temporal resolution and its high sensitivity. The shutter speed of the container was found to be around 20 cm/s when opening and 26 cm/s when closing, and the charge collected by the pixels for each acquisition was in the order of hundreds of picocoulombs. Despite the low source activity, the MagicPlate-512 dosimetry system has agreed within small uncertainties in comparison with ionisation chamber and EBT3 film proving

it is suitable for real-time verification of very low dose rate irradiators, providing high spatial and temporal resolution. A future study suggestion would be to use the OCTA detector to characterise the pencil beam profiles using sub-millimeter accuracy.

Chapter 7

Application of the Magicplate-512 System for Quality Assurance in Stereotactic Motion Adaptive Radiotherapy

This chapter has been published in Medical Physics:
M. Petasecca, M.K. Newall, J.T. Booth, M. Duncan, A.H. Aldosari, I. Fuduli, A.A. Espinoza, C. S. Porumb, S. Guatelli, P. Metcalfe, E. Colvill, D. Cammarano, M. Carolan, B. Oborn, M.L.F. Lerch, V. Perevertaylo, P.J. Keall, A.B. Rosenfeld, 2015, *MagicPlate-512: A 2D Silicon Detector Array for Quality Assurance of Stereotactic Motion Adaptive Radiotherapy*, Medical Physics, vol. 42, 2992, doi:10.1118/1.4921126

7.1 Introduction

Stereotactic radiosurgery (SRS) and stereotactic body radiotherapy (SBRT) are external beam modalities which use small beams to deliver high doses in small number of fractions. The modalities are used in treatment of brain tumors or sites where critical organ sparing is paramount to ensuring comfortable life for the patient post-treatment. The quality assurance for these types of treatment is challenging due to the necessity for detectors with high spatial resolution, high temporal resolution and zero energy dependence, to ensure accurate verification of the hypo-fractionated treatments delivered. In this chapter, the detector MagicPlate-512 with spatial resolution of 2 mm has been used to perform QA on a planned SBRT lung treatment with fields of 1×1 cm^2 up to 3×3 cm^2, and with induced motion of the target. The performance of the MP512 to resolve the beam profiles in comparison with EBT3 film is evaluated, as well as the temporal performance of the QA system is assessed.

7.2 Materials and Methods

The performance of the MP512 system in this study was assessed by observing the response of the detector for three square fields of 1×1 cm^2, 2×2 cm^2 and 3×3 cm^2, in three cases: no motion, motion, and motion with tracking. The FWHM and 20%-80% penumbra studies were performed in comparison with EBT3 film. The motion of the detector system was provided by the Scandidos HexaMotion motion platform, and the tracking of the system was performed with a Varian

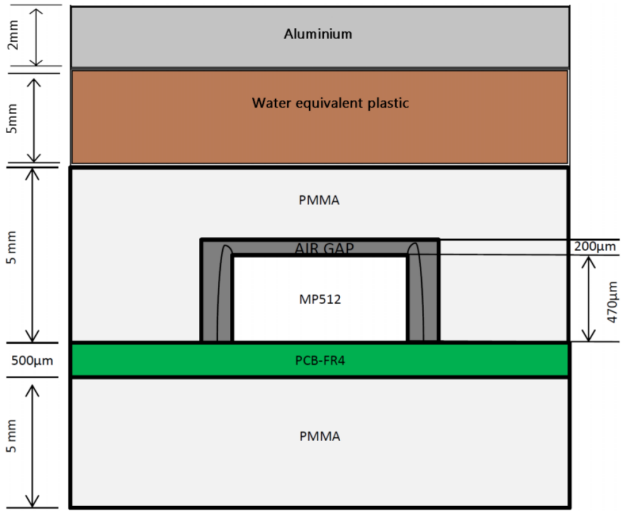

Figure 7.1: Schematic diagram of MP512 buildup (not to scale)

Calypso localisation system.

7.2.1 MagicPlate-512 Detector

The MP512 detector developed by CMRP is a monolithic silicon square array of diodes with pitch 2 mm and sensitive area of 0.5×0.5 mm^2. The detector has been described in Section 3.1.2.

7.2.2 Readout System

The readout system used in this study is the AFE-based electrometer and Romulus Radiation Tools software platform. Equalisation functionality of the software has been used to eliminate the variations in the response of individual pixels due to slight differences in the intrinsic properties of the *p*-*n* junctions, as described in Section 3.2.7.

7.2.3 Organ Motion Simulation

To simulate the organ movement, the MP512 detector was placed on 6 cm of SolidWater backscatter and placed on a modified HexaMotion platform by Scandidos (Uppsala, Sweden). The HexaMotion is a 6D motion platform designed as an accessory to the Delta^4 detector by the same company, in order to provide movement functionality for the commercial cylindrical QA device. The motion platform accepts the movement parameters from a text file and can be controlled from the linac bunker in the adjacent room. In this study, the motion system was modified using a wooden plate to accept the MP512 detector, readout system and SolidWater backscatter. The accuracy of the movement is greater than 0.5 mm. The lung motion simulated in this study was obtained from the 4D CT scan of a real patient and imported into HexaMotion. The movement plan had a temporal resolution of 25 ms and was simplified by only importing the $\times$ and y components of the patient's lung movement (Fig. 7.2). The z component of the lung movement was discarded in order to eliminate the dose rate and inverse square dependencies of the detector if it were to move away and towards the linac, as those parameters were out of the scope of this study.

7.2.4 Motion Tracking System

The tracking of the MP512 detector, which acted as the organ in motion in this study, was performed using the Calypso system by Varian (Palo Alto, CA). The purpose of the detector tracking was to feed in real-time the position of the target area (the MP512), which was varying due to the HexaMotion lung plan, to the

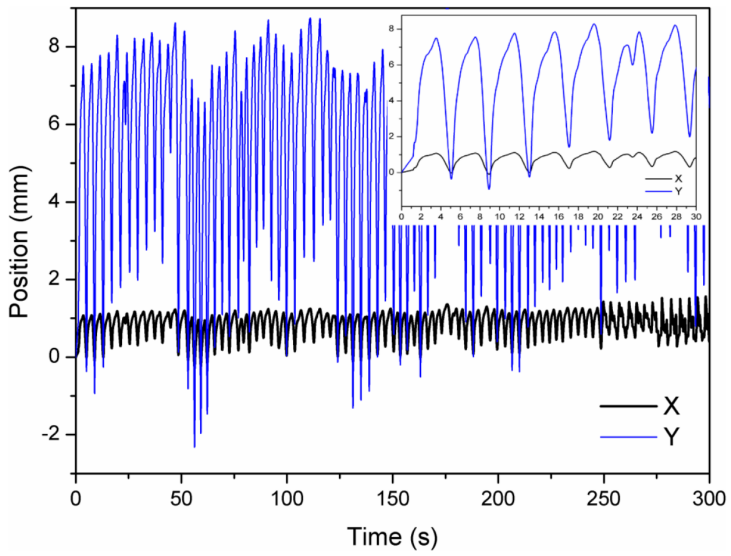

Figure 7.2: Diagram of imported patient lung motion simulated by the HexaMotion platform. The inset shows a 30 second section of the plan.

dynamic MLC (DMLC) so that the linac could compensate for the patient motion and conform the dose to the target volume within smaller tolerances. Calypso is a tracking system comprised of transceiver coils and RF transponder implant seeds known as 'beacons'. The array of transceiver coils is placed above the patient and emits a signal of 300-500 kHz, which excites the beacons and causes them to emit a resonant frequency unique to each beacon. Each signal is then recorded by the transponder coils as the relative distance to the beacons. A minimum number of three beacons must be used to successfully determine the center of mass of the target organ. The relative position of the Calypso system is made available to the linac by the use of infra-red cameras in the bunker room. Thus by knowing the relative position of the beacons with respect to the Calypso system, and the relative position of Calypso with respect to the IR cameras, the DMLC can account for organ movement and conform the small fields to the target volume. The feedback algorithm which drives the DMLC as a function of positioning data provided by

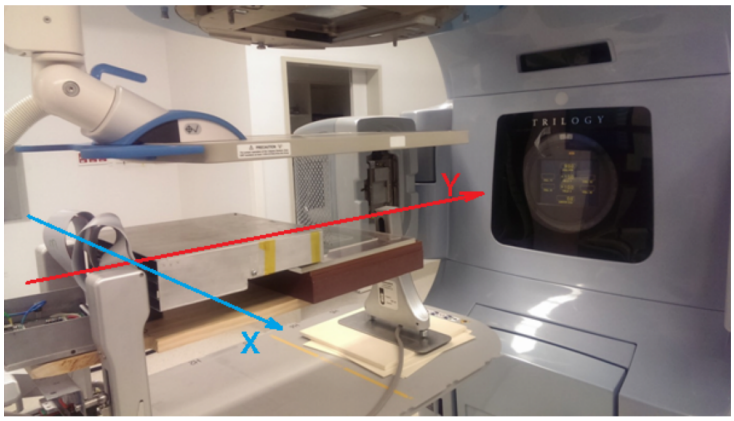

Figure 7.3: Experimental setup showing the MP512 system placed on the HexaMotion platform, on top of 6 cm SolidWater backscatter, and the direction of the axes. The Calypso motion system is visible between the detector and linac head.

Calypso has been developed by Keall *et al.* and successfully implemented in clinical practice (Keall et al., 2011, 2014).

7.2.5 Detector Packaging

For the successful use of the MP512 system in conjunction with Calypso, a custom RF shielding was necessary to be constructed for the detector and readout electronics, to avoid induced current in the detector wiring and analog front-end. The shielding was chosen to be constructed out of aluminium, and a calculation was performed to determine the thickness of aluminium required to attenuate the RF to 0.1% of the initial intensity. By approximating a 300 kHz plane wave traveling from the Calypso coils towards the detector with a normal angle of incidence on the aluminium, the Maxwell equation takes the form

$$\frac{\delta^2 E}{\delta z^2} = \mu_0 \mu_r \sigma \frac{\delta E}{\delta t} + i \mu_0 \mu_r \epsilon_0 \epsilon_r \omega \frac{\delta E}{\delta t}, \tag{7.1}$$

where ε_0 is the permittivity of free space (8.854×10^{-12} F/m); μ_0 is the permeability of free space ($4\pi \times 10^{-7}$ H/m); ω is the angular frequency ($2\pi \times 300 \times 10^3$ Hz); σ is the conductivity of aluminium (3.54×10^4 Ω^{-1}cm^{-1}); and μ_r is the relative permeability of aluminium, which is equal to 1 (Yamazaki et al., 2002). Due to the fact that $\sigma >> \omega\varepsilon_r\varepsilon_0$, an approximation can be made and the imaginary term can be ignored, leading to equation (7.1) being expressed as

$$\frac{\delta^2 E}{\delta z^2} = \mu_0 \mu_r \sigma \frac{\delta E}{\delta t} \tag{7.2}$$

The solution to equation (7.2) is in the form of

$$\mathbf{E} = \mathbf{E_0} exp(-\alpha z) expi(\omega t - \beta z), \tag{7.3}$$

where

$$\alpha = \beta = \sqrt{\frac{\mu_0 \mu_r \sigma \omega}{2}} \tag{7.4}$$

The skin depth, δ, for the 300 kHz Calypso RF wave is the inverse of $\alpha$and β, and its value is

$$\delta = \sqrt{\frac{2}{\mu_0 \mu_r \sigma \omega}} = 234 \mu m \tag{7.5}$$

For an attenuation of 99.9% of the RF wave, the calculation becomes

$$\frac{\mathbf{E_0} exp(\frac{-z}{2.34 \times 10^{-4}})}{\mathbf{E_0}} = 0.0018 \rightarrow z \approx 2\, mm \tag{7.6}$$

Thus, the required thickness of aluminium to reduce the RF to 0.1% of its initial intensity is around 2 mm. Petasecca et al. (2015) performed the Monte Carlo simulations with the aluminium shielding and found that using the 2 mm Al sheet

together with 5 mm SolidWater and 5 mm PMMA as buildup, the effective depth of the MP512 detector in this configuration corresponds to 1.5 cm d_{max} for a 6 MV beam. The results were verified using IC and agreement was within 1% between Geant4 and experimental results.

7.2.6 Beam Profiles

The profiles for 1×1, 2×2 and 3×3 cm^2 square fields were measured along horizontal and vertical axes using radiochromic film and MP512 detector. 1000 MU was delivered at 600 MU/min and 6 MV beam for three cases: no motion, motion, and motion with tracking. The fields were collimated by the MLC and the jaws were retracted in all directions by 1 cm to minimise leakage dose around the MLC leaves and to allow for the movement of the DMLC of 8 mm and 2 mm in Y- and X-direction, respectively. The MP512 detector was placed in the HexaMotion device above 6 cm SolidWater backscatter at 100 cm SAD and buildup as shown in Fig. 7.3. Three beacons were used for the organ tracking; they were fixed on a thin sheet of plastic 10 cm apart from one another. The sheet was then fixed on top of the Al shielding.

In the case of no motion, the movement platform was in the home position and the detector center was aligned to the isocenter of the beam, with the lasers crossing the central X- and Y- axes of MP512; Calypso RF field was enabled, but DMLC tracking was disabled.

In the case of motion with no tracking, the lung motion was imported into the HexaMotion platform and manually enabled, Calypso RF field was enabled, the

detector is aligned and the DMLC is disabled.

In the case of motion with tracking, the DMLC is following the motion of the lung pattern provided by the HexaMotion platform, using Calypso feedback, and according to the University of Sydney tracking software driver. Prediction was not used in this study.

The beam profiles were then repeated by removing the Al shielding, replacing MP512 with EBT3 film and adding SolidWater to effectively place the film at 1.5 cm d_{max}. Film scanning procedure was described in Section 6.2.5. The MP512 profiles were normalised to the central pixel and aligned to the position on the penumbra corresponding to 50% response of the central pixel. Film profiles were normalised to a central 2×2 mm^2 area surrounding the central axis. Comparisons of the FWHM and 20%-80% penumbra were performed using MATLAB curve fitting tool (shape-preserving). The results were tabulated in Table 7.1.

7.2.7 Temporal Performance of the System

The timing performance of the MP512 system was evaluated using the delivery of a dynamic wedge plan in the three modes described above. The advantage of being capable of resolving dose-per-pulse from the linac can be used to further improve the tracking algorithm of the DMLC and maximise healthy tissue sparing. 1000 MU was delivered using a 6 MV beam at 600 MU/min. The MP512 was placed at 1.5 cm equivalent depth and the angle of the linac gantry was kept constant to eliminate angular dependency of the detector. The motion of the phantom was in the same axis (Y) as the wedge delivered by the linac. The integral dose response

of the MP512 was compared with EBT3 film and an agreement evaluation was performed. Two MP512 pixels at positions (11, 13) and (8, 13) were chosen from the center of the wedge and closer to the penumbra region, respectively, which recorded about 50% of the integral dose compared to other detectors which received dose during the treatment plan. The response of the pixels in the case of no motion, motion, and motion with tracking was compared as the dynamic wedge traversed across the pixels.

7.3 Results

7.3.1 Detector Packaging

Fig. 7.4 shows, in the form of a histogram, the comparison between the baseline noise, the impact of Calypso's RF field and the effect of the aluminium shielding on the response of the MP512 detector. When unshielded, the detector measures stochastic fluctuations up to 9-10% of the dynamic range which are indistinguishable from the response of the detector when subjected to a real photon beam. This degrades the SNR of the system and increases the error bars of measurements, introducing inaccuracies in the total dose delivered and the dose-per-pulse evaluation of the beam. The latter is most affected, as it is less obvious when the beam is on and off.

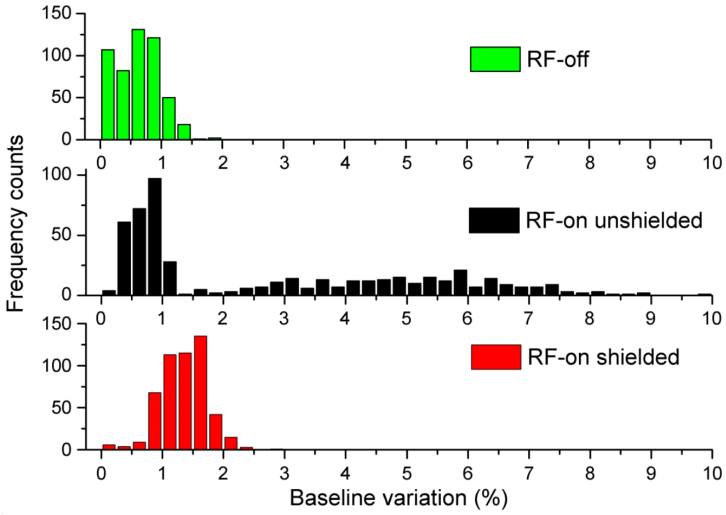

Figure 7.4: Comparison of the baseline distribution for the MP512 response for Calypso system off (green) and on (black and red). The positive effect of the aluminium shielding is clearly evident.

7.3.2 Beam Profiles

The profiles across the three beams in the case of no motion, motion, and motion with tracking are presented in Fig. 7.5 for Y-axis and in Fig. 7.6 for X-axis. Dose smearing in the case of organ motion is clearly evident by the asymmetry of the profiles, especially in the Y-axis, and the mitigation of this effect by the compensation of tracking is also clear by increasing the symmetry. Quantitatively, the comparison in the effect of motion is obvious in the difference of the size of the 20%-80% penumbra, which was evaluated on the right hand side of the profiles where the effect of the motion is most pronounced (Table 7.1). A difference of 2.4 mm average increase in penumbra is observed when the organ is in motion compared to no motion. This difference is reduced to 0.7 mm when tracking is activated; this corresponds to an effective reduction in motion effects of 70%. The profiles were taken with both MP512 and EBT3 film; agreement between the two

Table 7.1: Summary of FWHM and penumbra for MP512 and EBT3 film profiles

		EBT3		MP512	
Modality	Square Field size (cm)	FWHM (cm) ±0.01	RHS penumbra (cm) ±0.01	FWHM (cm) ±0.01	RHS penumbra (cm) ±0.01
No motion	1	1.14	0.26	1.17	0.25
	2	2.04	0.27	2.1	0.3
	3	3.06	0.3	3.16	0.29
Motion	1	1.16	0.5	1.21	0.51
	2	2.07	0.54	2.15	0.56
	3	3.1	0.53	3.15	0.57
Motion + tracking	1	1.1	0.35	1.14	0.37
	2	2.1	0.34	2.1	0.38
	3	3.1	0.35	3.12	0.39

detectors is within 3% and 0.4 mm for FWHM and penumbra, respectively.

The lung motion simulated in this study is less pronounced in the $\times$ axis, with a maximum displacement of ±0.5 mm compared to ±5 mm in the Y axis (Fig. 7.6). The minimum displacement which triggers a movement of the DMLC to compensate for the new organ position is 2 mm. Thus the difference in the $\times$ profiles is negligible.

7.3.3 Temporal Performance of the System

The timing performance of the MP512 detector system has been evaluated by irradiating the detector with a dynamic wedge plan (Fig. 7.7). Fig. 7.8 shows the integral dose deposition profiles for the three cases of no motion, motion, and motion with tracking, and the associated differences with respect to no motion.

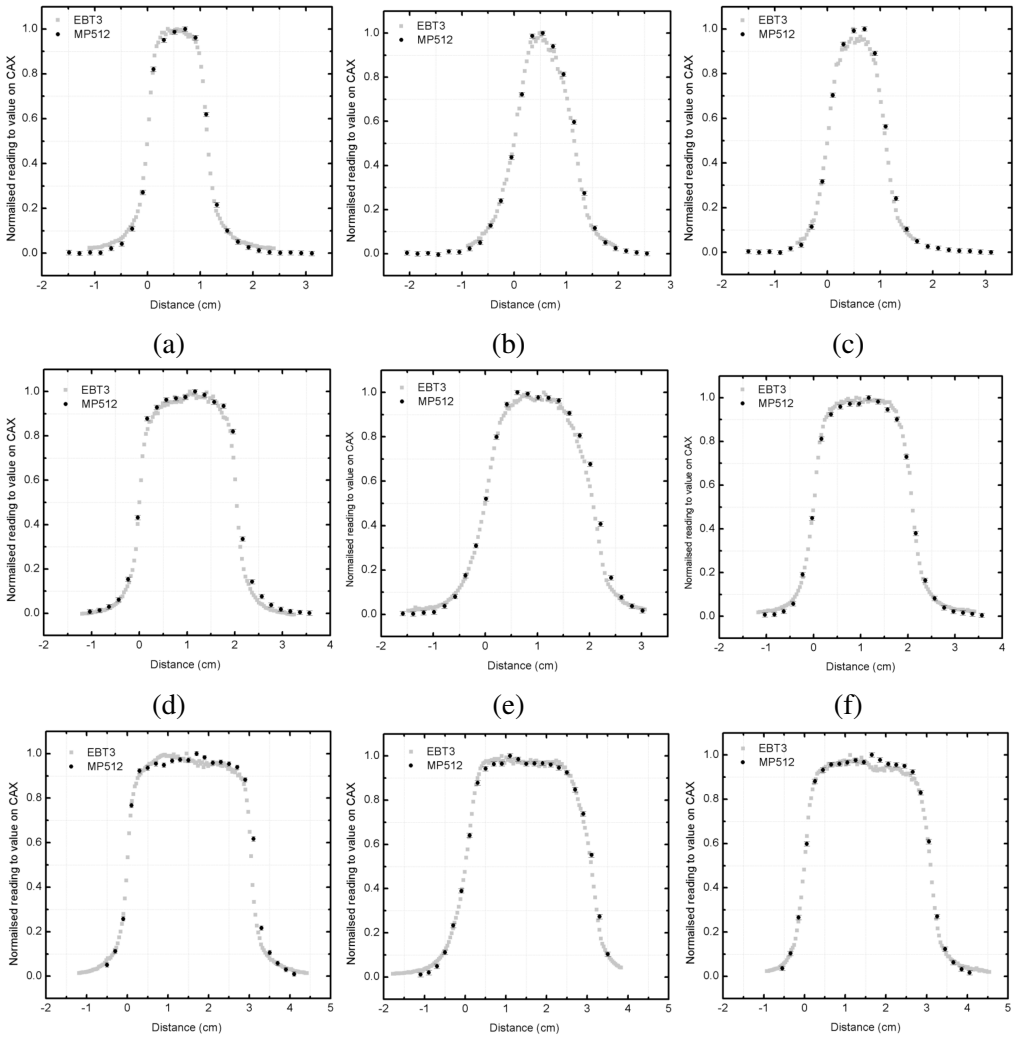

Figure 7.5: Profiles taken in the Y-axis using EBT3 film and MP512 for no motion (left), motion (center) and motion with tracking (right) for beam sizes 1×1 cm^2 (a) (b) (c), 2×2 cm^2 (d) (e) (f) and 3×3 cm^2 (g) (h) (i)

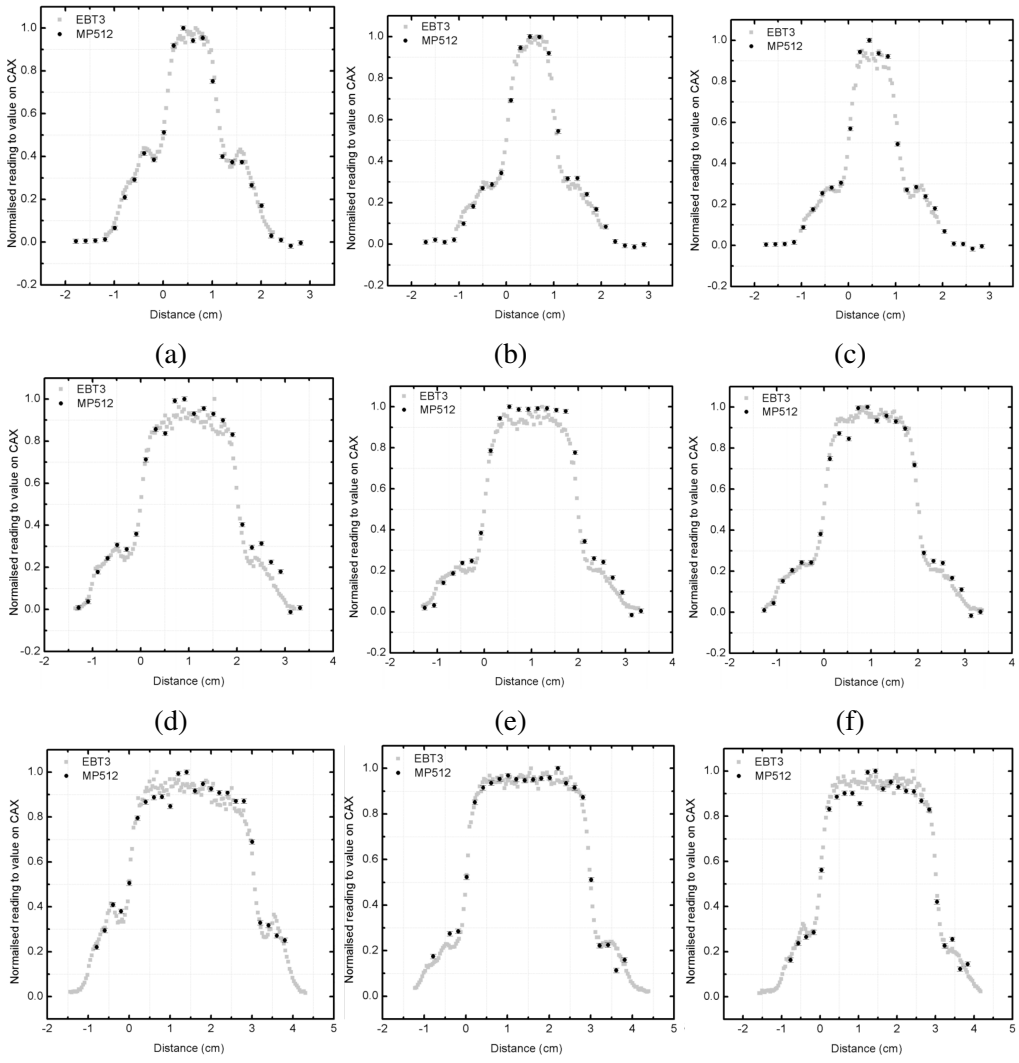

Figure 7.6: Profiles taken in the X-axis using EBT3 film and MP512 for no motion (left), motion (center) and motion with tracking (right) for beam sizes 1×1 cm^2 (a) (b) (c), 2×2 cm^2 (d) (e) (f) and 3×3 cm^2 (g) (h) (i)

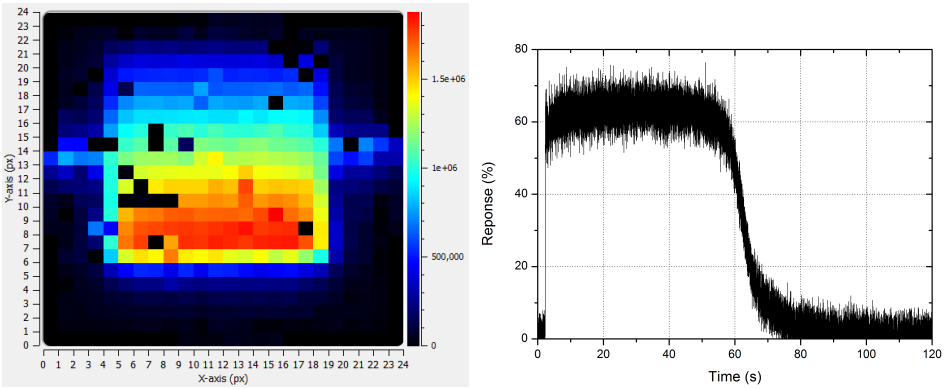

(a) (b)

Figure 7.7: (a) Response of the MP512 subjected to the dynamic wedge plan with no motion as visible in the Romulus off-line analysis mode; (b) raw response of the MP512 central pixel as a function of dynamic range for the same plan.

In the case of motion with no tracking, the difference along the integral dose distribution profile is -18% along the wedge, with a maximum deviation of +75% in the penumbra region. This corresponds to a displacement of 8 mm to 10 mm. In the case of motion correction, the difference is mitigated to -3% along the wedge and to a maximum of +15% in the penumbra region, which is in the range of 1.6 mm to 2 mm difference. The MP512 agrees well with the film profile, with variation of -18% along the wedge and +70% in the penumbra region in the case of motion with no tracking. Fig. 7.9 shows the comparison of the MP512 response and EBT3 film. Very good agreement is observed between the two detectors.

The temporal study of pixels (11, 13) and (8, 13) is shown in Fig. 7.10. Two pixels are presented in this study to show the difference in the temporal response of the pixels for a total delivered dose which is approximately the same. The black curve in the figure shows the response of pixel (11, 13) solely due to the scanning of the MLC which provides the dynamic wedge. In the first 20-25 seconds of beam-on,

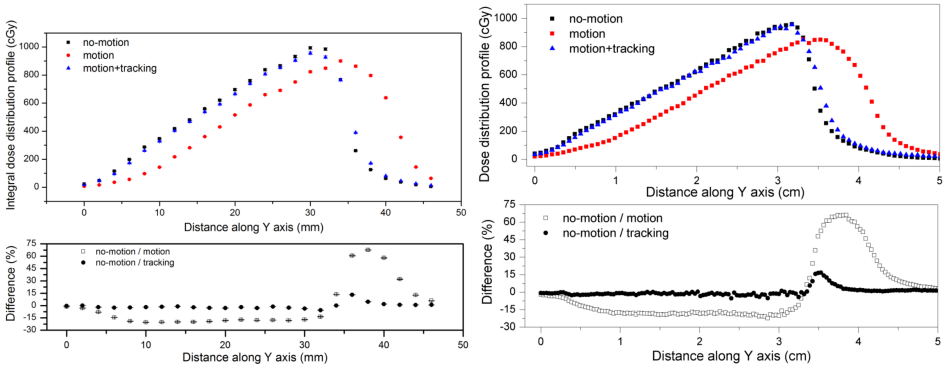

(a) (b)

Figure 7.8: Integral dose across the dynamic wedge profiles for no motion, motion and motion with tracking, depicting the percentage difference with respect to no motion, using MP512 (a) and EBT3 film (b)

the pixel is fully exposed to the beam. The response of the pixel slowly starts to decrease as it becomes collimated by the MLC, until complete shielding of the pixel occurs.

When the lung motion pattern is introduced, there are large spikes in the temporal response of the pixels which correspond with the pixels' maximum displacements entering and exiting the unshielded and shielded field of view of the beam. The spikes are most accentuated when the movement of the pixels traverses between the shielded and unshielded areas of the wedge, as shown by pixel (8, 13) in the range 25 s to 55 s. Small negative spikes in the response of pixel (11, 13) with motion in the first 20 seconds of beam-on coincide with the fastest motion of the respiratory pattern of the lung. The variation in the temporal response of the pixels is less for (11, 13) with motion and tracking, compared with pixel (8, 13) which, in this study, is not subject to tracking. This improvement is most evident in the region between 35 s and 45 s.

The latency between the tracking algorithm and the implementation of the correc-

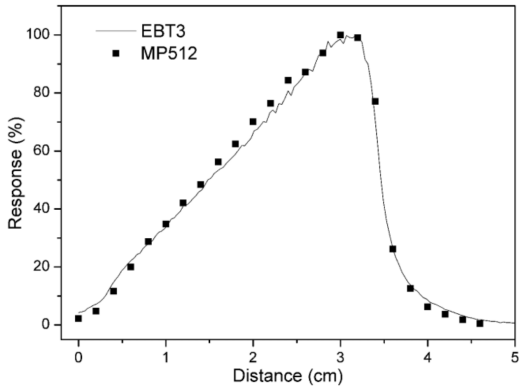

(a)

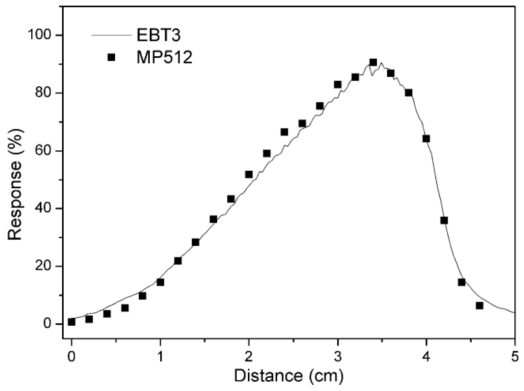

(b)

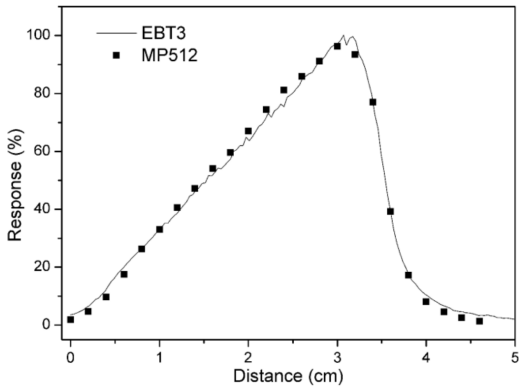

(c)

Figure 7.9: Comparison between EBT3 film and MP512 profiles of the dynamic wedge in the case of no motion (a), motion (b) and motion with tracking (c)

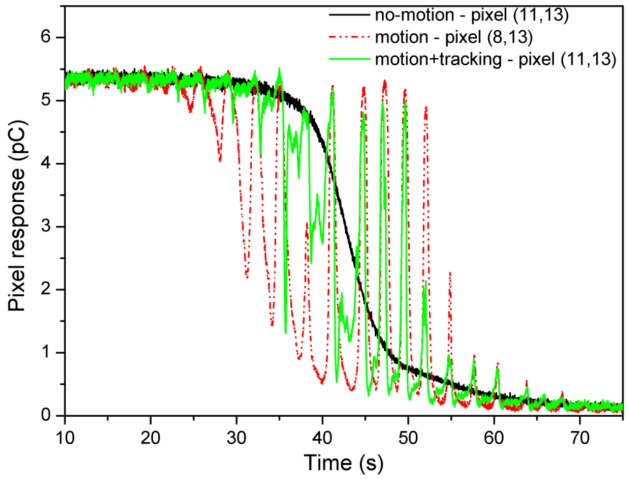

Figure 7.10: Temporal response of two MP512 pixels subjected to the dynamic wedge, for no motion, motion, and motion with tracking. The calibration factor is 5.81 nC/cGy.

tions has a latency of approximately 230 ms (Keall et al., 2014). An improvement to the tracking system would be to use a prediction algorithm which could take advantage of the high temporal resolution of MP512 to minimise the oscillations of the pixels' response due to the patient specific motion pattern.

7.4 Conclusion

In this work, the MagicPlate-512 system in conjunction with radiochromic EBT3 film has been used to evaluate the dose profiles of three stereotactic small beams, to quantify the performance of the MP512 for use as a quality assurance device in patient-specific SBRT plans involving organ motion. Excellent agreement has been found between MP512 and EBT3 film in the case of simulated lung motion experiments, with no motion, motion, and motion with tracking studies being performed. Agreement of 4% and less than 0.5 mm for FWHM and penumbra has

been found between MP512 and EBT3 film, respectively. Discrepancies as large as 10 mm can arise in the treatment of movable targets, which increase the planning target volume, and consequently the dose to healthy tissue surrounding the tumor. By utilising the high temporal resolution MP512 detector, which can synchronise to the linac and perform dose-per-pulse quality assurance, it is possible to reduce the irradiated volume and spare more healthy tissue by combining the use of MP512 with an organ tracking system such as Calypso, and DMLC motion tracking to compensate for organ movement. Predictive algorithms can further improve dose conformation to the tumor volume.

Chapter 8

Conclusion

This thesis was focused on the development of a data acquisition software for a novel EBRT quality assurance system, and the clinical and electrical characterisation of three monolithic detector arrays developed by Centre for Medical Radiation Physics. Furthermore, the application of the QA instrument was performed in quality assurance of *in-vivo* clinical IMRT, animal treatment using small cobalt-60 pencil beams, and QA of stereotactic motion adaptive radiotherapy. This chapter outlines the main findings of the thesis and discusses the future direction of the project.

8.1 Platform Design Architecture

The architecture of the CMRP QA device was described in this study. The design and development of a graphical user interface was thoroughly outlined, and the creation of software mapping algorithms for three silicon detector arrays with

different pixel configurations was presented. The structure of the DAQ software, named Romulus Radiation Tools, has been designed to be a multi-threaded approach comprised of two threads: one for the data acquisition and one for the graphical user interface. The DAQ thread was responsible solely with retrieving of binary encrypted data from the detector readout system. The GUI thread managed the real-time data decoding for prompt 2D visualisation of the detectors' response, 2D detector mapping using the generated pixel masks, and provided the functionality for the user to interact with the collected data. The GUI thread also provided the user with the off-line data analysis toolkit, which included per-pixel and batch analysis features such as obtaining the number of frames for a user-defined region of interest, integral pixel response, average response, charge collected, and uncertainty to within 95% confidence limits.

A 3D graphing add-on has been developed for Romulus, which enables the user to clearly visualise the shape of small stereotactic beam profiles and their associated penumbra regions using the response of the 2D detector arrays.

8.2 Evaluation of the Magicplate-121 System as a Dual Verification Device

The MagicPlate Dosimetry System using the MagicPlate-121 planar detector array was evaluated as a solution for pre-treatment and *in-vivo* dual verification quality assurance for IMRT. Two detectors were used in this study: the transmission detector which was mounted on the linac gantry and the dosimetry detector

which was placed in a cylindrical phantom. The setup allowed for pre-treatment QA using both detectors, and *in-vivo* QA using the radio-transparent detector in transmission mode. The performance of the rotatable phantom to follow the rotation of the gantry was evaluated. It was found that the phantom optical encoder was within ±1.5° of the nominal gantry angle for more than 95% of the time the tracking was enabled. A delay of about 400 ms between gantry and phantom was observed around the 22° position; this could be due to an irregularity on the transmission belt. Dose profiles at the depth of the dosimetry detector inside the cylindrical phantom agreed with the expected treatment plan dose within 1.3%. The MPDS successfully identified an introduced error in the dose rate for the *in-vivo* verification compared to the pre-treatment QA, and notified the user of the change.

Future studies include the use of the MP512 detector, or a larger area variant of the MP512, as the dose mode detector within the cylindrical phantom. This will greatly increase the spatial resolution of the measurements and will determine high dose gradient regions with increased accuracy.

8.3 Characterisation of Monolithic Silicon Detectors

The silicon detectors MagicPlate-512 and DUO have been characterised using a clinical linac to assess the detectors' linearity, uniformity, radiation damage and spatial resolution, and test structures of DUO and OCTA detectors' central pixels have been electrically characterised in terms of I-V and C-V, and charge collection efficiency and charge sharing properties have been investigated using a He^{2+} heavy

ion microprobe.

The MagicPlate-512 is a monolithic array of 0.5 $\times$ 0.5 mm^2 pixels arranged in a square. The detector demonstrated good linearity response up to 500 cGy and stabilisation of pixel response after 40 kGy irradiation with cobalt-60 gamma photons. The MP512 agrees with radiochromic film within 0.6 mm for FWHM and 20%-80% penumbra studies of stereotactic fields of size 2 cm, 1 cm and 0.5 cm. It was found that the uniformity of the MP512 was affected by thermal donors in the detector substrate distributed with cylindrical symmetry, affecting pixels at 17 mm around the center of the detector. This defect subsequently increased the relative response of the affected pixels for the Low *p*-stop concentration detector, and decreased the response for the High concentration *p*-stop detector. The artifact, present in all the MP512 detectors available in this study, is due to the Czochralski manufacturing technology of the silicon substrate. The effect of the "ring" of over-response can be mitigated with the use of a detector equalisation procedure applied to all pixels, in the case of Medium and High *p*-stop concentration detectors.

When subjected to high energy photon beams of 10 MV and above, the response of the MP512 detector decreases linearly at a rate of approximately 1% per every 33 Gy of delivered photon dose, due to photoneutron-induced defects in the silicon. The detector requires recalibration every 65 Gy of delivered dose in these conditions.

The DUO detector is an array of strips with size of 20 $\times$ 800 μm^2 and central pixellated structure dedicated to obtaining output factors for small stereotactic beamlets. The test structure pixels underwent breakdown in the range of 45-50 V

reverse bias. Leakage current was found to be in the order of 10^{-9} A at 40 V and capacitance of pixels was in the order of 10 pF at 10 V reverse bias. The detector demonstrated very good linearity response up to 500 cGy, with 95% of pixels lying within 1% of the mean after equalisation procedure. Stabilisation of response is achieved after pre-irradiating the detector with 140 cGy Co-60 photons. The detector agrees with radiochromic film within 0.35 mm for FWHM study, and within 0.58 mm for for 20%-80% penumbra for stereotactic fields of 2 cm and less. Charge collection efficiency is 66% in passive mode and crosstalk between pixels was found to be negligible.

The OCTA detector is a 512-channel silicon strip detector arranged in eight arrays at 45° to one another, around a common center. The sensitive area of each pixel is 40 $\times$ 800 μm^2. The central intersection of the arrays is comprised of nine square pixels of area 160 $\times$ 200 μm^2 each. In this study, the basic electrical characterisation, and charge collection efficiency and charge sharing study has been performed using the OCTA test structures. It was found that as with the DUO test structures, the OCTA pixels undergo breakdown at around 50 V reverse bias, and the leakage current is in the order of 10^{-9} A. The capacitance of the pixels is in the order of 10^{-12} F for all the pixels. Charge collection efficiency of the OCTA pixels is 73% in passive mode, due to a larger sensitive area of the pixels. There was a 10% low-energy crosstalk observed when sampling a strip pixel from an adjacent central (square) pixel.

Future work includes a comprehensive clinical characterisation of the OCTA detector, including percentage depth dose, linearity, uniformity, dose-per-pulse dependence and spatial resolution study. This will enable to determine the feasibility

of the OCTA for use in stereotactic radiotherapy quality assurance.

8.4 Characterisation of Cobalt-60 Pencil Beam Irradiator

The MagicPlate-512 data acquisition system was used in conjunction to radiochromic film and ionisation chamber to characterise a cobalt-60 pencil beam irradiator for use in animal radiotherapy, specifically for treatment of mice or rats. The irradiator, equipped with three collimators with machined holes of diameter 20 mm, 10 mm and 5 mm, was characterised in terms of percentage depth dose, output factor and shutter timing, and the beams were characterised in terms of profile shape, FWHM and penumbra.

Dose rate of the cobalt-60 source was calculated to be (10.65 ± 0.03) cGy/min and the percentage depth dose measurements using ionisation chamber and MP512 agreed within 2.4% up to a 50 mm depth in solid water. FWHM obtained with radiochromic film and MP512 agreed within 0.93 mm, and 20%/80% penumbra agreed within 0.85 mm. The 5 mm beam was found to have a non-uniform asymmetric profile shape due to the machining of the cavity. The shutter, operated by a motor and spring, was found to have a speed of 20 cm/s when opening and an average of 26 cm/s when closing. The total duration to fully open and close the shutter was calculated to be (250 ± 10) ms and (750 ± 10) ms, respectively.

A suggestion for a future study would be a characterisation of the pencil beam profiles with the OCTA detector. The higher spatial resolution of the detector

would provide a more detailed insight in the shape of the profiles, especially for the small 5 mm profile.

8.5 Application of the Magicplate-512 System for Stereotactic Motion Adaptive Radiotherapy

The MagicPlate-512 system was used in conjunction with radiochromic film to evaulate the dose profiles for three stereotactic beams, to assess the performance of the MagicPlate-512 system as a patient-specific SBRT quality assurance device involving organ motion. The study was performed using a simulated lung motion experiment. The MP512 and radiochromic film agreed within 4% and less than 0.5 mm for FWHM and penumbra, respectively. The dynamic MLC tracking functionality in conjunction with the Calypso tracking system and the high temporal resolution MagicPlate-512 system can help reduce the target volume of the tumor and movable target discrepancies, which could reduce the dose delivered to healthy tissue around the target and could help spare critical organs at risk. A suggestion for further work is to use the high temporal resolution of the MP512 system to minimise the latency between the tracking algorithm and the implementation of corrections by developing a prediction algorithm.

Bibliography

M.I. Al-Saleh, A. Espinoza, and J.R. Crandall. Antivirus Performance Characterisation: System-wide View. *IET Information Security*, 7.2:126–133, 2013.

S. Alashrah, S. Kandaiya, S.Y. Yong, and S.K. Cheng. Characterization of a 2D Ionization Chamber Array For IMRT Plan Verification. *Nuclear Instruments and Methods in Physics Research*, A619:181–185, 2010.

S. Alashrah, S. Kandaiya, L.S. Lum, and S.K. Cheng. Depth Dependence of the Single Chamber Response Function of the ImRT MatriXX Array in a 6MV Photon Beam. *Zeitschrift für Medizinische Physik*, 23(4):270–278, 2013.

A.H. Aldosari, A. Espinoza, D. Robinson, I. Fuduli, C. Porumb, S. Alshaikh, M. Carolan, M.L.F. Lerch, Member, V. Perevertaylo, A.B. Rosenfeld, and M.Petasecca. Characterization of an Innovative p-type Epitaxial Diode for Dosimetry in Modern External Beam Radiotherapy. *IEEE Transactions on Nuclear Science*, 60(6):4705–4712, 2013.

A.H. Aldosari, M. Petasecca, A. Espinoza, M. Newall, I. Fuduli, C. Porumb, S. Alshaikh, Z.A. Alrowaili, M. Weaver, P. Metcalfe, M. Carolan, M.L.F. Lerch, V. Perevertaylo, and A.B. Rosenfeld. A Two Dimensional Silicon Detectors Ar-

ray for Quality Assurance in Stereotactic Radiotherapy: MagicPlate-512. *Medical Physics*, 41(9):091707 1–10, 2014.

B. Allgaier, E. Schüle, and J. Würfel. Dose Reconstruction in the OCTAVIUS 4D Phantom and in the Patient Without Using Dose Information From the TPS. *PTW White Paper*, D913.200.06/00:1–8, 2013.

Z.A. Alrowaili, M.L.F. Lerch, M. Carolan, I. Fuduli, C. Porumb, M. Petasecca, P. Metcalfe, and A.B. Rosenfeld. 2D Mapping of the MV Photon Fluence and 3D Dose Reconstruction in Real Time for Quality Assurance During Radiotherapy Treatment. *Journal of Instrumentation*, 10:1–14, 2015.

Z.A. Alrowaili, M.L.F. Lerch, M. Petasecca, M.G. Carolan, P.E. Metcalfe, and A.B. Rosenfeld. Beam Perturbation Characteristics of a 2D Transmission Silicon Diode Array 'Magic Plate'. *Journal of Applied Clinical Medical Physics*, 17(2):5932, 2016.

M. Aristophanous, Y. Suh, P.C. Chi, L.J. Whittlesey, S. LaNeave, and M.K. Martel. Initial Clinical Experience with ArcCHECK for IMRT/VMAT QA. *Journal of Applied Clinical Medical Physics*, 17(5):20–33, 2016.

F.H. Attix. *Introduction to Radiological Physics and Radiation Dosimetry*. Wiley, 2004.

G. I. Ayzenshtat, V. P. Germogenov, S. M. Guschin, L. S. Okaevich, O. G. Shmakov, O. P. Tolbanov, and A. P. Vorobiev. X-ray and Gamma-ray Detectors Based on GaAs Epitaxial Structures. *Nuclear Instruments & Methods in Physics Research*, 531:97–102, 2004.

M.C. Aznar, C.E. Andersen, L. Bøtter-Jensen, S.Å. Bäck, S. Mattsson, J. Medin, and F. Kjær-Kristoffersen. Real-time Optical-fibre Luminescence Dosimetry for Radiotherapy: Physical Characteristics and Applications in Photon Beams. *Physics in Medicine and Biology*, 49(9):1655–1669, 2004.

E.H. Balagamwala, S.T. Chao, and J.H. Suh. Principles of Radiobiology of Stereotactic Radiosurgery and Clinical Applications in the Central Nervous System. *Technology in Cancer Research & Treatment*, 11(1):3–13, 2012.

A.S. Beddar, T.R. Mackie, and F.H. Attix. Water-equivalent Plastic Scintillation Detectors for High-Energy Beam Dosimetry: I. Physical Characteristics And Theoretical Considerations. *Physics in Medicine and Biology*, 37(10):1883–1900, 1992.

A.S. Beddar, N. Suchowerska, and S.H. Law. Plastic Scintillation Dosimetry for Radiation Therapy: Minimizing Capture of Cerenkov Radiation Noise. *Physics in Medicine and Biology*, 49:783–790, 2004.

J. L. Bedford, Y. K. Lee, P. Wai, C.P. South, and A.P. Warrington. Evaluation of the Delta^4 Phantom for IMRT and VMAT Verification. *Physics in Medicine and Biology*, 54(9):167–176, 2009.

M.J. Berger, J.S. Coursey, M.A. Zucker, and J. Chang. Stopping-Power and Range Tables for Electrons, Protons, and Helium Ions, 2015. URL http://www.nist.gov/pml/data/star/.

A. Bocci, M.A. Cortés-Giraldo, M.I. Gallardo, J.M. Espino, R. Arráns, M.A.G. Alvarez, Z. Abou-Haïdar, J.M. Quesada, A. Pérez Vega-Leal, and F.J. Pérez Nieto. Silicon Strip Detector for a Novel 2D Dosimetric Method for Radiotherapy

Treatment Verification. *Nuclear Instruments and Methods in Physics Research Section A: Accelerators, Spectrometers, Detectors and Associated Equipment*, 673:98–106, 2012.

G.C. Bonazzola, R. Cirio, M. Donetti, F. Marchetto, G. Mazza, C. Peroni, and A. Zampieri. Performances of a VLSI Wide Dynamic Range Current-To-Frequency Converter for Strip Ionization Chambers. *Nuclear Instruments and Methods in Physics Research Section A: Accelerators, Spectrometers, Detectors and Associated Equipment*, 405(1):111–120, 1998.

E. Borchi and M. Bruzzi. Radiation-Damage in Silicon Detectors. *Rivista Del Nuovo Cimento*, 17(11):1–63, 1994.

T. Bortfeld. IMRT: A Review and Preview. *Physics in Medicine and Biology*, 51(13):R363–379, 2006.

A. Brahme, J.E. Roos, and I. Lax. Solution of an Integral Equation Encountered in Rotation Therapy. *Physics in Medicine and Biology*, 27:1221–1229, 1982.

M. Bruzzi. Radiation damage in silicon detectors for high-energy physics experiments. *IEEE Transactions on Nuclear Science*, 48(4):960–971, 2001.

M. Bruzzi, M. Bucciolini, M. Casati, D. Menichelli, C. Talamonti, C. Piemonte, and B.G. Svensson. Epitaxial Silicon Devices for Dosimetry Applications. *Applied Physics Letters*, 90:172109–1–172109–3, 2007.

M. Bucciolini, F.B. Buonamici, S. Mazzocchi, C. De Angelis, S. Onori, and G.A.P. Cirrone. Diamond Detector Versus Silicon Diode and Ion Chamber

in Photon Beams of Different Energy and Field Size. *Medical Physics*, 30(8): 2149–2154, 2003.

M.J. Butson, P.K.N. Yu, T. Cheung, and P. Metcalfe. Radiochromic Film for Medical Radiation Dosimetry. *Materials Science and Engineering*, R 41:61–120, 2003.

D. Chapman, R. Barnett, and S. Yartsev. Helical Tomotherapy Quality Assurance with ArcCHECK. *Medical Dosimetry*, 39:159–162, 2014.

P.H. Charles, S.B. Crowe, T. Kairn, J. Kenny, J. Lehmann, J. Lye, L. Dunn, B. Hill, R.T Knight, C.M. Langton, and J.V. Trapp. The Effect of Very Small Air Gaps on Small Field Dosimetry. *Physics in Medicine and Biology*, 57:6947–6960, 2012.

P.H. Charles, G. Cranmer-Sargison, D.I. Thwaites, S.B. Crowe, T. Kairn, R.T. Knight, J. Kenny, C.M. Langton, and J.V. Trapp. A Practical and Theoretical Definition of Very Small Field Size for Radiotherapy Output Factor Measurements. *Medical Physics*, 41(4):041707, 2014.

K. Chelminski, P.K. Sobotka, W. Bulski, M. Kuich, K. Milanowska, and A.W. Domanski. Validation of ArcCHECK Matrix of Semiconducting Detectors for Dosimetry Verification in Radiotherapy. *Radiotherapy and Oncology*, Suppl 1: S500, 2012.

I.M. Cornelius, I. Orlic, R. Siegele, A.B. Rosenfeld, and D.D. Cohen. Ion Beam Induced Charge Collection Time Imaging of a Silicon Microdosimeter. *Nuclear Instruments and Methods in Physics B*, 210:191–195, 2013.

P. Cross. The Use of Parallel Plate Ion Chambers to Determine Surface Dose of a 6 MV Photon Beam. *Australasian Physical and Engineering Sciences in Medicine*, 15(4):208–213, 1992.

I.J. Das, G. Ding, and A. Ahnesjö. Small Fields: Nonequilibrium Radiation Dosimetry. *Medical Physics*, 35(1):206–215, 2008.

E. De Martin, Fiorino C., Broggi S., Longobardi B., Pierelli A., Perna L., Cattaneo G.M., and Calandrino R. Agreement Criteria Between Expected and Measured Field Fluences in IMRT of Head and Neck Cancer: The Importance and Use of the Gamma Histograms Statistical Analysis. *Radiotherapy and Oncology*, 85: 399–406, 2007.

P.P. Dendy and B. Heaton. *Physics for Diagnostic Radiology*. CRC Press, 1999.

F. dErrico, R. Nath, L. Tana, G. Curzio, and W.G. Alberts. In-phantom dosimetry and spectrometry of photoneutrons from an 18 MV linear accelerator. *Medical Physics*, 25(9):1717–1724, 1998.

Topical Review: Polymer Gel Dosimetry. Baldock, C. and Y. De Deene and S. Doran and G. Ibbott and A. Jirasek and M. Lepage and K.B. McAuley and M. Oldham and L.J. Schreiner. *Physics in Medicine and Biology*, 55(5):R1–R63, 2010.

V. Feygelman, G. Zhang, C. Stevens, and B.E. Nelms. Evaluation of a New VMAT QA Device, or the "X" and "O" Array Geometries. *Journal of Applied Clinical Medical Physics*, 12(2):146–168, 2011.

A. Fogliata, G. Nicolini, M. Alber, M. Asell, B. Dobler, M. El-Haddad,

B. Hårdemark, U. Jelen, A. Kania, M. Larsson, F. Lohr, T. Munger, E. Negri, C. Rodrigues, and L. Cozzi. IMRT for Breast. A Planning Study. *Radiotherapy and Oncology*, 76:300–310, 2005.

A.-M. Frelin, J.-M. Fontbonne, G. Ban, A. Batalla, J. Colin, A. Isambert, M. Labalme, T. Leroux, and A. Vela. A New Scintillating Fiber Dosimeter Using a Single Optical Fiber and a CCD Camera. *IEEE Transactions on Nuclear Science*, 53(3):1113–1117, 2006.

I. Fuduli, C. Porumb, A.A. Espinoza, A.H. Aldosari, M. Carolan, M.L.F Lerch, P. Metcalfe, A.B. Rosenfeld, and M. Petasecca. A Comparative Analysis of Multichannel Data Acquisition Systems for Quality Assurance in External Beam Radiation Therapy. *Journal of Instrumentation*, 9(6):1–12, 2014.

D.M. González-Castaño, F. Gómez, L. Brualla, J.V. Roselló, D. Planes, M. Sánchez, and M. Pombar. A Liquid-filled Ionization Chamber for High Precision Relative Dosimetry. *Physica Medica*, 27:89–96, 2011.

Intensity Modulated Radiation Therapy Collaborative Working Group. Intensity-Modulated Radiotherapy: Current Status and Issues of Interest. *International Journal of Radiation Oncology, Biology, Physics*, 51:880–914, 2001.

M. Heydarian, P.W. Hoban, and A.H. Beddoe. A Comparison of Dosimetry Techniques in Stereotactic Radiosurgery. *Physics in Medicine and Biology*, 41(1): 93–110, 1996.

P.J. Keall, Sawant A, Cho B, Ruan D, Wu J, Poulsen P, Petersen J, Newell L.J., Cattell H, and Korreman S. Electromagnetic-guided Dynamic Multileaf Collimator Tracking Enables Motion Management for Intensity-Modulated Arc

Therapy. *International Journal of Radiation Oncology, Biology, Physics*, 79(1): 312–320, 2011.

P.J. Keall, E. Colvill, R. OBrien, J.A. Ng, P.R. Poulsen, T. Eade, A. Kneebone, and J.T. Booth. The First Clinical Implementation of Electromagnetic Transponder-Guided MLC Tracking. *Medical Physics*, 41(2):020702 (5pp.), 2014.

H.S. Kim and J.K. Lee. Assessment and Measurement of the Photoneutron Field Produced in the Varian Medical Linear Accelerator. *Journal of Nuclear Science and Technology*, 44(1):95–101, 2007.

F.P. Korshunov, S.B. Lastovskii, V.P. Markevich, L.I. Murin, Y.V. Bogatyrev, and A.R. Peaker. Defect-Impurity Complexes With High Thermal Stability in epi-Si n+ -p Diodes Irradiated With MeV Electrons. *Vacuum*, 83:S131–S133, 2009.

J. Kozelka, J. Robinson, B. Nelms, G. Zhang, D. Savitskij, and V. Feygelman. Optimizing the Accuracy of a Helical Diode Array Dosimeter: A Comprehensive Calibration Methodology Coupled with a Novel Virtual Inclinometer. *Medical Physics*, 38(9):5021–5032, 2011.

H.W. Kraner. Radiation Damage in Silicon Detectors. *Nuclear Instruments and Methods in Physics Research*, 225(3):615–618, 1984.

J. Lambert, Y. Yin, D.R. McKenzie, S. Law, and N. Suchowerska. Cerenkov-Free Scintillation Dosimetry in External Beam Radiotherapy with an Air Core Light Guide. *Physics in Medicine and Biology*, 53:3071–3080, 2008.

S.H. Law, N. Suchowerska, D.R. McKenzie, S.C. Fleming, and T. Lin. Transmis-

sion of Cerenkov Radiation in Optical Fibers. *Optics Letters*, 32:1205–1207, 2007.

D. L'Étourneau, M. Gulam, D. Yan, M. Oldham, and J.W. Wong. Evaluation of a 2D diode array for IMRT Quality Assurance. *Radiotherapy & Oncology*, 70: 199–206, 2003.

Z. Li. Radiation damage effects in Si materials and detectors and rad-hard Si detectors for SLHC. *Journal of Instrumentation*, 4(3):1–31, 2009.

D.A. Low, J.M. Moran, J.F. Dempsey, L. Dong, and M. Oldham. Dosimetry Tools and Techniques for IMRT. *Medical Physics*, 38(3):1313–1338, 2011.

P. Maj, A. Baumbaugh, G. Deptuch, P. Grybos, and R. Szczygiel. Algorithms for Minimization of Charge Sharing Effects in a Hybrid Pixel Detector Taking Into Account Hardware Limitations in Deep Submicron Technology. *Journal of Instrumentation*, 7:C12020, 2012.

M.M. Matuszak, D. Yan, and I. Grills. Clinical Applications of Volumetric Modulated Arc Therapy. *International Journal of Radiation Oncology, Biology, Physics*, 77(2):608–616, 2010.

C.K. McGarry, B.F. O'Connell, M.W.D. Grattan, C.E. Agnew, D.M. Irvine, and A.R. Hounsell. Octavius 4D Characterization for Flattened and Flattening Filter Free Rotational Deliveries. *Medical Physics*, 40(9):091707 1–11, 2013.

D. Menichelli, M. Bruzzi, M. Bucciolini, C. Talamonti, M. Casati, L. Marrazzo, M. Tesi, C. Piemonte, A. Pozza, N. Zorzi, M. Brianzi, and A. De Sio. Design and Development of a Silicon-Segmented Detector for 2D Dose Measurements

in Radiotherapy. *Nuclear Instruments and Methods in Physics Research*, 583: 109–113, 2007.

S. Miljanić, M. Ranogajec-Komor, Ž. Knežević, and B. Vekić. Main Dosimetric Characteristics of Some Tissue-Equivalent TL Detectors. *Radiation Protection Dosimetry*, 100:437–442, 2002.

M. Moll. Radiation Tolerant Semiconductor Sensors for Tracking Detectors. *Nuclear Instruments and Methods in Physics Research Section A: Accelerators, Spectrometers, Detectors and Associated Equipment*, 565(1):202–211, 2006.

M. Moll, E. Fretwurst, and G. Lindström. Investigation on the Improved Radiation Hardness of Silicon Detectors with High Oxygen Concentration. *Nuclear Instruments and Methods in Physics Research Section A: Accelerators, Spectrometers, Detectors and Associated Equipment*, 439(2):282–292, 2000.

B.E. Nelms, D. Opp, J. Robinson, T.K Wolf, G. Zhang, E. Moros, and V. Feygelman. VMAT QA: Measurement-guided 4D Dose Reconstruction on a Patient. *Medical Physics*, 39(7):4228–4238, 2012.

A.J. Olch. Evaluation of the Accuracy of 3DVH Software Estimates of Dose to Virtual Ion Chamber and Film in Composite IMRT QA. *Medical Physics*, 39(1):81–86, 2012.

K. Otto. Volumetric Modulated Arc Therapy: IMRT in a Single Gantry Arc. *Medical Physics*, 35(1):310–317, 2008.

M. Petasecca, A. Cullen, I. Fuduli, A. Espinoza, C. Porumb, C. Stanton, A.H. Aldosari, Bräuer-Krisch, H. Requardt, A. Bravin, V. Perevertaylo, A.B. Rosen-

feld, and M.L.F. Lerch. X-tream: A Novel Dosimetry System for Synchrotron Microbeam Radiation Therapy. *Journal of Instrumentation*, 7(7):P07022, 2012.

M Petasecca, M.K. Newall, J.T. Booth, M. Duncan, A.H. Aldosari, I. Fuduli, A.A. Espinoza, C.S. Porumb, S. Guatelli, P. Metcalfe, E. Colvill, D. Cammarano, M. Carolan, B. Oborn, M.L.F. Lerch, V. Perevertaylo, P.J. Keall, and A.B. Rosenfeld. MagicPlate-512: A 2D Silicon Detector Array for Quality Assurance of Stereotactic Motion Adaptive Radiotherapy. *Medical Physics*, 42(6): 2992–3004, 2015.

E.B. Podgorsak. *Radiation Oncology Physics: A handbook for Teachers and Students*. Internation Atomic Energy Agency, 2005.

B. Poppe, T.S. Stelljes, H.K. Looe, and N. Chofor. Performance Parameters of a Liquid Flled Ionization Chamber Array. *Medical Physics*, 40(8):082106 1–14, 2013.

C.S. Porumb, A.H. Aldosari, I. Fuduli, D. Cutajar, M. Newall, P. Metcalfe, M. Carolan, M.L.F. Lerch, V.L. Perevertaylo, A.B. Rosenfeld, and M. Petasecca. Characterisation of Silicon Diode Arrays for Dosimetry in External Beam Radiation Therapy. *IEEE Transactions on Nuclear Science*, 63(3): 1808–1817, 2016.

R. Murphy. USB 101: An Introduction To Universal Serial Bus 2.0, 2016. URL http://www.cypress.com/file/134171/download.

G. Rikner and E. Grusell. General Specifications for Silicon Semiconductors for Use in Radiation Dosimetry. *Physics in Medicine and Biology*, 32(9):1109–1117, 1987.

R. Sadagopan, J.A. Bencomo, R.L. Martin, G. Nilsson, T. Matzen, and P.A. Balter. Characterization and Clinical Evaluation of a Novel IMRT Quality Assurance System. *Journal of Applied Clinical Medical Physics*, 10(2):2928, 2009.

L.J. Schreiner. Review of Fricke Gel Dosimeters. *Journal of Physics*, 3:9–21, 2004.

S. Sciortino, F. Hartjes, S. Lagomarsino, F. Nava, M. Brianzi, V. Cindro, C. Lanzieri, M. Moll, and P. Vanni. Effect of Heavy Proton and Neutron Irradiations on Epitaxial 4H-SiC Schottky Diodes. *Nuclear Instruments & Methods in Physics Research*, 552:138–145, 2005.

J. Shi, W.E. Simon, and T.C. Zhu. Modeling The Instantaneous Dose Rate Dependence of Radiation Diode Detectors. *Medical Physics*, 30(9):2509–2519, 2003.

W. Shockley and W.T. Read. Statistics of the Recombinations of Holes and Electrons. *Physical Review*, 87(5):835, 1952.

T.A. Simon, W. E. Simon, D. Kahler, J. Li, and C. Liu. Wide Field Array Calibration Dependence on the Stability of Measured Dose Distributions. *Medical Physics*, 37(7):3501–3509, 2010.

S.M. Sze and K.K. Ng. *Physics of Semiconductor Devices*. Wiley, 2007.

S. Takahashi. Conformation Radiotherapy: Rotation Techniques as Applied to Radiography and Radiotherapy of Cancer. *Acta Radiol. Suppl.*, 242:1–142, 1965.

C. Talamonti, M. Bruzzi, M. Bucciolini, L. Marrazzo, and D. Menichelli. Preliminary Dosimetric Characterization of a Silicon Segmented Detector for 2D Dose Verifications in Radiotherapy. *Nuclear Instruments & Methods in Physics Research*, 583:114–118, 2007.

Texas Instruments. 64 Channel Analog Front End for Digital X-Ray Detector, 2009. URL http://www.ti.com/lit/gpn/afe0064.

L.T. Tran, L. Chartier, D.A. Prokopovich, M.I. Reinhard, M. Petasecca, S. Guatelli, M.L.F. Lerch, V.L. Perevertaylo, M. Zaider, N. Matsufuji, M. Jackson, M. Nancarrow, and A.B. Rosenfeld. 3D-Mesa Bridge Silicon Microdosimeter: Charge Collection Study and Application to RBE Studies in 12C Radiation Therapy. *IEEE Transactions on Nuclear Science*, 62(2):504–511, 2015.

TROG. What is Radiotherapy?, 2013. URL http://www.trog.com.au/What-is-radiotherapy.

A. Un, M. Un, and I. Han. Comparison of Some Human Tissues and Some Commonly Used Thermoluminescent Dosimeters for Photon Energy Absorption. *American Journal of Physics and Applications*, 2(6):145–149, 2014.

T.S.A. Underwood, H.C. Winter, M.A. Hill, and J.D. Fenwick. Mass-Density Compensation Can Improve the Performance of a Range of Different Detectors Under Non-Equilibrium Conditions. *Physics in Medicine and Biology*, 58: 8295–8310, 2013.

P. Urso, R. Lorusso, L. Marzoli, D. Corletto, A. Pepe, P. Imperiale, M. Mira, and

L. Bianchi. Characteristics and Criticalities of Octavius-4D Detector System for IMRT and RapidArc Plan Verification. *Physica Medica*, 32:67, 2016.

H. Wertz, J. Boda-Heggemann, C. Walter, B. Dobler, S. Mai, F. Wenz, and F. Lohr. Image-Guided In Vivo Dosimetry for Quality Assurance of IMRT Treatment for Prostate Cancer. *International Journal of Radiation Oncology, Biology, Physics*, 67:288–295, 2007.

WHO. Cancer, 2016. URL http://www.who.int/cancer/en/.

G. Wickman. A Liquid Ionization Chamber with High Spatial Resolution. *Physics in Medicine and Biology*, 19(1):66–72, 1974.

J.H. Wong, I. Fuduli, M. Carolan, M. Petasecca, M.L. Lerch, V.L. Perevertaylo, P. Metcalfe, and A.B. Rosenfeld. Characterization of a Novel Two Dimensional Diode Array the "Magic Plate" as a Radiation Detector for Radiation Therapy Treatment. *Medical Physics*, 39(5):2544–2558, 2012.

J.H.D. Wong. *Implementation of Silicon Based Dosimeters, the Dose Magnifying Glass and Magic Plate for the Dosimetry of Modulated Radiation Therapy*. PhD thesis, Centre for Medical Radiation Physics, 2011.

J.H.D. Wong, M. Carolan, M.L.F. Lerch, M. Petasecca, S. Khanna, V.L. Perevertaylo, P. Metcalfe, and A.B. Rosenfeld. A Silicon Strip Detector Dose Magnifying Glass for IMRT Dosimetry. *Medical Physics*, 37(2):427–439, 2010.

J.H.D. Wong, T. Knittel, S. Downes, M. Carolan, M.L.F. Lerch, M. Petasecca, V.L. Perevertaylo, P. Metcalfe, M. Jackson, and A.B. Rosenfeld. The Use of a

Silicon Strip Detector Dose Magnifying Glass in Stereotactic Radiotherapy QA and Dosimetry. *Medical Physics*, 38(3):1226–1238, 2011.

R. Wunstorf, H. Feick, E. Fretwurst, and et al. Damage-Induced Surface Effects in Silicon Detectors. *Nuclear Instruments and Methods in Physics Research Section A: Accelerators, Spectrometers, Detectors and Associated Equipment*, 377(2):290–297, 1996.

Y. Yamada, M.H. Bilsky, D.M. Lovelock, E.S. Venkatraman, S. Toner, J. Johnson, J. Zatcky, M.J. Zelefsky, and Z. Fuks. High-Dose, Single-Fraction Image-Guided Intensity Modulated Radiotherapy for Metastatic Spinal Lesions. *International Journal of Radiation Oncology, Biology, Physics*, 71(2):484–490, 2008.

S. Yamazaki, H. Nakane, and A. Tanaka. Basic Analysis of a Metal Detector. *IEEE Transactions on Instrumentation and Measurement*, 51(4):810–814, 2002.

C.X. Yu. Intensity-Modulated Arc Therapy With Dynamic Multileaf Collimation: An Alternative to Tomotherapy. *Physics in Medicine and Biology*, 40:1435–1449, 1995.

Q. Yue, J.M. Duan, R.Q. Li, and J. Yang. Systematic Analysis of the Arc Check Diode Arrays for Tomotherapy Delivery Verification. *International Journal of Medical Physics, Clinical Engineering and Radiation Oncology*, 3:218–225, 2014.

J. Ziegler. SRIM Software, 2015. URL http://www.srim.org/.